再構成可能なインテリジェントサーフェスによるユーザ中心の６Ｇネットワークの設計と最適化

Design and Optimization of User-centric 6G Networks with Reconfigurable Intelligent Surface

JIALE SHU

Department of Sciences and Informatics
Muroran Institute of Technology

This dissertation is submitted for the degree of
Doctor of Philosophy of Engineering

February 2025

Declaration

I hereby declare that this thesis is my own work and effort and that it has not been submitted anywhere for any award. Wherever contributions of others are involved, every effort is made to indicate this clearly, with due reference to the literature, and acknowledgement of collaborative research and discussions.

JIALE SHU
February 2025

Acknowledgements

Firstly, I extend my sincere gratitude to my supervisor, Prof. Kaoru Ota, for her unwavering support during my Ph.D. studies and research endeavors. Her patience, motivation, and profound expertise have been invaluable assets. Under her guidance, I have gained invaluable insights into the research process, academic writing, presentation skills, and more.

I am grateful to Prof. Kaoru Ota, Prof. Mianxiong Dong, Prof. He Li, and Prof. Jianwen Xu for their invaluable support of my scientific research. In particular, I extend my heartfelt gratitude to my supervisor, Prof. Kaoru Ota, for her extensive guidance, as well as to Prof. Mianxiong Dong for his significant assistance in various aspects of my research. I also extend my sincere thanks to my external committee member, Tomohiko Taniguchi, for agreeing to serve on my Ph.D. defense committee.

I would like to acknowledge the financial support from the JST Support for Pioneering Research Initiated by the Next Generation (SPRING), which enables me to concentrate on my studies without worrying about tuition and living expenses.

Last but not least, I extend my deepest gratitude to my family and parents for their unwavering spiritual support throughout my Ph.D. journey.

JIALE SHU
February 2025

Abstract

As a new paradigm for 6G communications, reconfigurable intelligent surface (RIS) has admirable properties that enable the dynamic control of electromagnetic waves, thereby attracting significant attention from both industry and academia. Moreover, the user-centric network highlights the personalized allocation of network resources to meet the requirements of each individual mobile device, which sheds light on future mobile transmission and the corresponding service delivery. Due to this characteristic, RIS is expected to play a crucial role in the evolution of user-centric 6G network systems. However, tailoring RIS into these systems to meet user requirements is still an open challenge. Therefore, this dissertation aims to provide a vision of realizing user-centric 6G network with RIS, specifically focusing on how to provide customizable and sustainable communication for a user-centric 6G.

In this dissertation, three major tasks are proposed on the various RIS-assisted wireless communication scenarios. The first task focuses on optimizing RIS deployment to maximize network coverage and ensure a consistent user experience across various environments. By strategically placing RISs, we can enhance coverage rate and provide seamless connectivity to users regardless of their locations. The second task aims at optimizing RIS beamforming directions based on user demands to enhance resource utilization efficiency. By leveraging real-time traffic prediction, RIS units can dynamically adjust their configurations to match user needs, providing efficient and targeted communication for users in static and mobile scenarios. Finally, the third task addresses the challenge of user mobility by optimizing Quality of Experience (QoE) for mobile users through adaptive RIS beamforming. This task is divided into two parts. The first part focuses on virtual reality (VR) scenarios, where RIS is used to dynamically adjust beamforming to maintain high QoE for users moving within VR environments. The second part focuses on the Internet of Robotic Things (IoRT) scenarios, where RIS is employed to ensure reliable communication and effective control of robotic devices as they navigate through complex environments.

Table of contents

List of figures xiii

List of tables xvii

1 Introduction 1
- 1.1 Background 1
- 1.2 System Outline and Challenges 2

2 The Optimization of RIS Deployment to Provide Consistent User Experience 5
- 2.1 Motivation 5
- 2.2 Related Work 7
- 2.3 Preliminaries, System Model, and Assumptions 9
  - 2.3.1 Far-field or Near-field 9
  - 2.3.2 Power Radiation Pattern and Gain 9
  - 2.3.3 System Model 10
  - 2.3.4 Path loss model 11
- 2.4 Problem formulation 14
  - 2.4.1 Communication Region and Visible Region 14
  - 2.4.2 Coverage Optimization 17
  - 2.4.3 Beamforming Optimization 19
- 2.5 Proposed Coverage Optimization and Codebook-Based Optimization 20
  - 2.5.1 Multiscale Spatial Search Algorithm 20
  - 2.5.2 Near-field Codebook Design 22
  - 2.5.3 Hierarchical Codebook-Based Optimization 24
- 2.6 Simulation Results 25
  - 2.6.1 Validation of the proposed MSS algorithm 26
  - 2.6.2 Benchmarking Algorithms 28
  - 2.6.3 Validation of Proposed HNCB Algorithm 30

2.7 Conclusion 33

3 Optimization of RIS Beamforming Based on User Behaviors for High-Efficiency Service 35

3.1 Motivation 35
3.2 System Model & Problem Formulation 37
3.2.1 System Model 37
3.2.2 Network Traffic Prediction 40
3.2.3 Problem Formulation 40
3.3 Learning Algorithm for MIMO System 41
3.3.1 The Algorithm for Network Traffic Prediction 42
3.3.2 DDPG Algorithm 42
3.4 simulation results 45
3.4.1 Network Traffic Prediction 45
3.4.2 Average QoE of Users 46
3.4.3 Average Transmission Rate Comparisons 47
3.4.4 Impact of system settings 47
3.5 Conclusion 48

4 QoE Optimization for Mobile Users Based on User Movements In VR Scenario 49

4.1 Motivation 49
4.2 Related Work 52
4.3 System Model 53
4.3.1 RIS Model 53
4.3.2 Channel Model 54
4.3.3 Codebook 56
4.3.4 The Mobility Model of VR Users 57
4.3.5 Problem Formulation 58
4.4 Localization-based Beamforming 59
4.4.1 Framework of the Localization-based Beamforming 59
4.4.2 AoDs Estimation 60
4.4.3 AoD-based Localization 63
4.4.4 Boundary of Localization 64
4.4.5 Location-based Beamforming 66
4.5 Simulation Results 68
4.5.1 Simulation Scenario and Settings 68
4.5.2 Performance of AoD-based Positioning 68

4.5.3 Performance of Our Proposed Algorithm 70
4.6 Conclusion 74

5 QoE Optimization for Mobile Users Based on User Movements for IoRT Scenario 75
5.1 Related Work 77
5.2 System Model and Problem Formulation 78
5.2.1 Communication Model 78
5.2.2 Sensing Model 80
5.2.3 Computing Model 81
5.2.4 Problem Formulation 81
5.2.5 Problem Decomposition 82
5.3 QoS Optimization in RIS-assisted ISCC system in IoRT scenarios 83
5.3.1 Minimization Computing Latency at Stage-I 83
5.3.2 Maximization Transmission Rate and Sensing Accuracy at Stage-II 85
5.4 Simulation Results 88
5.5 Conclusion 94

6 Conclusions and Future Directions 97

References 99

List of figures

2.1 Illustration of the near-field and far-field regions. 9

2.2 Multiple large-scale RIS-assisted wireless communication systems in an indoor scenario. The green line represents the LoS link between the AP and users, the yellow line denotes the indirect link after one RIS reflection, and the blue line indicates the indirect link following two RIS reflections. 11

2.3 Illustration of the communication region of the RIS 15

2.4 (a) Top view of the visible region of the RIS. (b) Side view of the visible region of the RIS. 16

2.5 Coverage rate optimization via the MSS for three different scenarios. The first column of Fig. 2.5 shows three different simulation scenarios, the second column shows the signal power map with random RISs, and the third column shows the signal power map with MSS RISs. 27

2.6 Comparative analysis of coverage performance. This figure presents three subplots depicting the coverage performance of the MSS and other comparison algorithms in three distinct scenarios. Fig. 2.6(a) shows the comparison in Scenario A, Fig. 2.6(b) presents the performance in Scenario B, and Fig. 2.6(c) shows the results in Scenario C. Across all the scenarios, MSS consistently achieves superior coverage, underscoring its effective deployment strategies and adaptive nature 28

2.7 Coverage rates of various methods versus the number of obstacles. 30

2.8 Visualization of optimized beamforming via HNCB targeting a specific region in the near-field case where $d_r = 1$ m and $d_t = 30$ m. 31

2.9 Comparison of the average received power across different RIS sizes for various beamforming methods. 31

2.10 Average received power variation with increasing user number for different beamforming methods 32

3.1 (a) The HRIS-assisted MU-MIMO communication system. (b) The structure of HRIS. 38
3.2 L-DRL algorithm for HRIS-assisted wireless communication system. . . . 41
3.3 (a) The users' network traffic in 24h. (b) Loss of the online LSTM for network traffic prediction. 45
3.4 Average QoE of the HRIS-assisted communication network. 46
3.5 Average transmission rate of L-DRL algorithm and the benchmarks. 47
3.6 Rewards at different learning rates. 48

4.1 An overview of our proposed framework in a multi-RIS-assisted mmWave VR network, where the LoS link from AP to VR users is blocked. The AP sends a probing signal when the VR user's location changes. Then, the UE estimates its position based on the received signal and uploads the estimated location to the AP. Finally, the location-based beamforming is conducted based on the estimated location. 51
4.2 Illustration of the channel model depicting the spatial relationship between the AP, RIS, and the VR user. 54
4.3 The direction of beam alignment changes with the movement of the VR user. 57
4.4 Illustration of the framework for the proposed localization-based beamforming method. 60
4.5 The proposed AoDs-based localization approach, where $\boldsymbol{q}_1$, $\boldsymbol{q}_2$ and $\boldsymbol{q}_3$ represent the location of RISs which are known in advance. 62
4.6 The accuracy of the proposed AoD-based positioning algorithm versus transmit power. 69
4.7 Alignment rate comparison between the proposed localization-based beamforming and exhaustive beam sweeping. 70
4.8 Comparison of VR user SNR under different RIS optimization algorithms. 70
4.9 The effect of the transmit power on the average QoE and average VR latency in the proposed multi-RIS-assisted mmWave wireless VR network. 71
4.10 The effect of the number of RIS element on the average QoE and average VR latency in the proposed multi-RIS assisted mmWave wireless VR network. 72
4.11 The effect of the number of VR users on the average QoE and average VR latency in the proposed multi-RIS-assisted mmWave wireless VR network. . 73

5.1 System model of RIS-enabled ISCC system for IoRT scenarios. 79
5.2 Simulation scenario for RIS-assisted ISCC in IoRT. 89
5.3 The convergence of the proposed algorithm via different RIS elements N. . 90

5.4 Simulation results showing the maximum and minimum latency values across the realization index. 91
5.5 The effect of the number of robots K on the average QoS and average latency in the proposed RIS-assisted ISCC for IoRT scenarios. 91
5.6 The effect of the number of RIS elements N on the average QoS and average latency in the proposed RIS-assisted ISCC for IoRT scenarios. 92
5.7 The effect of the number of edge computing resource f^e_{total} on the average QoS and average latency in the proposed RIS-assisted ISCC for IoRT scenarios. 93
5.8 BER performance of RIS-enabled ISCC system for IoRT scenarios. 94
5.9 The effect of the sensing SNR on the average QoS. 95

List of tables

2.1 Notation and Definitions 16
2.2 Simulation Parameters 26
2.3 Performance Metrics in Various Simulation Scenarios W/ and W/O RIS . . 26

4.1 Simulation Parameters 68

Chapter 1

Introduction

1.1 Background

Reconfigurable Intelligent Surface (RIS) technology is emerging as a promising solution for enhancing 6G communications, offering the potential for dynamic control over electromagnetic waves. The advantages of RIS are manifold. RIS units are easy to deploy, consisting of passive elements controlled by a digital microcontroller, which can be conveniently placed on various structures, including building facades, indoor walls, and even vehicles. This versatility makes RIS deployment cost-effective compared to traditional solutions such as adding more base stations or relays. RIS also improves spectral efficiency by adjusting signal transmission paths and beamforming through multipath propagation, thereby enabling more users and higher data transmission within the same spectrum resources. Moreover, RIS can enhance signal strength and extend network coverage by establishing virtual line-of-sight links, especially useful in environments where physical obstacles block direct communication paths. Additionally, RIS optimizes power consumption by managing signal propagation paths more efficiently, thereby reducing overall system energy use and communication expenses. These attributes make RIS not only an effective solution for boosting network performance but also a sustainable one.

However, traditional RIS-assisted networks are not inherently user-centric, leading to several limitations. In a traditional setup, RIS configurations are often static or predetermined, which means they cannot adapt in real time to specific user needs or environmental changes. This lack of adaptability results in inconsistent service quality, as the network cannot adjust to the varying locations or demands of users. Resource utilization also tends to be inefficient because the allocation is not tailored to individual user needs, which may lead to over-provisioning in some areas and under-provisioning in others. Moreover, traditional RIS-assisted systems have limited ability to handle dynamic scenarios, such as user mobility, which further degrades the Quality of Experience (QoE) for mobile users.

To address these shortcomings, user-centric RIS-assisted networks have been proposed. In a user-centric design, the focus shifts from a generalized, one-size-fits-all approach to a personalized allocation of network resources, ensuring that each user's unique requirements are met. User-centric RIS systems dynamically adjust their beamforming and resource allocation based on real-time data, providing a more efficient and responsive network experience. This approach significantly enhances the consistency of user experience, optimizes resource utilization by dynamically adapting to user demand, and improves adaptability to user mobility by maintaining beam alignment in response to changes in user location. These benefits position user-centric RIS as a pivotal technology for achieving the high performance and flexibility required in future 6G networks.

Despite the clear advantages of user-centric RIS-assisted networks, their implementation involves addressing several key challenges that necessitate adjustments in three major areas. To overcome these challenges, we introduce a user-centric RIS-assisted network with three main adjustments: First, optimization of RIS deployment is crucial to increase network coverage, ensuring that users can receive consistent service quality regardless of their location. This involves strategically placing RIS units to maximize coverage and provide a consistent user experience in all areas of the network. Second, resource utilization efficiency must be enhanced by optimizing RIS beamforming based on user behaviors for high-efficiency service. The network needs to allocate resources dynamically based on user demand, maximizing efficiency while effectively coordinating multiple RIS units to prevent interference and ensure seamless communication, especially in dense urban environments. Third, adaptability to user movements is essential for maintaining Quality of Experience (QoE) for mobile users. This involves optimizing network configurations in real-time by adapting beamforming to changes in user location, which helps address the increased computational complexity associated with serving highly dynamic scenarios such as virtual reality (VR) or robotic communication networks.

1.2 System Outline and Challenges

In this section, three major challenges in the dissertation are briefly introduced, and the following chapters will discuss these research problems in detail.

In the first research task, we focused on optimizing RIS deployment to provide a consistent user experience by jointly optimizing the placement and cooperative beamforming of large-scale RISs. We proposed a multiscale spatial search (MSS) algorithm for optimal RIS placement and developed a hierarchical near-field codebook with a corresponding beam training methodology to maximize received signal strength. Our simulation results demonstrated substantial improvements in system coverage and received signal strength compared to existing benchmarks, showcasing the efficiency of the proposed joint optimization framework. Future work will explore extending this framework to handle dynamic user distributions and complex indoor environments.

The second task aimed to optimize RIS beamforming for high-efficiency service by leveraging user behaviors and predicted network demands. By employing an online LSTM network for traffic prediction and the DDPG algorithm for phase adjustment, we enhanced the Quality of Experience (QoE) for users based on their diverse requirements. Our approach resulted in significant QoE improvements, nearly doubling compared to randomly adjusted RIS phase shifts. Additionally, a 20% QoE improvement was achieved compared to non-predictive methods. Future research will consider incorporating real-time user behavior feedback to further enhance adaptability and responsiveness of the RIS configurations.

In the third task, we tackled the QoE optimization for mobile VR users by proposing a multi-RIS-assisted mmWave wireless VR system. Our work focused on leveraging RIS for both mitigating mmWave path loss and enabling precise user positioning. We introduced a two-phase framework involving localization through maximum likelihood estimation and subsequent beamforming optimization based on user locations. This approach led to improved QoE without requiring full channel state information, as validated by numerical simulations. Future work will extend this approach to cover dynamic environments with rapidly moving users and explore robust beamforming methods to handle unpredictable motion.

The fourth task addressed QoE optimization for the Internet of Robotic Things (IoRT) using a RIS-enabled integrated sensing, computing, and communication (ISCC) system. We formulated a complex optimization problem to enhance computational speed, communication rate, and sensing accuracy. Our solution utilized a block coordinate descent (BCD) approach with alternating optimization (AO) to effectively maximize the overall system performance. Extensive simulations showed that our approach notably improved the quality of service (QoS) and reduced system latency, emphasizing the practicality of our method for extreme IoRT environments. Future work will focus on enhancing the system's scalability and developing more adaptive algorithms to respond to rapidly changing scenarios in IoRT deployments.

Chapter 2

The Optimization of RIS Deployment to Provide Consistent User Experience

2.1 Motivation

With the successful deployment of fifth-generation (5G) networks, researchers are now shifting their focus toward the development of sixth-generation (6G) networks. Designed to support emerging applications such as virtual reality (VR) [15], augmented reality (AR) [54], and autonomous driving (AD) [39], 6G aims to deliver faster transmission speeds, lower latency, and increased spectral efficiency [63]. These improvements are achieved through higher frequency bands, wider bandwidths, and massive antenna arrays.

However, the shift to higher frequency bands reduces the ability of electromagnetic waves to bypass obstacles, increasing their susceptibility to obstacles such as furniture and walls in indoor environments [90, 48]. This challenge necessitates innovative solutions to maintain and enhance system performance. One promising solution is RIS technology, which consists of numerous passive elements capable of independently controlling the phase and amplitude of incident signals [80]. An RIS can establish indirect links to increase the received signal strength for users when obstacles impede the line-of-sight (LoS) link between the transmitter and the receiver [69, 94].

In contrast to alternative solutions such as active relays, the RIS offers lower cost, higher energy efficiency, and easier deployment [14], making it a promising technology for future 6G networks [55, 49]. However, implementing an RIS presents challenges, notably the multiplicative fading effect, which exacerbates path loss in the transmitter–RIS–receiver link [18]. To address this issue, both the academic and industrial sectors advocate deploying large-scale RISs to increase channel gain and reduce path loss [3]. Here, a large-scale RIS refers to an RIS with a significantly large physical size (aperture) and a large number of elements, providing higher channel gain and improved signal reflection capabilities [73].

To fully leverage the benefits of large-scale RISs in improving wireless communication, two key challenges need to be addressed:

(i) **Large-scale RIS Placement Strategy:** RIS placement significantly influences signal coverage. Transitioning from traditional to large-scale RIS deployment requires cooperative reflection among multiple RISs, which should be considered in the placement strategy.

(ii) **Beamforming Direction Adjustment:** Once optimally placed, the beamforming direction of a large-scale RIS must be tuned according to the user locations to maximize the received power. However, obtaining reliable channel state information (CSI) for reflective beamforming is challenging due to the increased complexity of the numerous elements in large-scale RISs [8].

Significant efforts have aimed to address the aforementioned challenges by optimizing the placement of the RIS and the beamforming direction. In [97] and [96], the authors optimized the deployment of multiple RISs in an indoor environment to enhance the coverage of the communication network. The authors of [5] enhance the received signal strength for users by optimizing the beamforming direction of the RIS. However, existing works have focused mainly on single reflections of the RIS to increase coverage and increase signal strength, with limited attention given to cooperative reflections among multiple RISs, which is a crucial factor in large-scale RIS deployment.

Cooperative beamforming in network systems can significantly enhance system performance. Recently, some studies have focused on cooperative reflections among multiple RISs to further improve system performance. For example, in [100], the performance of a double-RIS-assisted multiuser communication system with cooperative passive beamforming was analyzed. The authors of [46] introduced a cooperative beamforming design for multi-RIS assisted networks. Additionally, a unified framework was proposed to optimize the cooperative reflection between multiple RISs [99]. However, these studies do not comprehensively consider the placement and cooperative beamforming of multiple RISs while also neglecting the impact of near-field effects.

Motivated by the above analysis, this paper attempts to fill this gap by proposing a novel framework that offers a comprehensive solution for large-scale RIS deployment and cooperative beamforming in multiobstacle indoor scenarios. The proposed framework jointly optimizes the deployment and cooperative beamforming of multiple large-scale RISs to effectively enhance coverage and received signal strength, with the consideration of near-field effects. Specifically, the proposed framework consists of two core strategies. First, a multiscale spatial search (MSS) algorithm is introduced, which incorporates greedy strategies to determine the optimal RIS locations and ensure maximal coverage by avoiding local optima. Second, upon determining the optimal RIS locations, a near-field codebook is designed, and a corresponding RIS beam training method is implemented to optimize the cooperative beamforming direction. Extensive simulations are conducted to evaluate the effectiveness of the proposed framework, and the results clearly demonstrate its superiority over other benchmark methods. The main contributions of this paper can be summarized as follows:

- Proposed a novel framework for jointly optimizing multiple RIS deployments and cooperative beamforming for multiple large-scale RISs in a multiobstacle indoor scenario. The proposed framework can enhance both the network coverage and the received signal strength for users in large-scale RIS environments.
- Development of an efficient MSS algorithm to identify the optimal locations for RIS deployment. The algorithm first divides the 3D space into large-resolution regions to identify potential deployment areas. These potential areas are further partitioned into smaller resolution regions to locate the precise RIS placement. In addition, a greedy strategy is introduced to avoid local optima and ensure maximal coverage.
- Design of a hierarchical near-field codebook and a corresponding RIS beam training method to optimize cooperative beamforming. This approach specifically addresses the near-field effects often neglected in current studies, thereby maximizing the received signal strength by users.
- Comprehensive performance evaluation and validation of the proposed methods through simulations. The results highlight the efficacy of the proposed approach, demonstrating improvements in coverage and received signal strength compared with existing methodologies.

2.2 Related Work

As a new paradigm for 6G communications, the RIS has admirable properties that enable the dynamic control of electromagnetic waves, thereby attracting significant attention from both industry and academia. Recently, the performance of RIS-assisted wireless networks has been widely studied. In [56], the RIS was applied to establish a virtual link when the LoS link from the transmitter to the receiver was blocked. The authors proposed an alternating optimization algorithm to optimize the phase shift of the RIS, thereby maximizing the achievable rate of the multi-input multioutput (MIMO) system. In [3], a self-configuring RIS was applied to increase users' received signal strength. In [98], a simultaneously transmitting and reflecting RIS (STAR-RIS) was utilized to maximize the sum rate of unmanned aerial vehicles (UAVs), which was achieved by jointly optimizing the UAV trajectory and STAR-RIS passive beamforming. However, the above works focused on optimizing the phase shift of the RIS to enhance the performance of the network, ignoring multi-RIS deployment and placement locations of the RIS.

Some works have explored the impact of RIS placement on network performance [80, 42, 97]. In [80], the authors explore the influence of a single RIS location on the performance of wireless communication systems. The simulation results show optimal system performance when the RIS is positioned near the users or the BS. The authors of [42] introduced a deep reinforcement learning (DRL)-based algorithm for concurrently optimizing the RIS's position and phase shift to enhance the performance of the network. In [97], A gradient descent-based algorithm is applied to pinpoint the optimal deployment strategy for multiple RISs. The proposed methodologies significantly increased the coverage of millimeter-wave communication systems, especially in environments dense with obstacles. However, existing works have focused primarily on single reflections of the RIS to improve coverage and signal strength, paying little attention to cooperative reflections among multiple RISs, which is crucial for large-scale RIS deployment.

Some works have explored the potential for cooperative beamforming between RISs to enhance the performance of wireless communication systems. The authors of [100] evaluate the performance of cooperative passive beamforming involving two RISs, and the simulation results demonstrate that, given sufficiently large RIS gains, a double-RIS cooperative beamforming system could yield a higher signal–to–noise ratio (SNR) than traditional single-RIS systems. [26] presented a novel hybrid beamforming scheme for a multihop RIS-assisted system, employing a DRL-based approach for designing collaborative digital and analog beamforming matrices. The numerical results corroborate the effectiveness of multihop RISs in extending the coverage of terahertz (THz) networks. In [52], the authors propose a novel multipath beam routing scheme for environments densely populated with an RIS, which services multiple antenna BSs and single-antenna users. However, the near-field effects caused by large-scale RISs have also not been adequately considered in the above works. To our knowledge, how to jointly optimize the deployment and cooperative beamforming of multiple large-scale RISs in a multiobstacle indoor environment to increase the coverage and received signal strength has not been addressed previously.

2.3 Preliminaries, System Model, and Assumptions

2.3.1 Far-field or Near-field

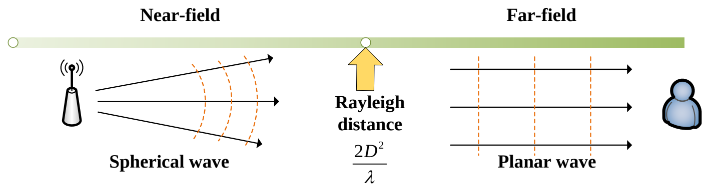

Fig. 2.1 Illustration of the near-field and far-field regions.

Fig. 5.1 shows the classification of the electromagnetic field around an antenna into near-field and far-field regions. The distance from the antenna or transmitter to the receiver, which significantly influences the choice of channel model, differentiates these regions. When the distance exceeds the threshold, defined by $L = \frac{2D^2}{\lambda}$ (D denotes the maximum dimension of the array aperture and λ is the wavelength), the spherical waves can be approximated as planar waves [71]. The far-field assumption is prevalent in prior research because traditional RIS-assisted systems have relatively limited use in the near-field region. However, with the transition toward large-scale RIS deployment, the near-field region proportionally expands [21]. For example, in a scenario with a carrier frequency of $f = 60$ GHz ($\lambda = 0.005$ m) and an array aperture of $D = 0.25$ m, the resulting Rayleigh distance L is 25 m. Thus, in a large-scale RIS-assisted system, the receiver is likely in the near-field region, necessitating a spherical wave assumption for accurate channel modeling.

2.3.2 Power Radiation Pattern and Gain

Within RIS-assisted systems, the power radiation pattern characterizes how the power of the received or reflected signal varies with direction and distance from the RIS. This paper introduces a normalized power radiation pattern, $F(\theta, \varphi)$, where θ and φ denote the elevation and azimuth angles relative to the RIS plane, respectively. The normalized power radiation pattern is a dimensionless function scaled such that its maximum value is 1, representing the relative strength of radiation in different directions. A typical normalized power radiation pattern, as suggested in [97], is as follows:

$$F(\theta, \varphi) = \begin{cases} \cos\theta & \theta \in \left[0, \frac{\pi}{2}\right], \varphi \in [0, 2\pi] \\ 0 & \theta \in \left(\frac{\pi}{2}, \pi\right], \varphi \in [0, 2\pi] \end{cases}. \tag{2.1}$$

Equation (5.1) shows that antenna gain, an essential performance indicator encompassing antenna directivity and radiation efficiency, depends on the elevation angle θ, peaking when $\theta = 0$. The term antenna gain describes how much power is transmitted or received in the direction of peak radiation relative to that of an isotropic antenna, which, by assuming 100% antenna efficiency, can be written as:

$$G = \frac{4\pi}{\int_{\varphi=0}^{2\pi}\int_{\theta=0}^{\pi} F(\theta,\varphi)\sin\theta d\theta d\varphi}. \tag{2.2}$$

Using a power radiation pattern as defined in Eq. (5.2), an antenna with 100% radiation efficiency would have a gain of 4. Accordingly, the power radiation pattern of the RIS elements is as follows:

$$G(\theta,\varphi) = \begin{cases} 4\cos\theta & \theta \in \left[0,\frac{\pi}{2}\right], \varphi \in [0,2\pi], \\ 0 & \theta \in \left(\frac{\pi}{2},\pi\right], \varphi \in [0,2\pi]. \end{cases} \tag{2.3}$$

Eq. (5.3) denotes the power radiation pattern of the RIS elements in the following section.

2.3.3 System Model

This paper considers multiple large-scale RIS-assisted wireless communications in an indoor environment, as illustrated in Fig. 2, where an AP with L antennas assisted by $\boldsymbol{Q}$ RISs simultaneously serves $\boldsymbol{U}$ single-antenna users. An indirect link via the RIS can be established when obstacles obstruct the LoS link between the AP and users. The index sets of users and RISs can be represented as $\boldsymbol{U} = \{\boldsymbol{u}_1, \boldsymbol{u}_2, \cdots, \boldsymbol{u}_R\}$ and $\boldsymbol{Q} = \{\boldsymbol{q}_1, \boldsymbol{q}_2, \cdots, \boldsymbol{q}_K\}$, respectively. For simplicity, both the AP and the users' antennae are assumed to be omnidirectional, offering uniform gain in all directions in the proposed model. The locations of the AP, the center of the k-th RIS, and the r-th user are represented as $\boldsymbol{q}_{AP} \in \mathbb{R}^3$, $\boldsymbol{q}_k \in \mathbb{R}^3$, and $\boldsymbol{u}_r \in \mathbb{R}^3$, respectively, where $\mathbb{R}^3$ denotes the 3-dimensional Cartesian coordinate space.

Each RIS comprises a uniform planar array (UPA) of $N \times M$ passive elements, where N and M represent the number of rows and columns on the RIS, respectively. RISs are typically installed on flat surfaces, such as walls or ceilings, making the UPA configuration both practical and effective for these environments. Each element spans an area of size $d_x \times d_y$, with d_x and d_y denoting the lengths along the row and column directions, respectively. As per [5], d_x and d_y are equivalent to half of λ, i.e., $d_x = d_y = \lambda/2$.

The power radiation pattern of each element is characterized by $G(\theta,\varphi)$, as defined in Eq. (5.3), which allows each element to adjust the reflection coefficient $\tau_{n,m}^k = Ae^{\phi_{n,m}^k}$ to control the incident signal, where $\phi_{n,m}^k$ is the phase shift, A is the amplitude, and $N_{n,m}^k$ is a

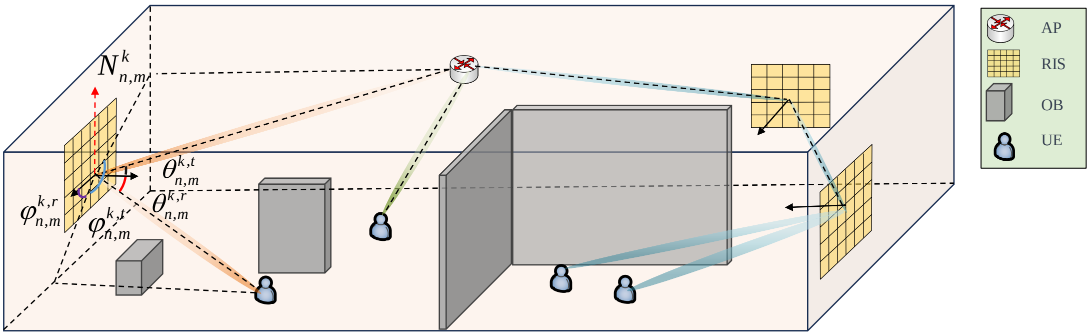

Fig. 2.2 Multiple large-scale RIS-assisted wireless communication systems in an indoor scenario. The green line represents the LoS link between the AP and users, the yellow line denotes the indirect link after one RIS reflection, and the blue line indicates the indirect link following two RIS reflections.

general element on the k-th RIS. In this paper, it is assumed that all the elements have the same amplitude, $A = 1$.

A free-space path loss model is employed to represent path loss, as it offers a suitable approximation when high-frequency signal reflection from obstacles and walls is notably weaker than that of LoS- or RIS-reflected paths. This model forms the basis of the proposed system model and guides the subsequent sections of this study.

2.3.4 Path loss model

The power received by $\boldsymbol{u}_r$ through the LoS path from the AP can be expressed as a function of multiple parameters, which includes the transmit power of the AP P_t, the antenna gain of the AP G_t, and the antenna gain of the user G_r. In the absence of obstacles in the LoS link, as illustrated in Fig. 2.2, the received power P^r_{los} is given by:

$$P^r_{los} = \left(\frac{P_t G_t}{4\pi d^2_{A,r}}\right)\left(\frac{\lambda^2 G_r}{4\pi}\right). \tag{2.4}$$

Here, $d_{A,r}$ signifies the distance from $\boldsymbol{q}_{AP}$ to $\boldsymbol{u}_r$. Given an arbitrary element, $N^k_{n,m}$ on $\boldsymbol{q}_k$, and defining $\theta^{k,t}_{n,m}$, $\varphi^{k,t}_{n,m}$, and $d^{k,t}_{n,m}$ as the elevation angle, azimuth angle, and distance from the AP to $N^k_{n,m}$, respectively, the received signal power at $N^k_{n,m}$ can be modeled as follows:

$$P^{k,t}_{n,m} = \frac{P_t G_t G(\theta^{k,t}_{n,m}, \varphi^{k,t}_{n,m})\lambda^2}{(4\pi d^{k,t}_{n,m})^2}. \tag{2.5}$$

From Eq. (5.5), the power that reflects off $N^k_{n,m}$ to user $\boldsymbol{u}_r$ is as follows:

$$P^{k,r}_{n,m} = \frac{P_t G_t G_r G^k_{n,m} \lambda^4 \left\| \tau^k_{n,m} \right\|^2}{(4\pi)^4 (d^{k,t}_{n,m})^2 (d^{k,r}_{n,m})^2}. \tag{2.6}$$

In this equation, $G^k_{n,m} = G(\theta^{k,t}_{n,m}, \varphi^{k,t}_{n,m}) G(\theta^{k,r}_{n,m}, \varphi^{k,r}_{n,m})$ and $\theta^{k,r}_{n,m}$, $\varphi^{k,r}_{n,m}$, and $d^{k,r}_{n,m}$ represent the elevation angle, the azimuth angle and the distance from $N^k_{n,m}$ to $\boldsymbol{u}_r$, respectively.

The user's received signal power via $\boldsymbol{q}_k$ reflection is as follows:

$$\begin{aligned} P^r_{nlos} = {} & P_t \frac{G_t G_r \lambda^4}{(4\pi)^4} \\ & \times \left| \sum_{n=1}^{N} \sum_{m=1}^{M} \frac{\sqrt{G^k_{n,m}}}{d^{k,t}_{n,m} d^{k,r}_{n,m}} e^{\frac{-j2\pi\left(d^{k,t}_{n,m} + d^{k,r}_{n,m}\right)}{\lambda}} \right|^2. \end{aligned} \tag{2.7}$$

Importantly, the received power, P^r_{nlos}, depends on the number of elements. The channel gain provided by the RIS can offset path loss when the number of elements on the RIS is sufficiently large, thus enabling joint reflection among multiple RISs.

This paper extends this analysis to consider the received signal power via two RIS joint reflections. Let $\boldsymbol{q}_j$ denote the second RIS and let $N^j_{p,q}$ be an arbitrary element on $\boldsymbol{q}_j$; the received power P^r_{coop} is as follows:

$$\begin{aligned} P^r_{coop} = {} & P_t \frac{G_t G_r \lambda^6}{(4\pi)^6} \\ & \times \left| \sum_{n=1}^{N} \sum_{m=1}^{M} \sum_{p=1}^{N} \sum_{q=1}^{M} \frac{\sqrt{G^k_{n,m} G^j_{p,q}}}{d^{k,t}_{n,m} d^{p,q}_{n,m} d^{j,r}_{p,q}} e^{\frac{-j2\pi\left(d^{k,t}_{n,m} + d^{p,q}_{n,m} + d^{j,r}_{p,q}\right)}{\lambda}} \right|^2, \end{aligned} \tag{2.8}$$

where $G^j_{p,q}$ denotes the product of the incident and reflective gains of $\boldsymbol{q}_j$, $d^{p,q}_{n,m}$ represents the distance from $N^k_{n,m}$ to $N^j_{p,q}$, and $d^{j,r}_{p,q}$ indicates the distance from $N^j_{p,q}$ to $\boldsymbol{u}_r$.

While Eq. (2.8) provides a comprehensive representation of the received power in relation to various system parameters, its complexity renders direct inference challenging. For a more intuitive understanding of the impact of these parameters on the received power, this paper subsequently discusses the free-space loss models in both far-field and near-field scenarios.

Far-field Beamforming

Under the conditions of far-field beamforming, both the transmitter and receiver are situated within the RIS's far-field region. Given that the variance in distances and angles from each element on the RIS to the transmitter or receiver is minute, we can simplify the proposed model by assuming that all the elements share the same coordinates. Consequently, d_t and d_r are used to denote the distances from the transmitter and receiver to the RIS, respectively. Similarly, θ_t, φ_t, θ_r, and φ_r denote the elevation and azimuth angles from the transmitter to the RIS and from the RIS to the receiver, respectively.

Using these simplifications, the received signal power (as per Eq. (5.7)) can be translated into the following form:

$$P^r_{nlos} = P_t \frac{G_t G_r M^2 N^2 \lambda^4 G(\theta_t, \varphi_t) G(\theta_r, \varphi_r)}{256\pi^4 d_r^2 d_t^2}. \tag{2.9}$$

When the combined antenna gain $G(\theta_t, \varphi_t)G(\theta_r, \varphi_r)$ equals G^2, the maximum received power can be achieved as follows:

$$P^r_{max} = P_t \frac{G_t G_r G^2 M^2 N^2 \lambda^4}{256\pi^4 d_r^2 d_t^2}. \tag{2.10}$$

Hence, the path loss can be calculated according to Eq. (5.9) as:

$$PL_{far} = \frac{256\pi^4 d_r^2 d_t^2}{G_t G_r G^2 M^2 N^2 \lambda^4}. \tag{2.11}$$

Similarly, the received signal power for two RIS joint reflections (as per Eq. (2.8)) can be expressed in the following manner:

$$P^r_{coop} = \frac{P_t G_t G_r \lambda^6 M^4 N^4 G^k_{n,m} G^j_{p,q}}{(4\pi)^6 d_r^2 d_t^2 d_{ris}^2}. \tag{2.12}$$

Here, d_{ris} represents the distance between the first and second RSIs. Thus, the maximum value of Eq. (5.12) becomes:

$$P^r_{max} = \frac{P_t G_t G_r \lambda^6 M^4 N^4 G^4}{(4\pi)^6 d_r^2 d_t^2 d_{ris}^2}. \tag{2.13}$$

Near-field Beamforming

When the transmitter, the receiver, or both are situated within the near-field region of the RIS, we refer to this as the near-field beamforming case. Given this condition, it is essential to consider that each element within the RIS possesses precise coordinates and incident angles.

For a desired direction $(\theta_{des}, \varphi_{des})$, the maximum received power can be approximately formulated as [73]:

$$P^r_{max} \approx \frac{P_t G_t G_r \lambda^2}{16\pi^2 \left(d_r + d_t\right)^2}, \tag{2.14}$$

when

$$\phi^k_{n,m} = \mod \left(\frac{2\pi(d^{k,t}_{n,m} - d^{k,t'}_{n,m})}{\lambda}, 2\pi \right), \tag{2.15}$$

where $d^{k,t'}_{n,m}$ is the distance from $N^k_{n,m}$ to a virtual transmitter, whose location can be expressed as $\boldsymbol{q}_k + (-d_t \sin\theta_{des} \cos\varphi_{des}, -d_t \sin\theta_{des} \sin\varphi_{des}, d_t \cos\theta_{des})$. The path loss corresponding to Eq. (5.15) can be written as:

$$PL_{near} = \frac{16\pi^2 \left(d_r + d_t\right)^2}{G_t G_r \lambda^2}. \tag{2.16}$$

The critical notations and definitions of this paper are consolidated in Table 2.1 for easy reference.

2.4 Problem formulation

2.4.1 Communication Region and Visible Region

The deployment of RISs plays a key role in enhancing the received signal power of users. By strategically positioning RISs, the coverage of wireless communication systems can be significantly improved. The coverage region is the area where the received signal power exceeds a certain threshold, denoted by P_{th}. This threshold is closely related to environmental noise. For RIS placement optimization, this paper considers that the distance between the AP and RIS greatly exceeds the size of the RIS. In this context, the received power of users aligns with Eq. (2.8). The coverage range of the AP manifests as a sphere with a radius of

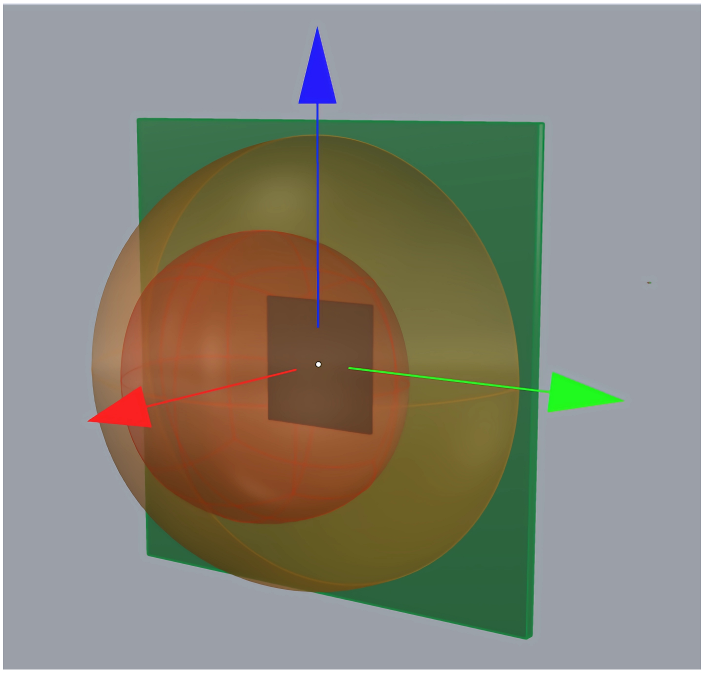

Fig. 2.3 Illustration of the communication region of the RIS

$R_a = \sqrt{\frac{P_t G_t G_r \lambda^2}{16\pi^2 P_{th}}}$. The coverage range of $\boldsymbol{q}_k$ can subsequently be described as:

$$
\begin{aligned}
R_r^k(\theta_t, \theta_r, d_t) &= \sqrt{P_t \frac{G_t G_r M^2 N^2 \lambda^4 G_{n,m}^k}{256\pi^4 d_t^2 P_{th}}} \\
&= H_s \times \sqrt{\frac{G(\theta_t, \varphi_t) G(\theta_r, \varphi_r)}{d_t^2}},
\end{aligned}
\tag{2.17}
$$

where $H_s = \sqrt{P_t \frac{G_t G_r M^2 N^2 \lambda^4}{256\pi^4 P_{th}}}$ denotes the value of hyperparameters relevant to the system's configuration. Therefore, the communication distance of the RIS depends on its position, denoted as $R_r^k(\theta_t, \theta_r, d_t)$.

Fig. 5.3 illustrates the communication region of an RIS. The red contour outlines the region boundaries where the received power surpasses P_{th}. The yellow hemispherical surface, with its radius indicated by $R_r^k(\theta_t, 0, d_t)$, marks the upper limit of the RIS communication range. Owing to the beamforming capability of the RIS, the yellow region is selected as the RIS communication coverage area to optimize the RIS position.

In complex indoor environments, covering certain areas could pose challenges if we consider only single reflections. Therefore, for enhanced user power reception, this paper considers cooperative reflections between two RISs. According to Eq. (5.12), the approximate

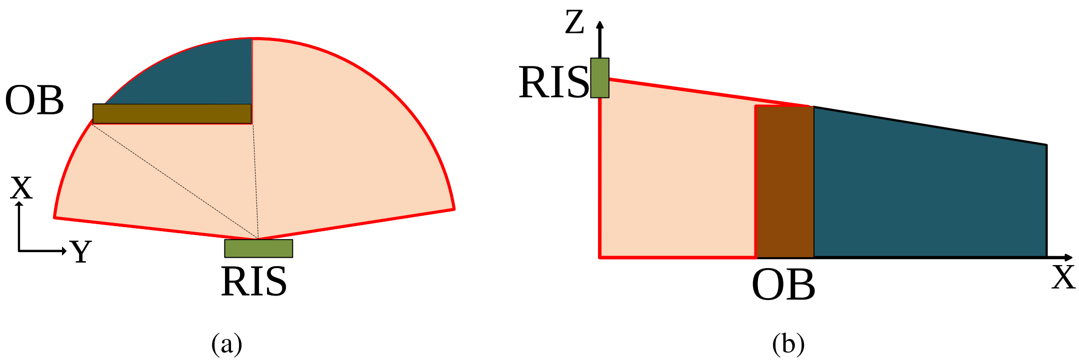

Fig. 2.4 (a) Top view of the visible region of the RIS. (b) Side view of the visible region of the RIS.

Table 2.1 Notation and Definitions

Notation	**Definition**	**Notation**	**Definition**
N	Number of rows of elements in RIS	M	Number of columns elements in RIS
P_t	Transmit power of AP	G_t	Antenna gain of AP
G_r	Antenna gain of users	G	Gain of each element
P_{th}	The threshold of received power	λ	The wavelength of carrier frequency
$N^k_{n,m}$	Element in the n rows and m columns in k-th RIS	$\tau^k_{n,m}$	Reflection coefficient of $N^k_{n,m}$
$d^{k,t}_{n,m}$	The distance between $N^k_{n,m}$ and transmitter	$d^{k,r}_{n,m}$	The distance between $N^k_{n,m}$ and receiver
d_t	The distance from the AP to RIS center	d_r	The distance from RIS center to receiver
d_{ris}	The distance from the first to second RIS	$R^k_r(\theta_t, 0, d_t)$	The maximum coverage range of k-th RIS
$G(\theta, \varphi)$	The power radiation pattern of elements	$\phi^k_{n,m}$	The phase shift of $N^k_{n,m}$
(θ_r, φ_r)	The elevation and azimuth angles from AP to center of RIS	(θ_t, φ_t)	The elevation and azimuth angles from the center of RIS to receivers
$(\theta^{k,t}_{n,m}, \varphi^{k,t}_{n,m})$	The elevation and azimuth angles from $N^k_{n,m}$ to transmitter	$(\theta^{k,r}_{n,m}, \varphi^{k,r}_{n,m})$	The elevation and azimuth angles from $N^k_{n,m}$ to receiver

communication distance of the cooperative reflection can be written as:

$$R_c^k = \frac{M^2N^2G^2\lambda^3}{(4\pi)^3 d_r d_t d_{ris}} \sqrt{\frac{P_t G_t G_r}{P_{th}}}. \tag{2.18}$$

Then, we focus on defining the visible area, which refers to the region where communication with the AP or RISs through an LoS channel is feasible. Fig. 2.4 provides top and side views of the visible region. Let $\theta(\boldsymbol{q}_k, \boldsymbol{p})$ denote the elevation angle from $\boldsymbol{q}_k$ to point $\boldsymbol{p}$, $\boldsymbol{Q}$ denote the set of all nonobstructed points in a given scenario, and $\boldsymbol{O}$ denote the set of points constituting obstacles. The communication region of $\boldsymbol{q}_k$ can be expressed as:

$$\begin{aligned} \boldsymbol{C}_k = \big\{ \boldsymbol{p} \in \boldsymbol{Q} \mid \theta\left(\boldsymbol{p}, \boldsymbol{q}_k\right) \leq \frac{\pi}{2}, \\ \|\boldsymbol{p} - \boldsymbol{q}_k\| \leq R_r^k\left(\theta_t, 0, d_t\right) \big\}. \end{aligned} \tag{2.19}$$

However, the existence of obstacles in the scenario implies that certain points in $\boldsymbol{C}_k$ cannot receive signals from $\boldsymbol{q}_k$. Thus, the visible region$\boldsymbol{V}_k$ can be defined as the set of points in $\boldsymbol{C}_k$ maintaining LoS links with $\boldsymbol{q}_k$:

$$\boldsymbol{V}_k = \{\boldsymbol{p} \in \boldsymbol{C}_k \mid \forall \lambda \in [0,1], \lambda \boldsymbol{p} + (1-\lambda)\boldsymbol{q}_k \notin \boldsymbol{O}\}. \tag{2.20}$$

Finally, the blind region of the AP is defined as

$$\begin{aligned} \boldsymbol{B}_{AP} = \{\boldsymbol{p} \in \boldsymbol{Q} \mid \|\boldsymbol{q}_{AP} - \boldsymbol{p}\| > R_a\} \cup \\ \{\boldsymbol{p} \in \boldsymbol{Q} \mid \exists \lambda \in [0,1], \lambda \boldsymbol{p} + (1-\lambda)\boldsymbol{q}_{AP} \in \boldsymbol{O}\}. \end{aligned} \tag{2.21}$$

2.4.2 Coverage Optimization

To highlight the role of the k-th RIS in enhancing system coverage, we devise the performance function $F(\boldsymbol{q}_k, \boldsymbol{p})$. $\boldsymbol{N}_k$ is defined as the index set of all RISs whose visible region intersects with the visible region of $\boldsymbol{q}_k$. At a specified point $\boldsymbol{p}$, the performance function $f(\boldsymbol{q}_k, \boldsymbol{p})$ is expressed as follows:

$$f(\boldsymbol{q}_k, \boldsymbol{p}) = \begin{cases} 1, \text{ if } \boldsymbol{p} \in \boldsymbol{V}_k \text{ and } \forall j \in \boldsymbol{N}_k, \boldsymbol{p} \notin \boldsymbol{V}_j, \\ 0, \text{ if } \boldsymbol{p} \in \boldsymbol{V}_k \text{ and } \exists j \in \boldsymbol{N}_k, \boldsymbol{p} \in \boldsymbol{V}_j, \\ 0, \text{ if } \boldsymbol{p} \notin \boldsymbol{V}_k. \end{cases} \tag{2.22}$$

In Eq. (5.23), $f(\boldsymbol{q}_k, \boldsymbol{p})$ is evaluated as 1 if the point $\boldsymbol{p}$ is in the visible region of $\boldsymbol{q}_k$ and not in the visible region of any other intersecting RIS. For all other conditions, it is evaluated as 0.

This paper then defines the overall performance function $F(\boldsymbol{q}_k, \boldsymbol{p})$ of $\boldsymbol{q}_k$ as follows:

$$F(\boldsymbol{q}_k, \boldsymbol{p}) = \Psi + \frac{1}{P}\int_{\boldsymbol{V_k}} f(\boldsymbol{q}_k, \boldsymbol{p}) \tag{2.23}$$

where Ψ corresponds to the cost of deploying $\boldsymbol{q}_k$. The total coverage across all RISs is given by:

$$H(\boldsymbol{Q}) = \sum_{\boldsymbol{k}=1}^{K} F(\boldsymbol{q}_k, \boldsymbol{p}) \tag{2.24}$$

The primary objective of the proposed coverage optimization problem is to pinpoint the optimal locations for the RISs to maximize the coverage performance function; this allows us to cover as many blind regions as possible efficiently. The optimization problem is modeled as follows.

Problem 1: *Coverage Maximization through a Single Reflecting RIS.*

$$\begin{aligned} \textbf{(P1)} \quad & \max_{\boldsymbol{Q}} \quad H(\boldsymbol{Q}) \\ & \text{s.t. } \forall k \in \boldsymbol{K}, \quad \|\theta(\boldsymbol{q}_k, \boldsymbol{q}_{AP})\| \leq \frac{\pi}{2} \quad \text{and} \\ & \lambda \boldsymbol{q}_{AP} + (1-\lambda)\boldsymbol{q}_k \in \boldsymbol{Q} \backslash \boldsymbol{B}_{AP}, \lambda \in [0,1]. \end{aligned} \tag{2.25}$$

To illustrate the NP-hardness of Problem **(P1)**, we draw upon a known NP-hard problem—the set cover problem (SCP)—to perform a polynomial-time reduction. In the SCP, we have a finite set X and a collection S of its subsets. The goal is to find a minimal-cost subset cover such that each element in X is included in at least one selected subset.

This paper makes an analogy between Problem **(P1)** and the SCP by considering the regions within a room as set X and the reachable coverage area of each RIS as a subset in collection S.

- A subset cover for the SCP corresponds to a set of RIS configurations that maximizes coverage in Problem **(P1)**.
- Conversely, a solution to Problem **(P1)** would provide a subset cover for the SCP, covering all regions.

This equivalence demonstrates that Problem **(P1)** shares the NP-hard nature of SCP. When the coverage rate $H(\boldsymbol{Q})$ falls below a predetermined threshold C even after a single reflection from the RIS, this paper strategically deploys an additional RIS within the visible region $\boldsymbol{V_k}$ of the existing RISs. This approach exploits the cumulative reflection capabilities of multiple RISs to increase the overall system coverage rate. Let $\boldsymbol{q}_I = \{\boldsymbol{q}_1, \boldsymbol{q}_2, \cdots, \boldsymbol{q}_i\}$ be the RIS location determined by solving Problem **(P1)**.

Problem 2: *Coverage Maximization through the Cooperative Reflection of Multiple RISs.*

$$
\begin{aligned}
\textbf{(P2)} \quad & \max_{\boldsymbol{Q}} \quad H(\boldsymbol{Q}) \\
& \text{s.t. } \forall k \in \boldsymbol{K}, \forall i \in \boldsymbol{I}, \quad \|\theta(\boldsymbol{q}_k, \boldsymbol{q}_i)\| \le \frac{\pi}{2} \\
& \quad \lambda \boldsymbol{q}_i + (1-\lambda)\boldsymbol{q}_k \in \boldsymbol{Q} \backslash \boldsymbol{B}_{AP}, \lambda \in [0,1].
\end{aligned}
\tag{2.26}
$$

2.4.3 Beamforming Optimization

When the optimal locations for RISs are established, adapting the direction of RIS beamforming to account for user mobility becomes critical. The sheer number of elements on a large-scale RIS makes real-time beamforming direction adjustment a challenging task. Given the potential proximity of the user to the RIS, the assumption of identical positions for all RIS elements does not hold. Consequently, this paper designs a near-field codebook, which is then used to adjust the beamforming direction based on the user's position. We divide the total space into L regions, $[\phi_l, \phi_{l+1}]$, with $\phi_{l+1} - \phi_l = \pi/L, \forall l$. To extract the codewords, this paper proposes the following optimization problem:

Problem 3: *Near-Field Codebook Design.*

$$
\begin{aligned}
\textbf{(P3)} \quad & \max_{\boldsymbol{w}} \quad \mathbb{E}\left(|\boldsymbol{w}^H \boldsymbol{h}(\phi)|^2\right) \\
\text{s.t.} \quad & \phi \in (\phi_l, \phi_{l+1}) \\
& \boldsymbol{w}^H \boldsymbol{w} = 1 \\
& |\boldsymbol{w}^H \boldsymbol{h}(\phi')|^2 \le \varepsilon, \text{ for all } \phi' \notin (\phi_l, \phi_{l+1})
\end{aligned}
\tag{2.27}
$$

Here, $\boldsymbol{w}$ signifies the phase configuration on the RIS, $\mathbb{E}(.)$ denotes the expectation operation, $\angle \boldsymbol{h}$ signifies the channel response vector, and ε indicates a threshold for received signal power. The above optimization problems and the corresponding solutions provide a comprehensive strategy for improving the coverage and user experience of indoor wireless communication systems with an RIS.

2.5 Proposed Coverage Optimization and Codebook-Based Optimization

This section unfolds in two segments. First, this paper discusses the proposed novel optimization algorithm—the multiscale spatial search (MSS)—tailored to optimize the placement of the RIS to achieve maximum coverage. Subsequently, we delve into a beamforming optimization method based on the near-field codebook.

2.5.1 Multiscale Spatial Search Algorithm

The core aim of this newly developed optimization algorithm, multiscale spatial search (MSS), is to expand the coverage of the wireless communication system. We breakdown this algorithm into three distinct stages: system initialization, single reflection RIS location optimization, and cooperative reflection RIS location optimization.

Stage I: System Initialization In a given indoor scenario, the set of obstacles $\boldsymbol{O}$, the points outside of obstacles $\boldsymbol{Q}$ and the locations of the APs $\boldsymbol{q}_{AP}$ are generated, as shown in Step 1. Based on the spatial relationship between $\boldsymbol{q}_{AP}$ and $\boldsymbol{O}$, this paper further divides $\boldsymbol{Q}$ into two subsets: $\boldsymbol{Q}_{los} \notin \boldsymbol{B}_{AP}$ and $\boldsymbol{Q}_{nlos} \in \boldsymbol{B}_{AP}$. By applying Eq. (4), the received power from the AP at each point in $\boldsymbol{Q}_{los}$ is calculated, enabling us to determine the initial coverage rate C_{init} against the critical power P_{critic}. C_{init} is calculated as follows:

$$C_{\text{init}} = \frac{\sum_{r \in \boldsymbol{Q}_{\text{los}}} 1\left(P_{\text{los}}^{r} \geq P_{\text{critic}}\right)}{|\boldsymbol{Q}|}, \tag{2.28}$$

where $1(\cdot)$ denotes the indicator function, which equals 1 if the condition inside the parentheses is true and 0 otherwise. We subsequently initialize various parameters used in the algorithm. The process of **stage I** is shown in steps 1–3 in Algorithm 1.

Stage II: Single Reflection RIS Location Optimization In Stage II, this paper evaluates the initial system coverage rate, C_{init}, against a predefined threshold, C. If $C_{init} \geq C$, this negates the necessity for RIS placement. Conversely, if $C_{init} < C$, we proceed by sampling the set $\boldsymbol{Q}_{los}$ at a relatively high resolution, μ, to identify all potential RIS placements within $\boldsymbol{Q}$. For each proposed RIS location, $\boldsymbol{q}_k$, we determine the corresponding visible region, $\boldsymbol{V}_k$. We then scan each point within $\boldsymbol{Q}$ to identify the optimal RIS position, $\boldsymbol{q}_{max}$, which results in the maximization of the performance function $F(\boldsymbol{q}_k, \boldsymbol{V}_k)$, as defined by Eq. (5.24). Given that each RIS incurs a cost, $\boldsymbol{\Psi}$, this paper considers only those RIS placements that yield a positive performance function, $F(\boldsymbol{q}_k, \boldsymbol{p}) > 0$.

Algorithm 1 Multiscale Spatial Search Algorithm

Input: $\boldsymbol{O}$, $\boldsymbol{Q}$, $\boldsymbol{q}_{AP}$ ▷ Stage I
Divide $\boldsymbol{Q}$ into $\boldsymbol{Q}_{los}$, $\boldsymbol{Q}_{nlos}$
Calculate C_{init} via Eq. (28)
while $C_{init} \leq C$ **do** ▷ Stage II
 $\boldsymbol{Q} \leftarrow \text{sample}(\boldsymbol{Q}_{los}, \mu)$, generate $\boldsymbol{q}_k \in \boldsymbol{Q}$
 procedure OPTIMIZE($\boldsymbol{Q}$)
  for $\boldsymbol{q}_k \in \boldsymbol{Q}$ **do**
   $C_{max} \leftarrow 0$, $\boldsymbol{q}_{max} \leftarrow \emptyset$
   Generate $\boldsymbol{V}_k$, calculate C_k via Eq. (5.24)
   if $C_k \geq C_{max}$ **then**
    $C_{max} \leftarrow C_k$, $\boldsymbol{q}_{max} \leftarrow \boldsymbol{q}_k$
   end if
  end for
  if $C_{max} > 0$ **then**
   Add $\boldsymbol{q}_{max}$ to the indoor scenario and calculate the coverage rate of the system C'.
  end if
  return C', $\boldsymbol{q}_{max}$
 end procedure
 for $n = 1$ **to** N **do**
  $\boldsymbol{Q}^n \leftarrow \text{sample}(\boldsymbol{q}_{max}^{n-1}, \mu/\sigma^n) + \xi^n \boldsymbol{Q}_{los}$
  Generate $\boldsymbol{q}_n \in \boldsymbol{Q}^n$
  C_{max}^n, $\boldsymbol{q}_{max}^n \leftarrow \text{OPTIMIZE}(\boldsymbol{Q}^n)$
  if $C_{max}^n - C_{max}^{n-1} > \eta$ **then**
   Continue
  end if
 end for
 Repeat Stage II to find the set of all single-reflection RIS locations $\boldsymbol{q}_I = \{\boldsymbol{q}_1, \cdots, \boldsymbol{q}_i\}$.
end while ▷ Stage II
$C_I \leftarrow$ calculate_coverage for $\boldsymbol{q}_I$
if $C_I < C$ **then** ▷ Stage III
 Search for cooperative reflection RISs
 for $\boldsymbol{q}_i \in \boldsymbol{q}_I$ **do**
  Generate visible_area $(\boldsymbol{V}_i)$
  Generate $\boldsymbol{q}_i \leftarrow$ Repeat Stage II to generate all RIS locations in $\boldsymbol{V}_i$
 end for
end if ▷ Stage III
Output: All RIS locations $\boldsymbol{Q}_k$ and the maximum coverage C_{best}.

As such, the optimal position $\boldsymbol{q}_{max}$ for RIS placement within $\boldsymbol{Q}$ is identified. The corresponding process is outlined in steps 5–16 of **Algorithm 1**. However, owing to computational limitations, the initial sampling resolution, μ, may be too coarse to pinpoint the optimal RIS position accurately. Therefore, after identifying an approximate optimal position, $\boldsymbol{q}_{max}$, we refine this search by dividing the surrounding space at a higher resolution of μ/σ^k, with $\sigma > 1$ as a hyperparameter. Concurrently, to circumvent the placement of the RIS at a local optimum, this paper incorporates a greedy strategy. This strategy allows the RIS to investigate other points within the space based on a decaying probability, ξ, where $\xi < 1$. Once the incremental improvement in coverage rate falls below a prespecified threshold, η, we deem the current resolution optimal, yielding the optimal RIS location $\boldsymbol{q}^n_{max}$ and corresponding coverage rate C^n_{max}. This process is iteratively repeated until all RIS locations, denoted by $\boldsymbol{q}_I = \{\boldsymbol{q}_1, \cdots, \boldsymbol{q}_i\}$, that satisfy the requirements have been established.

Stage III: Cooperative Reflection RIS Location Optimization Upon completion of Stage II, all the established RISs, $\boldsymbol{q}_I$, are positioned within the room, and the resulting coverage rate, denoted as C_I, is computed. If $C_I < C$, the situation calls for cooperative reflection involving multiple RISs. By employing Eq. (5.22), the visible area for each $\boldsymbol{q}_i$ is defined as $\boldsymbol{V}_i$. Each N_i is then treated as an AP for the points within $\boldsymbol{V}_i$. Following this, the steps in Stage II are replicated to ascertain the optimal locations for the $\boldsymbol{q}_J$ RISs, denoted as $\boldsymbol{q}_J = \left\{\boldsymbol{q}_1, \boldsymbol{q}_2, \cdots, \boldsymbol{q}_j\right\}$. As a result, the MSS algorithm yields the combined set of optimal RIS locations, $\boldsymbol{Q}_k$, along with the maximum coverage rate, C_{max}.

Complexity Analysis: The complexity of the proposed MSS algorithm primarily arises from two stages. More specifically, the complexity of Stage II, which involves single reflection RIS location optimization, is proportional to the product of the number of sampling points and the number of iterations in the optimization process. This complexity can be approximated as $O(N \cdot n)$. In Stage III, which involves cooperative reflection RIS location optimization, the complexity is dependent on the number of RISs determined in Stage II and the number of potential RIS locations, resulting in a complexity of approximately $O(M \cdot N)$. Consequently, the overall complexity of the algorithm is approximately $O(N \cdot n + M \cdot N)$, which makes it suitable for practical applications, especially in scenarios with a reasonable number of obstacles and RISs. The process of the MSS algorithm is summarized in **Algorithm 1**.

2.5.2 Near-field Codebook Design

After determining the placement of the RISs, hierarchical near-field codebook-based optimization is proposed to optimize the cooperative beamforming of RIs. The codebook, denoted by $\boldsymbol{W}_L = \{\boldsymbol{w}_1, \boldsymbol{w}_2, ..., \boldsymbol{w}_l\}$, comprises unit-norm vectors $\boldsymbol{w}_l \in \mathbb{W}^{N \times M}$. Each vector

Algorithm 2 Near-field Codebook Design

1: Initialize $\boldsymbol{W}_L \leftarrow \emptyset$
2: Randomly generate $\boldsymbol{w}_l$
3: Partition the 3D space into regions $L = \{1, ..., l\}$
4: **for** each *region* $\in L$ **do**
5:     **while** not achieving $|\boldsymbol{w}^H \boldsymbol{h}(\phi')|^2 \leq \varepsilon$ **do**
6:         **for** each *row* of *RIS* **do**
7:             Adjust the phase configuration in *row* based on Eq. (5.16)
8:             Maximize $\boldsymbol{E}\left(|\boldsymbol{w}^H \boldsymbol{h}|^2\right)$ in target *region* subject to $\angle \boldsymbol{h} \in (\phi_l, \phi_{l+1})$ and $\boldsymbol{w}^H \boldsymbol{w} = 1$
9:         **end for**
10:     **end while**
11:     Append the optimized configuration of *RIS* as a $\boldsymbol{w}_l$ to $\boldsymbol{W}_L$
12: **end for**
13: **return** $\boldsymbol{W}_L$

represents the phase of a corresponding element. In practice, every element is subject to a limited phase shift. The constraint is defined as:

$$\mathfrak{N} = \left\{\frac{\pi}{1}, \frac{\pi}{2}, \cdots, \frac{\pi}{2^n}, n \in \mathbb{N}\right\}. \tag{2.29}$$

Here, n represents the number of feasible phase shifts. The proposed codebook design procedure is detailed in **Algorithm 2**, which commences with initializing an empty RIS codebook, $\boldsymbol{W}_L$, and randomly generating the codeword $\boldsymbol{w}_l$ (Steps 1–2). The algorithm then partitions the 3D space into l regions, symbolized by $L = \{1, ..., l\}$ (Step 3). Each region corresponds to a specific interval of phase constraints, denoted as (ϕ_l, ϕ_{l+1}), where ϕ indicates the phase. Following this division, the algorithm proceeds to optimize the RIS configuration for each region (Step 4). The iterative optimization continues until the squared absolute value of the received signal, $|\boldsymbol{w}^H \boldsymbol{h}(\phi')|^2$, reaches the predefined threshold ε (Step 5). Each iteration within a region evaluates every row of the RIS (Step 6). The phase configuration of a row is then adjusted via Eq. (5.16) (Step 7). Simultaneously, the algorithm aims to maximize the expected value of the squared absolute value of the received signal, $\mathbb{E}\left(|\boldsymbol{w}^H \boldsymbol{h}|^2\right)$, in the target region (Step 8). This maximization is subject to the power constraint $\boldsymbol{w}^H \boldsymbol{w} = 1$ and the phase constraint $\angle \boldsymbol{h} \in (\phi_l, \phi_{l+1})$ for the current region. After the optimization process converges, the resulting optimal RIS configuration for the current region is appended to the RIS codebook as a codeword, $\boldsymbol{w}_l$ (Step 9). This procedure is repeated until all the regions in L have been optimized. The algorithm ultimately produces a comprehensive RIS codebook, $\boldsymbol{W}_L$, featuring region-specific codewords encapsulating optimal RIS configurations (Step 10).

2.5.3 Hierarchical Codebook-Based Optimization

A hierarchical codebook-based beamforming optimization algorithm is proposed to reduce the beam training overhead. The hierarchical codebook approach aims to reduce the overall computational complexity by performing optimizations in progressively smaller search spaces. The proposed algorithm operates in two primary phases: the probe phase, in which an optimal codeword from the hierarchical codebook is selected for each user location, and the communication phase, in which the chosen codeword is used to maximize the signal strength.

Algorithm 3 Maximizing Signal Strength with the Hierarchical Near-field Codebook (HNCB)

Initialize the user locations $\leftarrow \boldsymbol{P}$, $P_{max} \leftarrow 0$
The number of codebook levels is K, the sampling area is R^1, and the division step length is Δ^1.
$s_k = 0$, $\boldsymbol{w}_{k,best} = 0$ and $s_{k,best} = 0$ ▷ Probe Phase
for each $\boldsymbol{p} \in \boldsymbol{P}$ **do**
  for $k = 1, 2, \ldots, K$ **do**
    Divide the entire space R^k using the divide step length Δ^k, generating L^k regions
    Generate $\boldsymbol{W}_L^k$ via Algorithm 2
    for each $\boldsymbol{w}_l^k$ in $\boldsymbol{W}_L^k$ **do**
      $s_k = s_k + 1$
      Set RIS with $\boldsymbol{w}_l^k$
      AP sends a pilot signal $\boldsymbol{S}$
      RIS uses $\boldsymbol{w}_l^k$ to reflect $\boldsymbol{S}$
      Users collect received_signal_strength $\boldsymbol{p}_l^k$
      if $\boldsymbol{p}_l^k > P_{max}^k$ **then**
        $P_{max}^k \leftarrow \boldsymbol{p}_l^k$, $\boldsymbol{w}_{k,best} \leftarrow \boldsymbol{w}_l^k$, $s_{k,best} \leftarrow s_k$
      end if
    end for
    Choose R^{k+1} based on $s_{k,best}$, $\Delta^{k+1} = \delta\Delta^k$
  end for
  The optimal codeword index $s_{K,best}$ for the user.
end for
Output: A dictionary $\boldsymbol{Q}$, where each user location $\boldsymbol{p}$ corresponds to an optimal index $s_{K,best}$
▷ Communication Phase
Set the RIS with $s_{K,best}$ in the codebook to maximize the received signal strength for user $\boldsymbol{p}$
Repeat the probe phase periodically to accommodate changes in the environment or user locations

During the probe phase, the algorithm first determines the number of codebook levels K, the initial sampling area R^1, and the initial division step length Δ^1. For each user location $\boldsymbol{p} \in \boldsymbol{P}$, the algorithm iterates over K hierarchical levels:

1. At the first level $k = 1$, the algorithm divides the entire space R^1 using the large step length Δ^1, generating L^1 regions. Since the initial step length is large, the size of the codebook at this level is relatively small, allowing for quick traversal and identification of the best region.

2. Based on the best region from the first level, the algorithm proceeds to the next level $k = 2$, using a smaller step length Δ^2 to further divide the best region into L^2 smaller regions. This process continues, with each subsequent level refining the search space further until the K-th level is reached.

At each level k, for each generated region $\boldsymbol{w}_l^k$, the algorithm calculates the received signal strength $\boldsymbol{p}_l^k$ and compares it with the current maximum signal strength $P_{\max}^k$. If $\boldsymbol{p}_l^k > P_{\max}^k$, it updates $P_{\max}^k$, the best codeword $\boldsymbol{w}_{k,\text{best}}$, and the best codeword index $s_{k,\text{best}}$. After all the codewords at the current level are evaluated, the algorithm selects the next level's region R^{k+1} based on $s_{k,\text{best}}$ and updates the divide step length to $\Delta^{k+1} = \delta\Delta^k$. This hierarchical search method allows the algorithm to find the optimal codeword effectively within a smaller search space, significantly reducing computational complexity. During the subsequent communication phase, the RIS is set according to the best codeword associated with a given user location $\boldsymbol{p}$. This setting guarantees the maximization of the received signal strength for each user. To account for any changes in the environment or user locations, the probe phase is periodically repeated, enabling the system to adapt dynamically.

By leveraging this two-phase optimization algorithm, an adaptive communication protocol can be established. The proposed protocol not only maximizes the received signal strength at each user location but also accommodates changes in the environment and user movements, making it a potential approach for optimizing RIS-aided communication networks.

2.6 Simulation Results

In this section, extensive simulation experiments are conducted to demonstrate the performance of the proposed optimization algorithm. First, three distinct scenarios are established to validate the performance of the proposed MSS algorithm while exploring the impact of different experimental parameter settings on the performance of the MSS. The optimization performance of the proposed HNCB method is subsequently verified under various scenarios.

2.6.1 Validation of the proposed MSS algorithm

To validate the effectiveness of the proposed MSS algorithm comprehensively, three diverse simulation scenarios are established. Each scenario represents a distinct configuration, including a single RIS, two cooperative RISs, and multiple RISs, as displayed in Fig. 2.5. The key parameters common to all the simulation scenarios are summarized in Table II.

Table 2.2 Simulation Parameters

Parameter	Value	Description
G_tP_t	30 dBm	EIRP for AP
P_{th}	-70 dBm	Received Power Threshold
λ	5×10^{-3} m	Wavelength
f	60 GHz	Communication Frequency
M	120	Number of Rows
N	120	Number of Columns
G_r	0 dB	User Gain
C	0.9	Desired Coverage Threshold
η	0.01	Improvement Threshold for Coverage
μ	4	Initial Sampling Resolution
σ	3	Resolution Refinement Factor
ξ	0.1	Greedy Exploration Decay Factor

Table 2.3 Performance Metrics in Various Simulation Scenarios W/ and W/O RIS

	Room_size	AP_location	OBs_center_location	OBs_size	RIS_location	w/o_RIS	w/_RIS
Scenario A	[30, 30, 10]	[0, 15, 6]	[14.5, 18.0, 5.0]	[1, 24, 10]	[15.4, 0.0, 5.4]	51.51%	98.50%
Scenario B	[30, 30, 10]	[0, 15, 6]	[10.5, 20.0, 5.0] [15.0, 9.5, 5.0]	[1, 20, 10] [10, 1, 10]	[20.1, 0.0, 5.4] [30.0, 11.0, 5.0]	42.66%	97.82%
Scenario C	[50, 50, 10]	[25, 25, 10]	[5.5, 15.0, 4.0] [35.5, 40.0, 5.0] [17.5, 35.5, 5.0] [35.5, 15.0, 4.0] [20.5, 10.5, 4.0] [17.5, 42.5, 1.0] [17.5, 22.5, 2.5]	[1, 10, 8] [1, 10, 10] [35, 1, 10] [1, 10, 8] [11, 1, 8] [5, 5, 2] [5, 5, 5]	[31.1, 0.0, 5.8] [50.0, 46.0, 7.0] [7.0, 0.0, 5.0] [46.0, 50.0, 7.0]	59.77%	92.95%

This paper conducted a comprehensive analysis of three distinct scenarios—Scenarios A, B, and C. Each scenario is characterized by unique variations in room size, AP location, OB position and dimensions. The detailed configurations and outcomes for each scenario are provided in Table III and are visually represented in Fig. 2.5.

In Scenario A, the room is 30 m long, 30 m wide, and 10 m high. The AP is located at [0,15,6]. The obstacle is centered at [14.5, 18, 5], with dimensions of 1 m in length,

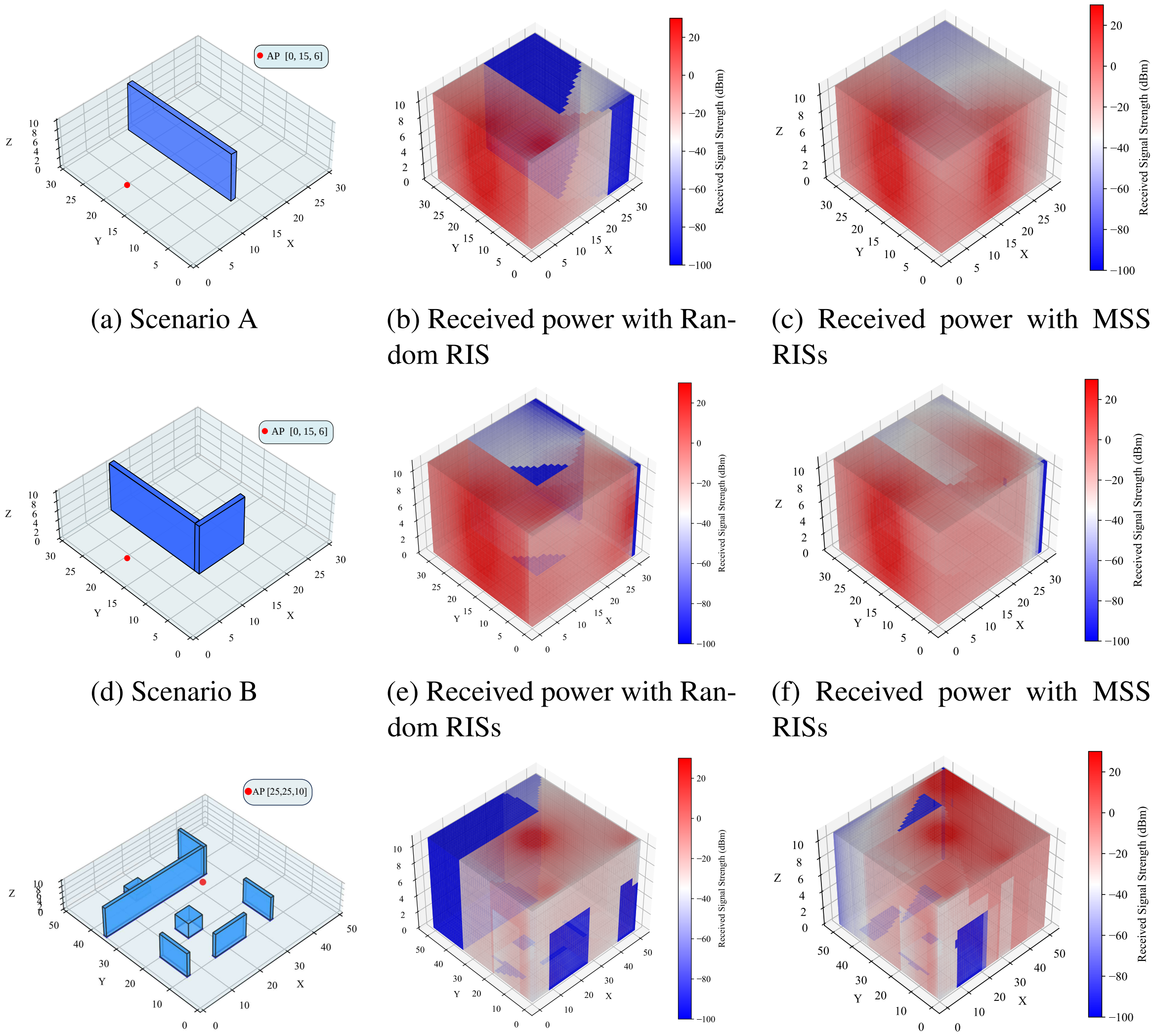

(a) Scenario A
(b) Received power with Random RIS
(c) Received power with MSS RISs
(d) Scenario B
(e) Received power with Random RISs
(f) Received power with MSS RISs
(g) Scenario C
(h) Received power with Random RISs
(i) Received power with MSS RISs

Fig. 2.5 Coverage rate optimization via the MSS for three different scenarios. The first column of Fig. 2.5 shows three different simulation scenarios, the second column shows the signal power map with random RISs, and the third column shows the signal power map with MSS RISs.

24 m in width, and 10 m in height. The RIS is positioned at [15.4, 0, 5.4]. With the random deployed RIS, the performance was 59.51%, which increased to 98.50% upon RIS implementation, indicating a significant improvement. Scenario B, with the same room dimensions as Scenario A, introduces increased complexity with multiple OBs and RIS locations. This scenario confirms the effectiveness of cooperative reflection between RISs, showing coverage of 60.12% with the random RISs and enhancing performance to 97.82% with RIS deployment. Scenario C, which is designed to emulate an extensive environment, underscores the scalability and adaptability of the proposed algorithm. In a room of size [50, 50, 10] with seven OBs and four RIS locations, the performance with random RISs was 69.74%, whereas the incorporation of an RIS yielded a substantial coverage of 92.95%.

The experimental analysis underscores the efficacy and adaptiveness of the MSS algorithm, particularly in complex and larger environments. Strategic RIS deployment significantly improves wireless signal coverage, thereby optimizing network performance.

2.6.2 Benchmarking Algorithms

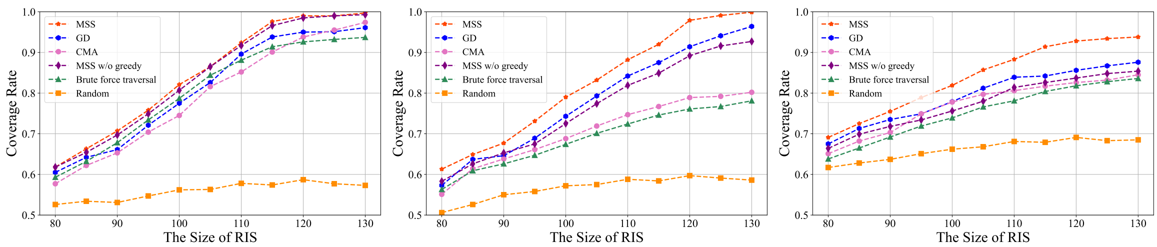

(a) Scenario A (b) Scenario B (c) Scenario C

Fig. 2.6 Comparative analysis of coverage performance. This figure presents three subplots depicting the coverage performance of the MSS and other comparison algorithms in three distinct scenarios. Fig. 2.6(a) shows the comparison in Scenario A, Fig. 2.6(b) presents the performance in Scenario B, and Fig. 2.6(c) shows the results in Scenario C. Across all the scenarios, MSS consistently achieves superior coverage, underscoring its effective deployment strategies and adaptive nature

.

This section compares the performance of the proposed MSS algorithm with that of the following baseline methods.

- *Gradient descent (GD)* [97]: GD is an iterative coverage expansion algorithm based on gradient descent to optimize the locations and orientations of multiple RISs to maximize network coverage.

- *Coverage maximization algorithm (CMA)* [96]: CMA is the optimization algorithm in [96], which optimizes the coverage of the network by optimizing the RIS orientation and horizontal distance.
- *MSS w/o greedy*: MSS w/o greedy method means the proposed MSS algorithm without a greedy component.
- *Brute force traversal*: This legend corresponds to sequentially traversing all possible points, generating points at a constant step length of 1.
- *Random*: The random algorithm means that RISs are randomly placed in the region with an existing LoS link with the AP.

Fig. 2.6 shows a comparison of the coverage rate results of the different methods in three distinct scenarios. For simplicity, this paper assumes that the number of elements in a row, represented by N and M, is equal to the size of the RIS. All six methods show a consistent trend of increasing coverage rates with increasing RIS size due to the greater path gain provided by the increased number of RIS elements. Compared with the other baselines, the proposed MSS method achieves a higher coverage rate across all three scenarios, demonstrating its efficient utilization of the RIS in various complex environments. The GD and CMA methods improve coverage with increasing RIS size but fall short of the MSS algorithm. This is because the MSS method employs a multiscale spatial search strategy, which iteratively divides the space at higher resolutions to pinpoint more precise locations for RIS placement. The MSS w/o greedy method performs similarly to the MSS in Scenario A but underperforms in the more complex Scenarios B and C. As the complexity of the scenario increases, the MSS w/o greedy method is more prone to becoming trapped in local optima, highlighting the importance of the greedy strategy. Furthermore, the brute force traversal method outperforms only the random method, as it struggles to effectively handle the RIS placement problem in scenarios involving cooperative reflections among multiple RISs.

Fig. 5.7 presents the coverage performance against the number of obstacles. In this simulation, each obstacle has a fixed size of 8m $\times$ 8m $\times$ 8m, and the positions of the obstacles are randomly generated in each experiment to simulate various real-world scenarios. The AP is fixed at the position [25, 25, 10] in a room of size 50 m $\times$ 50 m $\times$ 10 m. To ensure reliability, 100 experiments were conducted for each number of obstacles, and the coverage rates were averaged. As shown in Fig. 5.7, the coverage rates for all methods generally decrease as the number of obstacles increases. This decline is attributed to the increased signal blockage caused by more obstacles. Moreover, the proposed MSS consistently outperforms other methods in terms of coverage across all obstacle scenarios, maintaining approximately 76%

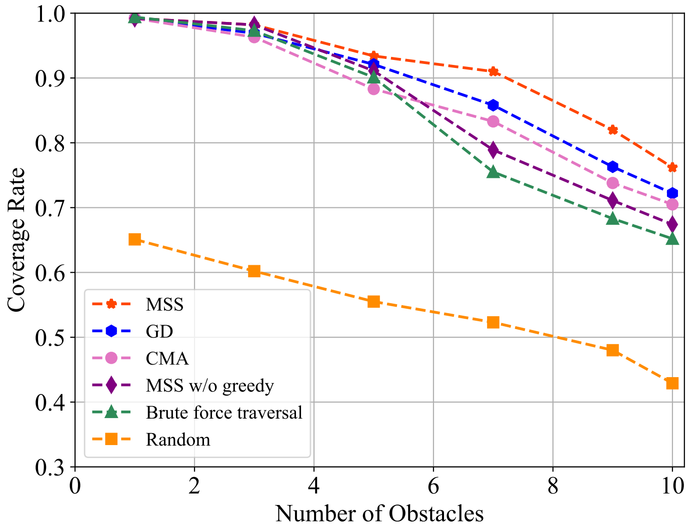

Fig. 2.7 Coverage rates of various methods versus the number of obstacles.

coverage even in the presence of ten obstacles. This finding demonstrates the effectiveness and adaptiveness of the proposed MSS method.

Furthermore, the results of Figs. 2.6 and 5.7 indicate that the proposed MSS method achieves the highest coverage rates across various indoor scenarios and RIS sizes compared with other algorithms, demonstrating the effectiveness and adaptiveness of the proposed approach.

2.6.3 Validation of Proposed HNCB Algorithm

Fig. 5.8 provides a visual representation of the optimized beamforming technique applied following the optimized placement of the RIS, as achieved through the proposed proposed HNCB method. This figure demonstrates how the beamforming strategy specifically targets a region defined by $\varphi_r = \pi/4, \theta_r = \pi/4$ when the receiver distance is $d_r = 1$ m and the transmitter distance is $d_t = 30$ m. The proposed HNCB method optimizes system performance by intelligently focusing signal power where it is most beneficial, thereby maximizing resource utilization efficiency.

Fig. 5.9 compares the performance of five beamforming methods across varying RIS sizes, including perfect CSI beamforming, HNCB, MARISA [3], the Far-field Codebook [62], and a random phase configuration strategy. The perfect CSI beamforming method, which has perfect CSI allowing for precise adjustment of the beamforming direction, is chosen as the upper bound for performance comparison. The results show that, in addition to the perfect CSI beamforming method, the proposed HNCB consistently delivers higher

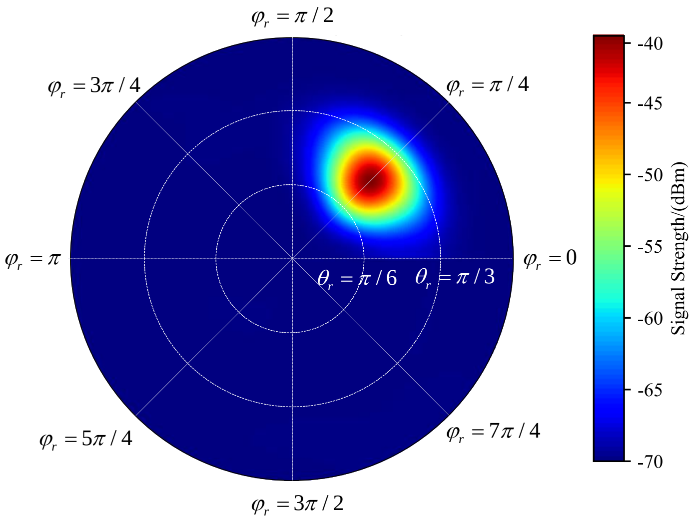

Fig. 2.8 Visualization of optimized beamforming via HNCB targeting a specific region in the near-field case where $d_r = 1$ m and $d_t = 30$ m.

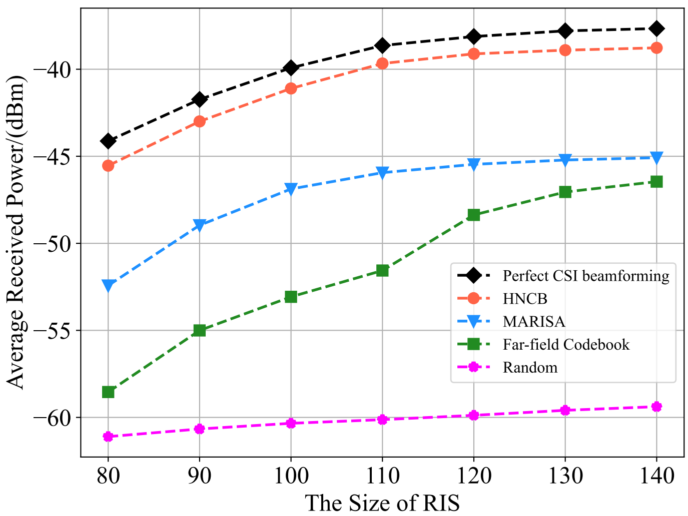

Fig. 2.9 Comparison of the average received power across different RIS sizes for various beamforming methods.

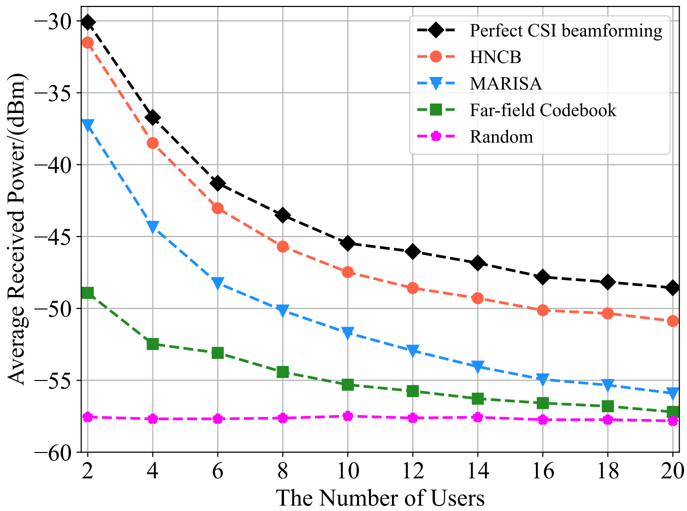

Fig. 2.10 Average received power variation with increasing user number for different beamforming methods

average received power than other algorithms across all RIS sizes. The superior performance is attributed to the ability to customize the phase adjustment according to the unique position of each RIS, effectively concentrating the signal power toward the user. MARISA, which adjusts the phase of RIS elements based solely on the angle, performs worse than HNCB does, highlighting the advantage of HNCB's position-based phase adjustment. However, it still outperforms the far-field codebook and random methods, indicating relative effectiveness when position information is not readily available. Despite the theoretical advantage in large-scale scenarios, the Far-field Codebook method performs less than HNCB and MARISA do, suggesting that near-field codebook methods such as HNCB might be more advantageous in practical applications with moderate RIS sizes. As expected, the random phase configuration yields the lowest average received power across all RIS sizes. These observations underscore the value of phase adjustment strategies such as HNCB, which utilize intelligent beamforming techniques to maximize user-end power reception. The results indicate that the proposed HNCB method achieves performance close to the upper bound, effectively adjusting the beamforming direction and enhancing the received signal strength for users.

As depicted in Fig. 4.8, the average received power tends to decrease with an increase in the number of users due to the shared nature of wireless communication resources. The results show that, in addition to the perfect CSI beamforming method, HNCB maintains a higher average received power than the other methods do, even with increasing users. By focusing the power on each user, HNCB ensures that each user can still experience relatively high received power, improving the overall system performance.

2.7 Conclusion

A novel framework for optimizing large-scale RIS deployment and cooperative beamforming in complex indoor environments is presented. The proposed approach incorporates an efficient MSS algorithm for RIS placement and an HNCB method for beamforming optimization. The proposed framework has demonstrated superior performance in maintaining high coverage and maximizing signal strength across various scenarios. The simulation results underscore the potential of the proposed approach in enhancing the performance of RIS-assisted wireless communication systems, especially in indoor settings. Future research could delve into more intricate scenarios and varied user mobility patterns, further broadening the applicability of the proposed approach.

Chapter 3

Optimization of RIS Beamforming Based on User Behaviors for High-Efficiency Service

3.1 Motivation

The successful deployment of 5G has paved the way for numerous emerging technologies, including virtual reality, the metaverse, and automated driving. These innovative applications necessitate elevated transmission rates and enhanced stability in communication systems beyond the capabilities of traditional technologies. The conventional communication paradigm, influenced by the propagation environment, struggles to ensure consistent transmission rates, thus diminishing the user's QoE. In response, we aspire to devise an intelligent wireless communication system that tailors the user's transmission rate according to their specific requirements [89].

The attainment of this goal calls for a groundbreaking technology capable of continual environmental sensing and direction control of signal propagation. Capitalizing on advancements in synthetic materials, a metasurface known as "Reconfigurable Intelligent Surface (RIS)" has emerged to create an intelligent propagation environment capable of reflecting incident signals in the desired direction. Specifically, RIS comprises a multitude of nearly passive and cost-effective reflecting elements, each capable of independently modifying the phase shift of the incident signals. When the downlink transmission rate from the Base Station (BS) to users falls short of user requirements, the flexible configuration of the signal phase via RIS can enhance signal strength. Because RIS can be seamlessly integrated into existing network architectures without significant hardware modifications, it is deemed a promising technology for future networks [47]. Nevertheless, RIS-assisted MIMO smart communication systems present several challenges: **(i) High computational complexity**: Optimizing the received signal strength for all users simultaneously in RIS-assisted multiple users wireless communication systems introduces significant computation. **(ii) Dynamically changing environment**: Environmental dynamics lead to variations in the channel, necessitating real-time Channel State Information (CSI) acquisition for the RIS-assisted communication system. **(iii) Differentiation of user demands**: As user transmission rate demands fluctuate over time, RISs must adjust the beamforming direction accordingly.

The immense potential of RIS has motivated extensive research to optimize the performance of RIS-assisted wireless communication systems [6, 11]. Fu *et al.* investigated RIS-assisted MIMO non-orthogonal multiple access (NOMA) systems and proposed an alternating difference-of-convex (DC) method to minimize the transmitter's power [17]. In another work, the author introduced a fractional programming method to maximize the sum rate of the communication system, employing three distinct iterative algorithms to optimize the reflection coefficient based on the different types of RIS reflective elements [27]. A ranking algorithm based on combined channel strength was proposed to ensure user fairness, achieving performance close to the theoretical upper limit [87]. However, most existing research concentrates on exploring the optimal configuration of RIS under specific CSI, neglecting the dynamic changes in the environment over time.

Artificial Intelligence (AI) advancements have seen Deep Reinforcement Learning (DRL) emerge as an excellent technique for handling vast amounts of data and mathematically intractable non-linear non-convex problems. Unlike traditional optimization approaches, DRL-based algorithms can learn features directly from data without depending on predefined mathematical models, making them more adaptive to environmental changes. A DDPG-based algorithm was proposed to maximize the sum rate by jointly designing continuous transmit beamforming and RIS phase shifts [25]. Zhang *et al.* introduced a DRL-based algorithm to maximize throughput under imperfect CSI by modeling the return distribution for each state-action pair using a quantile regression method.

In another work, Liu *et al.* considered a RIS-assisted terahertz VR network. Initially, the authors implemented a recurrent neural network (RNN) to predict each user's Line-of-Sight (LoS) or Non-Line-of-Sight (NLoS) status, then employed DRL to select the appropriate reflection coefficient matrix for users in NLoS areas [40]. However, existing research has largely overlooked the diversity of users' demands [92].

In light of the previous analysis, we introduce a RIS-assisted MU-MIMO smart wireless communication system in this paper. The RIS is optimally configured based on user traffic prediction results. An online LSTM module is proficient in capturing temporal correlations between historical network traffic data and is implemented to predict users' network traffic at the subsequent time step. Following this, the RIS reflecting elements are reconfigured based on network traffic predictions to optimize users' QoE. Specifically, we propose a DRL-based algorithm to select the optimal phase shifts of RIS elements. The primary contributions of this paper are summarized as follows:

- We introduce an online LSTM algorithm to predict users' future network traffic by leveraging the temporal correlation of users' historical network traffic. The predicted traffic is then utilized to determine if a user requires an increased transmission rate through RIS beamforming.
- For the first time, we propose a DRL-based algorithm that considers demand differentiation to explore the optimal joint design of RIS phase shifts and transmit beamforming.
- Extensive experiments demonstrate that the proposed optimization methods based on users' network traffic predictions significantly enhance their QoE. Furthermore, our proposed optimization algorithm achieves approximately twice the QoE of a solution with random RIS phase shifts.

The structure of the remainder of this paper is as follows: In Section II, we present the system model and formulate the optimization problem. The proposed L-DRL approach, including its design and implementation, is detailed in Section III. In Section IV, we validate the effectiveness of our proposed methodology through simulation experiments, while Section V presents conclusions.

3.2 System Model & Problem Formulation

This section introduces the Hybrid Reconfigurable Intelligent Surface (HRIS) concept and its application to a communication system scenario. The problem of network traffic prediction is then presented as a means of enhancing communication performance. Based on these analyses, the optimization problem is formulated.

3.2.1 System Model

As depicted in Fig. 3.1a, we contemplate a scenario including one Base Station (BS) with M antennas, K User Equipments (UEs), each with a single antenna, and an HRIS with N reflecting elements. We consider two links: a direct LoS link from BS to users and an indirect link where the HRIS reflects user signals. Both links serve to provide communication

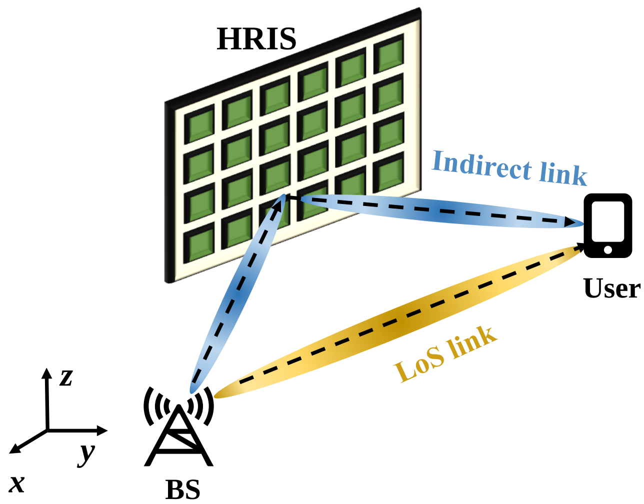

(a) The HRIS-assisted MU-MIMO communication system.

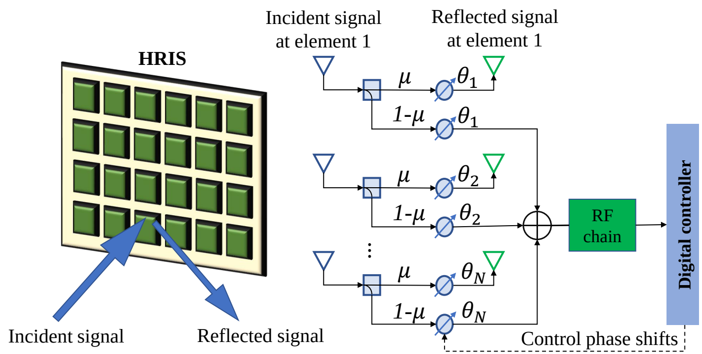

(b) The structure of HRIS.

Fig. 3.1 (a) The HRIS-assisted MU-MIMO communication system. (b) The structure of HRIS.

services for users. The HRIS, employed in our communication system, aids in obtaining the CSI of the indirect link more effectively. An HRIS is an array of hybrid elements capable of reflecting and sensing incident signals simultaneously [86]. As shown in Fig. 3.1b, in the HRIS architecture, each element is combined with a directional coupler that transmits the absorbed power of the incident signals toward radio frequency (RF) hardware, which estimates the CSI of the incident channel. The percentage of the incident signal reflected for communication is denoted by $\mu \in [0,1]$. A detailed description of HRIS can be found in [4].

We use $\boldsymbol{h}_{r,k} \in \mathbb{C}^{(1\times M)}$, $\boldsymbol{G} \in \mathbb{C}^{(N\times M)}$, and $\boldsymbol{h}_k \in \mathbb{C}^{(1\times N)}$ to denote the BS-UE$_k$ channels, BS-HRIS channels, and HRIS-UE$_k$ channels, respectively.

The received signal strength by user k can thus be expressed as:

$$y_k = \left(\sqrt{\mu}\boldsymbol{h}_k\boldsymbol{\Theta}\boldsymbol{G} + \boldsymbol{h}_{r,k}\right)\boldsymbol{W}\boldsymbol{x} + n_k \tag{3.1}$$

where $\blacksquare = \text{diag}\left[\beta_1 e^{j\theta_1}, \cdots, \beta_N e^{j\theta_N}\right]$, with $\theta_i \in [0,2\pi]$ and $|\beta_i|^2 \leq 1$, $\forall i = 1,2,\cdots,N$ represents the phase shifts and the amplitude ratio by the HRIS. The transmit precoding matrix of the BS denoted as $\boldsymbol{W} \in \mathbb{C}^{M\times K}$, has its k-th column w_k representing the transmit precoder for UEk. Moreover, $\boldsymbol{x} \in \mathbb{C}^{K\times 1}$ represents the transmitted data from the BS to all users that satisfy the conditions $\mathbb{E}\left[|xk|^2\right] = 1$. Assuming that the maximum transmit power of the BS is P_t, the constraint $\mathbb{E}\left[|\boldsymbol{W}\boldsymbol{x}|^2\right] \leq P_t$ is satisfied. In addition, $n_k \sim \boldsymbol{CN}(0,\delta^2)$ denotes Gaussian white noise with variance δ^2.

From (5.1), the received signal of UEk can be further expressed as:

$$\begin{aligned} y_k = \left(\sqrt{\mu}\boldsymbol{h}_k\boldsymbol{\Theta}\boldsymbol{G} + \boldsymbol{h}_{r,k}\right) w_k x_k + \sum_{n,n\neq k}^{K} \\ \left(\sqrt{\mu}\boldsymbol{h}_n\boldsymbol{\Theta}\boldsymbol{G} + \boldsymbol{h}_{r,n}\right) w_n x_n + n_k \end{aligned} \tag{3.2}$$

Here, $\sum_{n,n\neq k}^{K}\left(\boldsymbol{h}_n\boldsymbol{\Theta}\boldsymbol{G} + \boldsymbol{h}_{r,n}\right)\omega_n x_n$ represents the interference of other users' signals on UE$_k$.

From (5.2), the Signal-to-Interference-plus-Noise Ratio (SINR) at UE$_k$ is given as:

$$\gamma_k = \frac{\left|\left(\sqrt{\mu}\boldsymbol{h}_k\boldsymbol{\Theta}\boldsymbol{G} + \boldsymbol{h}_{r,k}\right) w_k\right|^2}{\sum_{n=1,n\neq k}^{K}\left|\left(\sqrt{\mu}\boldsymbol{h}_n\boldsymbol{\Theta}\boldsymbol{G} + \boldsymbol{h}_{r,n}\right) w_n\right|^2 + \sigma_n^2} \tag{3.3}$$

Therefore, the transmission rate of UEk can be expressed as:

$$R_k = \log_2(1+\gamma_k). \tag{3.4}$$

3.2.2 Network Traffic Prediction

In a multi-user communication system, transmission speed demand varies among users at any given time. Precise traffic prediction allows the HRIS to direct beamforming toward users experiencing high network traffic in advance, enhancing user QoE. Consequently, accurate traffic prediction facilitates a more effective intelligent wireless propagation environment.

Due to its temporal correlation with users' network traffic, historical data can be leveraged to predict future traffic. These predictive results are then compared against the transmission rate provided by the LoS channel, denoted by $\boldsymbol{h}_{r,k}\boldsymbol{W}\boldsymbol{x}$, to identify which users require improved QoE through HRIS. This approach prioritizes users demanding higher transmission rates during the joint beamforming process of both BS and HRIS, thereby enhancing the communication system's overall performance. The traffic prediction problem can be formally modeled follows:

$$y_k^{t+1} = f(y_k^{t-P+1}, \cdots, y_k^t) \tag{3.5}$$

where y_k^{t+1} denotes the network traffic of UE_k at the time slot $t+1$, and $y_k^{t-P+1}, \cdots, y_k^t$ represents the historical wireless traffic demands for UE_k. The prediction accuracy is defined as:

$$\beta(t) = 1 - \frac{1}{K}\sum_{k=1}^{K}\left|\frac{y_k^t - \hat{y}_k^t}{y_k^t}\right| \tag{3.6}$$

Here, $\hat{y}_k^t$ signifies the predicted value for user k at time t, while $\beta(t)$ represents the prediction accuracy at the same time.

3.2.3 Problem Formulation

The QoE is contingent upon the wireless system's ability to fulfill the transmission rate requirements of users. Consequently, we propose the following definition for users' QoE:

$$\mathrm{QoE}_k(t) = \beta(t)\tanh\left(10\log\frac{R_k(t)}{R'_k(t)}\right) \tag{3.7}$$

Where $R'_k(t)$ represents the user-requested transmission rate derived from our prediction, while $R_k(t)$ denotes the actual transmission rate at time t. This meticulously engineered function optimizes the user experience while efficiently managing resources.

This study introduces a communication system design optimizing $\boldsymbol{\Theta}$ and $\boldsymbol{W}$ to maximize users' long-term QoE, formally expressed as

$$\begin{aligned} & \max \sum_{i=t}^{\infty} \sum_{k=1}^{K} \mathrm{QoE}_k(i) \\ & s.t. \quad \|\boldsymbol{W}\|^2 \leqslant P_t \\ & \qquad\quad 0 \leqslant \theta_n \leqslant 2\pi, \forall n = 1, \ldots, N \end{aligned} \tag{3.8}$$

Given that the complexity of the problem presented in Equation (5.6) escalates exponentially with the number of HRIS elements, it is classified as an NP-hard problem. To address this complex optimization issue, we employ a DRL-based algorithm as a solution.

3.3 Learning Algorithm for MIMO System

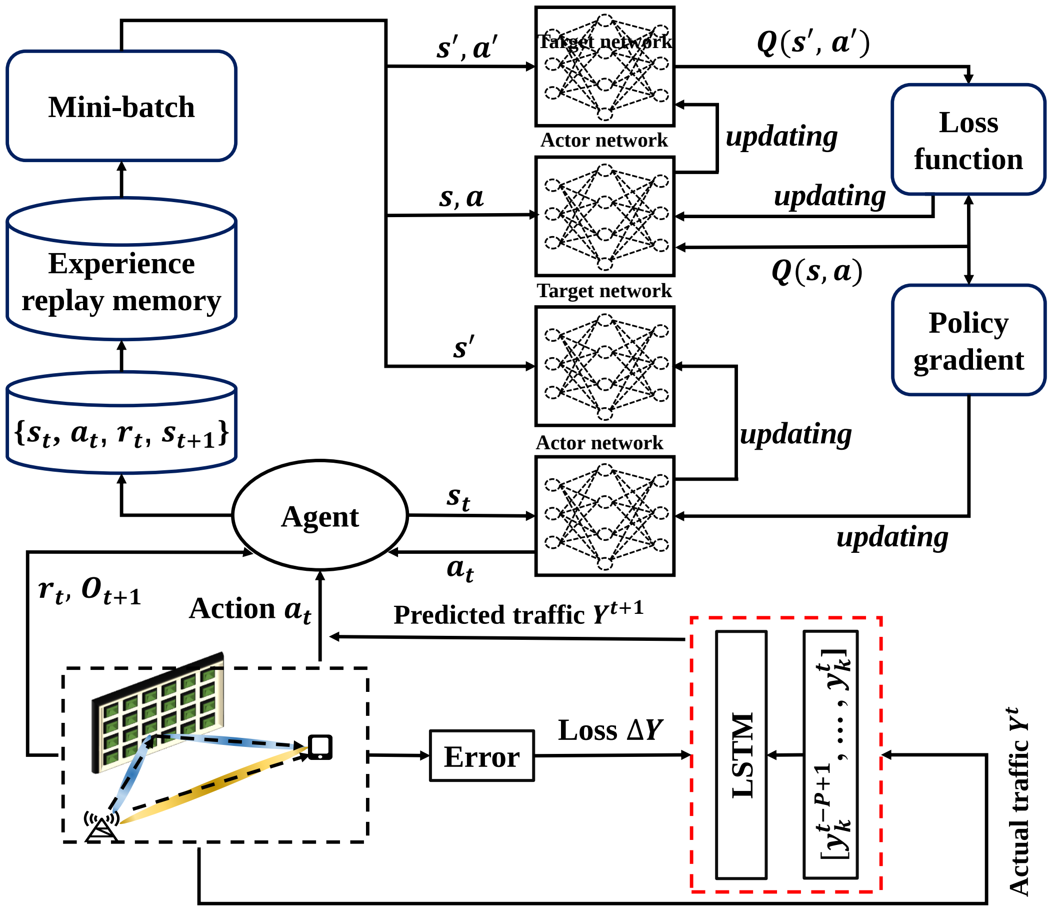

Fig. 3.2 L-DRL algorithm for HRIS-assisted wireless communication system.

This section presents a novel L-DRL algorithm that addresses the optimization problem outlined in Equation (5.6). The L-DRL algorithm incorporates online LSTM and DDPG components, as depicted in Fig.5.2.

Utilizing network traffic as an input, the L-DRL algorithm selects the optimal joint design of the HRIS configuration and BS precoding matrix via continuous interaction with the radio propagation environment.

3.3.1 The Algorithm for Network Traffic Prediction

This study employs an online LSTM network for predicting user wireless traffic. Recognizing the temporal correlation inherent in user data traffic, we utilize network traffic data from the preceding P time steps to forecast user traffic demand at the following time step $t+1$.

The LSTM unit, with its ability to capture long-term dependencies in time series data, is crucial to our approach. This capability stems from its intricately designed structure, rendering it an ideal choice for various sequence-related tasks. Our LSTM network comprises multiple layers, each comprising P LSTM units.

For each time step, the online LSTM receives current network traffic from users through uplink transmission. A softmax layer, connected following the LSTM layer, outputs the prediction results, facilitating the forecast for time slot $t+1$.

The proposed LSTM network employs backpropagation for parameter updates. Using Mean Absolute Error (MAE) as the loss function, the update process within the LSTM network can be represented as:

$$\boldsymbol{L}(\theta)=\frac{1}{K}\sum_{k=1}^{K}\left|y_k^{t+1}(\theta)-\hat{y}_k^{t+1}\right| \tag{3.9}$$

where θ represents all parameters in the LSTM network, $\hat{y}_k^{t+1}$ denotes the ground truth, and y_k^{t+1} signifies the prediction for user k at time slot $t+1$.

3.3.2 DDPG Algorithm

Since the problem in Equation 5.6 is a nonconvex optimization problem, we employ DDPG to find the optimal configuration for HRIS. DDPG can learn the optimal policy π by interacting with the environment to maximize the long-term QoE of users.

We model the BS and the HRIS as an agent and use a three-tuple $\langle \boldsymbol{S},\boldsymbol{A},\boldsymbol{R}\rangle$ to represent the fundamental elements in DDPG, which are specifically defined as follows:

- **State $\boldsymbol{S}_t$:** The state S_t consists of three parts: $\boldsymbol{Y}_t, \boldsymbol{C}_t, \mathrm{QoE}_{t-1}$. Thus, the state of the t-th time slot can be defined as
$$\boldsymbol{S}_t = [\boldsymbol{Y}_t, \boldsymbol{C}_t, \mathrm{QoE}_{t-1}] \tag{3.10}$$
where $\boldsymbol{Y}_t = [y_1^t, y_2^t, \cdots, y_k^t]$ is the predicted network traffic at the t-th time slot, $\boldsymbol{C}_t = [h_{r,k}^t, G^t, h_k^t]$ is the specific CSI in the t-th time slot, and QoE_{t-1} is the QoE of all users in the t-th time slot.

- **Action $\boldsymbol{A}_t$:** The action at the t-th time slot consists of two parts: $\boldsymbol{W}$ and $\boldsymbol{\Theta}$, which can be expressed as
$$\boldsymbol{A}_t = (\boldsymbol{W}, \boldsymbol{\Theta}) \tag{3.11}$$
where $\boldsymbol{W} = [w_1, w_2, \cdots, w_k]$ is the transmit precoding matrix, and $\boldsymbol{\Theta}$ is the configuration of the HRIS.

- **Reward $\boldsymbol{R}_t$:** The reward at the t-th time slot is defined as the QoE of all users, which is expressed as
$$\boldsymbol{R}_t = \sum_{k=1}^{K} \mathrm{QoE}_k(t) \tag{3.12}$$

The DDPG algorithm, structured on an actor-critic architecture, is outlined in Algorithm 1, which comprises the following steps:

1) Initialization: Before beginning to train the neural network, we initialize the critic and actor-network parameters, and the action $\boldsymbol{A}_t = (\boldsymbol{W}, \boldsymbol{\Theta})$. We also initialize the experience replay memory $\boldsymbol{M}$.

2) Training: At the commencement of training, the agent receives the current state S_t as input and selects an action S_t based on the policy π, which can be represented as

$$A_t = \pi\left(\theta_a \mid S_t\right) \tag{3.13}$$

where θ signifies the parameter of the actor-network.

Post the execution of action A_t, the environment provides a new observation and instant reward R_{t+1}. The transition composed of (s_t, a_t, r_t, s_{t+1}) is collected and stored in the experience pool $\boldsymbol{M}$. The Q value function signifies the return for adhering to a deterministic policy π, denoted as
$$\begin{aligned} Q_\pi\left(s_t, a_t\right) &= \mathbb{E}\left[R^t \mid s_t, a_t\right] \\ R^t &= \sum_{\varepsilon=0}^{\infty} \gamma^{\varepsilon} r^{t+1+\varepsilon} \end{aligned} \tag{3.14}$$
where $\gamma \in (0,1]$ is a discounting factor.

Algorithm 4 DDPG Algorithm

Input: $\boldsymbol{Y}_t, \boldsymbol{C}_t, \mathrm{QoE}_{t-1}$
Output: Action $\boldsymbol{A}_t = (\boldsymbol{W}, \boldsymbol{\Theta})$, QoE QoE_t
Initialization: Replay buffer $\boldsymbol{M}$, actor network parameters θ_a, target actor network parameters θ_a', critic network parameters θ_c, target critic network parameters θ_c', transmit precoding matrix $\boldsymbol{W}_t$, phase shift matrix $\boldsymbol{\Theta}_t$
Set initial state s_0
while $t < T+1$ **do**
    for $i = 1$ to N **do**
        Select action a_t based on current policy using Eq. (5.13)
        Apply action a_t, receive next state s_{t+1} and reward r_t
        Store transition (s_t, a_t, r_t, s_{t+1}) in $\boldsymbol{M}$
        Compute target Q-value using Eq. (5.14)
        Sample a mini-batch W from $\boldsymbol{M}$
        Construct the loss function $L(\theta_c)$ using Eq. (5.16)
        Update critic network parameters θ_c using Eq. (5.15)
        Update actor network parameters θ_a using Eq. (5.17)
        Update target networks θ_a' and θ_c' using Eq. (5.18)
        Set s_{t+1} as the input of the DDPG agent
    end for
end while

3) Update: The agent extracts a random mini-batch of experiences W from the experience replay buffer $\boldsymbol{M}$. Utilizing collected experiences W, we update the parameters of the critic networks in the direction of $\Delta_{\theta_c} L(\theta_c)$ by minimizing the loss $L(\theta_c)$, which can be expressed as

$$\theta_c^{t+1} = \theta_c^t - \mu_c \Delta_{\theta_c} L(\theta_c) \tag{3.15}$$

$$\begin{aligned} L(\theta_c) = \big(& R_t + \gamma Q_\pi\left(\theta_c' \mid s_{t+1}, \pi\left(\theta_a' \mid s_{t+1}\right)\right) \\ & - Q_\pi\left(\theta_c \mid s_t, a_t\right)\big)^2 \end{aligned} \tag{3.16}$$

where θ_c is the parameter of the target network, μ_c represents the rate of updating the critic network parameters, and $\pi(\theta_a' \mid s_{t+1})$ denotes the target actor-network with input s_{t+1}.

The agent updates θ_a in the direction of $\Delta_a Q_\pi(\theta_c \mid s_t, a_t)$, expressed as

$$\theta_a^{t+1} = \theta_a^t - \mu_a \Delta_a Q_\pi(\theta_c \mid s_t, a_t) \Delta_{\theta_a} \pi(\theta_a \mid s_t) \tag{3.17}$$

where μ_a represents the rate of updating the actor network parameters and $\Delta_a Q_\pi(\theta_c \mid s_t, a_t)$ is the gradient of the actor network. The actor-network aims to identify an optimal action a for maximizing the long-term QoE.

The DDPG network implements a soft update method to ensure the parameters of DDPG are updated in each iteration. The formula is as follows:

$$\begin{aligned} \theta_c' &\leftarrow \tau\theta_c + (1-\tau)\,\theta_c' \\ \theta_a' &\leftarrow \tau\theta_a + (1-\tau)\,\theta_a' \end{aligned} \tag{3.18}$$

where τ controls the rate of updating the target network parameters, θ_c' and θ_a' are parameters of the target network.

3.4 simulation results

In this section, we undertake an extensive series of experiments in a simulated environment to authenticate the efficacy of the proposed L-DRL algorithm, as illustrated in Fig. 5.2. We configure the LSTM with a time step of 20, a hidden layer of 5, and a learning rate of 0.0001. Within the DDPG, we assign a learning rate of 0.001, a mini-batch size of 24 for experience replay, and a buffer size 1000000. We generate the LoS channel $\boldsymbol{h}_{r,k}$ using a Rayleigh distribution and obtain $\boldsymbol{h}_k$ and $\boldsymbol{G}$ for HRIS.

3.4.1 Network Traffic Prediction

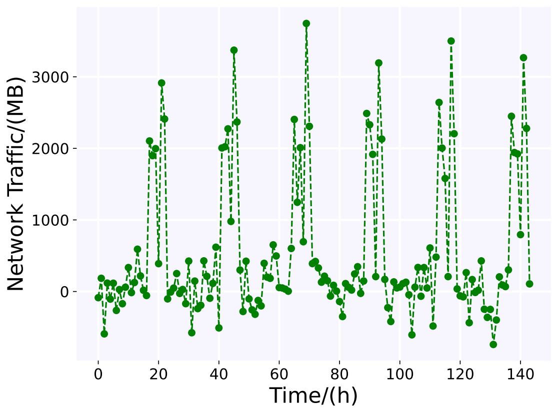

(a) The users' network traffic in 24h.

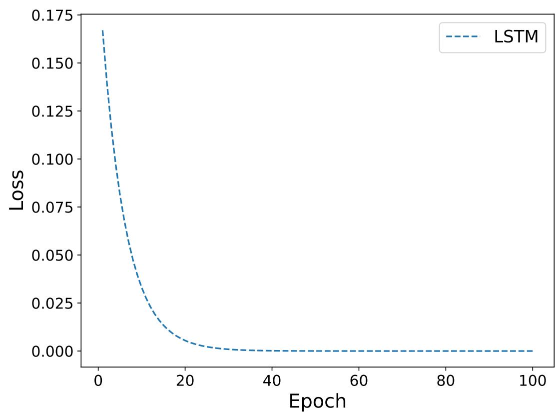

(b) Loss of the online LSTM for network traffic prediction.

Fig. 3.3 (a) The users' network traffic in 24h. (b) Loss of the online LSTM for network traffic prediction.

We collect data from 100 unique users over a week in 1-hour intervals to construct a real-world user network traffic dataset. As depicted in Fig. 3.3a, we present a five-day

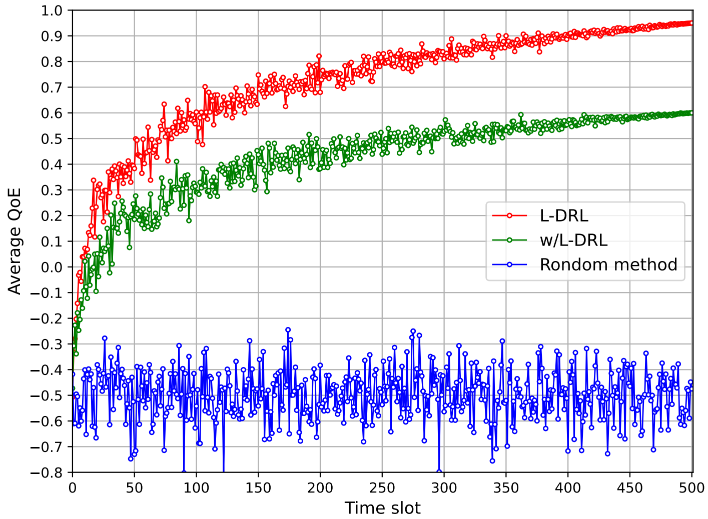

Fig. 3.4 Average QoE of the HRIS-assisted communication network.

user network traffic pattern. From Fig. 3.3a, it is clear that network traffic varies widely. Moreover, peak user traffic appears to coincide with specific times of the day, indicating a recurring pattern in the dynamics of network traffic. Given these patterns, it is plausible to forecast future user traffic.

Fig. 3.3b displays the loss for network traffic prediction, which stabilizes after 30 epochs, demonstrating the superior predictive capabilities of LSTM. By accurately predicting user traffic trends, we can pre-determine the beamforming direction, enhancing the configuration of HRIS elements.

3.4.2 Average QoE of Users

In the HRIS-assisted communication network, the average QoE signifies transmission quality. To validate the impact of the network traffic prediction module, we design a variant of L-DRL, designated as "w/L-DRL," which lacks a prediction module. As illustrated in Fig. 5.4, it is evident that our proposed L-DRL method outperforms the others.

Compared to random HRIS phase configurations, L-DRL ensures superior QoE by continuously optimizing the configuration through interaction with the environment. Furthermore, L-DRL outperforms w/L-DRL, confirming that accurate network traffic prediction can enhance the transmission quality of communication systems. Based on these findings, it is reasonable to conclude that the proposed L-DRL method can enhance communication quality and guarantee user QoE.

3.4.3 Average Transmission Rate Comparisons

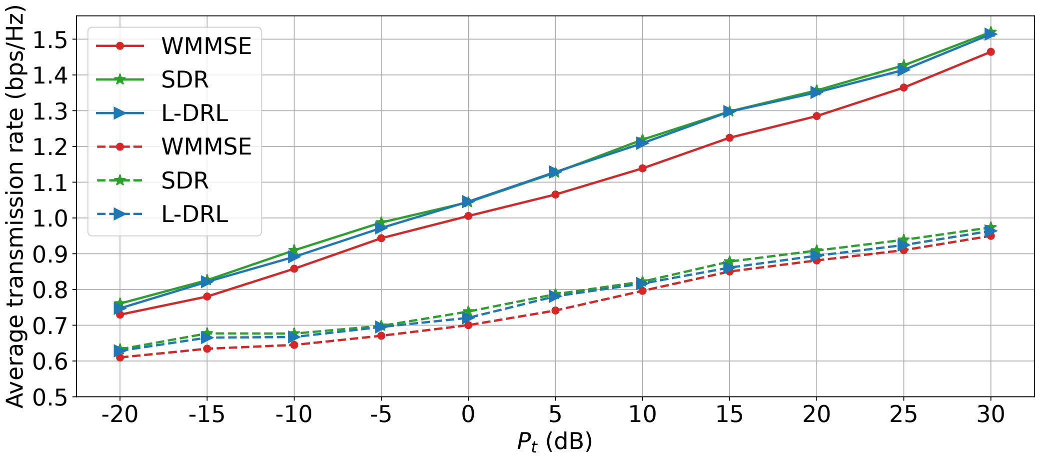

Fig. 3.5 Average transmission rate of L-DRL algorithm and the benchmarks.

To thoroughly investigate the performance of L-DRL, we compare it with two state-of-the-art methods, Semi-Definite Relaxation (SDR) and Weighted Minimum Mean Square Error (MMSE). We utilize the average transmission rate for users as the evaluation metric, providing an intuitive comparison of algorithm performance.

As shown in Fig. 5.5, the performance of our proposed L-DRL aligns with the two benchmarks. Hence, it is reasonable to conclude that our proposed algorithm effectively improves the transmission quality. We further examine the performance of the proposed algorithm and two benchmarks with increasing transmission power P_t under two system settings, $M = 8, N = 32, K = 8$ and $M = 32, N = 32, K = 32$. An increase in the number of users leads to a decrease in the average transmission rate due to channel interference. This indirectly suggests that reducing the number of optimized users of HRIS helps guarantee QoE for users with high transmission rate requirements.

3.4.4 Impact of system settings

To delve deeper into the performance of the proposed L-DRL, we examine the impact of the learning rate on this algorithm. An optimal learning rate aids the proposed algorithm in identifying the most suitable joint design of BS and HRIS. As depicted in Fig. 5.6, the proposed algorithm garners the highest average reward when the learning rate is 0.001. Proper hyperparameters enable the algorithm to interact more effectively with the environment and to update parameters more efficiently.

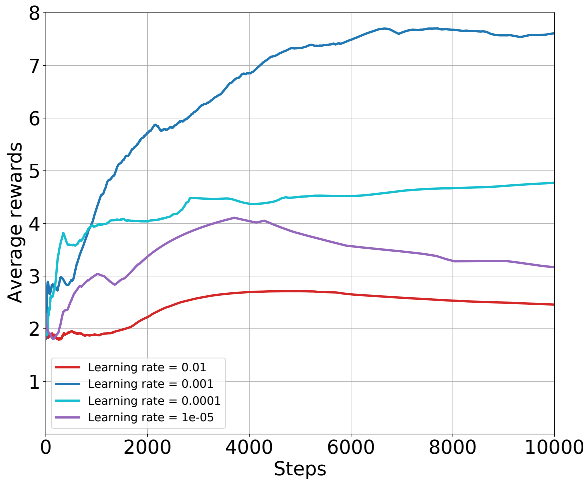

Fig. 3.6 Rewards at different learning rates.

Lastly, we delve into the influence of other hyperparameters, such as episode length, on the performance of L-DRL. Our analysis reveals that meticulous tuning of these hyperparameters can enhance the L-DRL's performance. Following parameter adjustments, the L-DRL model can adeptly manage the phase of elements in HRIS, guaranteeing a high-quality user experience.

3.5 Conclusion

This paper introduced a novel optimization algorithm, predicated on network traffic prediction, for HRIS configuration. To enhance user QoE, we initially employed an online LSTM network to predict future user network traffic, thereby assisting the communication system in executing superior beamforming. Subsequently, we utilized a DDPG algorithm to select the optimal HRIS configuration to maximize users' long-term QoE. Comprehensive simulation results demonstrated that the proposed L-DRL enhanced the average user transmission rate. Concurrently, the experimental results confirmed that appropriate parameter selection could facilitate improved system performance.

Chapter 4

QoE Optimization for Mobile Users Based on User Movements In VR Scenario

4.1 Motivation

Wireless virtual reality (VR) has emerged as a pivotal technology, revolutionizing how we interact with the digital world through immersive experiences that surpass traditional boundaries and impacting industries such as entertainment, gaming, healthcare, and education [83, 91]. Due to the wide range of potential applications, VR is considered as one of the most promising technologies in the consumer electronics field [65].

To fully realize VR's potential, three critical challenges must be addressed: ensuring high transmission rates for quality streaming, achieving low latency for real-time interaction, and maintaining stable connectivity in dynamic environments [15]. Existing wireless communication technologies, such as 5G and Wi-Fi 6, while offering a peak rate of Gbps, still need to be improved to meet the demanding requirements of VR [66].

Due to its capacity to provide high transmission speeds and low latency, the mmWave network is one of the most promising technologies for wireless VR [50]. However, integrating mmWave technology into VR systems presents several unique challenges [1]. Firstly, the high frequency of mmWave signals results in significant attenuation and path loss, requiring a direct line-of-sight (LoS) channel for communication between transmitter and receiver [43, 58]. Then, the directional nature of mmWave signals demands precise beam alignment to ensure high-performance communication [29]. In wireless VR, user mobility and obstacles like walls and furniture complicate maintaining stable LoS and accurate beam alignment [24].

To overcome the challenges in mmWave VR systems, several solutions like enhanced beamforming [70], rapid path search and alignment [51], and prediction of mobility trajectories [88] have been investigated. Notably, reconfigurable intelligent surface (RIS) emerges as an up-and-coming solution due to its energy efficiency, cost-effectiveness, and ease of integration [68]. RIS, a meta-surface with numerous passive, programmable elements, can dynamically control electromagnetic waves, enhancing signal propagation [22, 35]. It provides a solution for when direct LoS channels between transmitter and receiver are obstructed by creating an indirect path that ensures uninterrupted signal transmission despite obstacles [64, 44].

RIS technology is expected to play a vital role not only in enhancing communication but also in enabling precise localization within mmWave VR systems [93]. Accurate user positioning is essential for the beam alignment of the highly directional mmWave beams. However, the challenge of effectively achieving user localization and beam alignment in environments assisted by multiple RISs to improve VR user experience and reduce interactive latency is still a critical unresolved issue.

This paper introduces a novel framework in multi-RIS-assisted mmWave VR systems to solve the above challenges. As shown in Fig. 4.1, the algorithm initiates as the VR device detects user movement through embedded inertial measurement units (IMUs). Upon detecting movement, the VR user signals its change of location to the access point (AP) via the uplink channel. The AP then sends a probing signal for the VR device to estimate its current position through a localization procedure. After estimating its position, the user equipment (UE) relays this information to the AP, laying the groundwork for location-based beamforming. With accurate VR user location information, we can jointly optimize the AP, VR users, and RISs beamforming directions, thereby enhancing data transmission rates and VR user QoE. The proposed localization-based beamforming algorithm can dynamically adjust beam direction in response to VR user movements, ensuring seamless, high-speed communication within the RIS coverage area. The main contributions of our paper are summarized as follows:

- We investigate the optimization of QoE for multiple moving VR users in multi-RIS-assisted scenarios, where RIS plays a crucial role in both localization and communication. The proposed framework considers several key performances, including transmission rate, latency, and QoE.

- We developed an AoD-based positioning algorithm that leverages reflective paths from multiple RIS, significantly improving localization accuracy. Specifically, a maximum

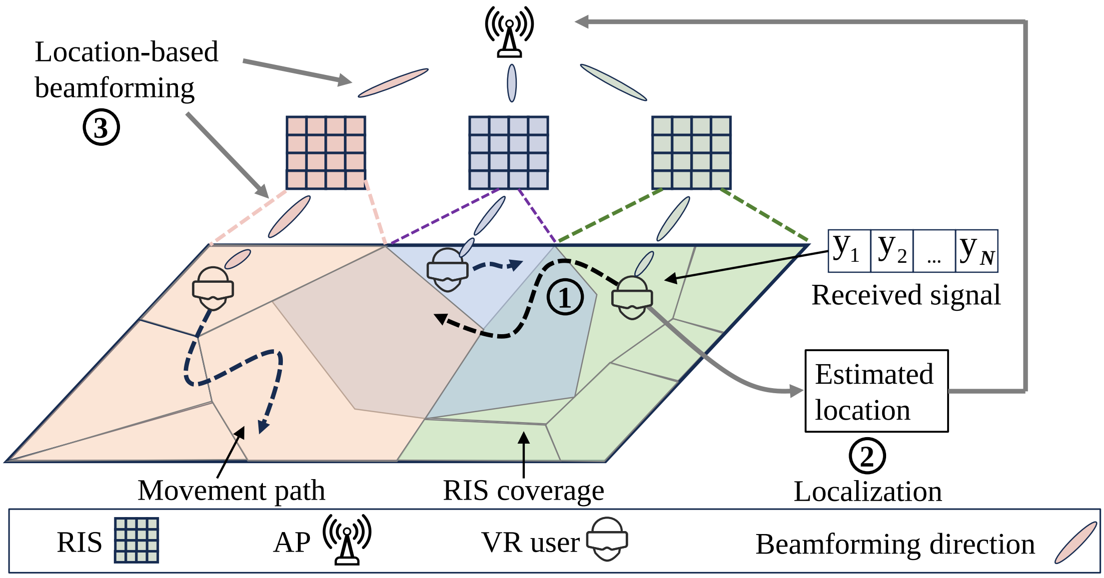

Fig. 4.1 An overview of our proposed framework in a multi-RIS-assisted mmWave VR network, where the LoS link from AP to VR users is blocked. The AP sends a probing signal when the VR user's location changes. Then, the UE estimates its position based on the received signal and uploads the estimated location to the AP. Finally, the location-based beamforming is conducted based on the estimated location.

likelihood (ML) estimation method is first applied to estimate the AoDs of each RIS to VR users. Then, an AoD-based localization algorithm is proposed to obtain the estimated location for each VR user.

- A location-based beamforming method is proposed to optimize the QoE of VR users, utilizing VR users' locations to select optimal beamforming directions. Compared to the benchmark algorithm, our proposed method can guarantee users' QoE with reduced computational requirements.
- Comprehensive simulations validate the feasibility and effectiveness of our multi-RIS-assisted VR mmWave network, demonstrating our method's ability to improve QoE and reduce latency. Furthermore, we analyze the impact of critical parameters on QoE and interaction latency, including the number of RIS, reflecting elements, and total transmission power.

4.2 Related Work

This section provides an overview of the current literature on mmWave VR systems, RIS deployment in integrated sensing and communication (ISAC) systems, and RIS-assisted VR systems.

1) Wireless VR in the mmWave Frequency Band: mmWave is widely recognized as the optimal communication frequency band for achieving rapid and seamless wireless transmission, with aspects like transmission rate, reliability, delay, quality of service, energy efficiency, and resource consumption receiving substantial investigation [72, 70, 88, 10, 12].

In [70], the proposed CoVRage solution focuses on the receiving side for VR headset users, using built-in sensor orientation data to predict user movement and adjust the phased array accordingly, ensuring high, stable gain. In [88], research on coordinated multipoint transmission (CoMP) with mmWave communication has shown improvements in VR system dependability and power efficiency, utilizing parallel echo state networks (ESN) for movement prediction and deep reinforcement learning (DRL) for power control optimization. The authors of [72] introduce a resource control mechanism for IoT-based consumer electronics, enhancing network efficiency and energy sustainability using RIS. In [10], a dual-link design combining sub-6 GHz and mmWave networks has been proposed to enhance wireless VR transmission consistency. In [12], an innovative transmission scheme has been introduced to balance quality of service (QoS) with minimal resource consumption for wireless VR. However, these studies mainly focus on scenarios with direct LoS links, not fully exploring RISs' potential to provide high communication performance when LoS is obstructed.

2) RIS in ISAC systems: The integration of RIS into ISAC systems has been extensively studied for its potential to enhance detection and communication. Notably, research has shown RIS's capability to improve the Cramér-Rao lower bound for signal detection [78], as well as its role in augmenting the signal-to-noise ratio (SNR) through the combination of active and passive beamforming strategies [31]. In [38], a memorization method has been applied to simplify the RIS beamforming algorithm, optimizing RIS parameter matrices. Furthermore, simultaneously transmitting and reflecting surfaces (STARS) have been proposed to boost ISAC system performance, demonstrating enhanced sensing accuracy and reliability over traditional RIS [79]. RIS has also significantly elevated the communication and sensing performance of mmWave orthogonal frequency division multiplexing (OFDM) ISAC systems [76]. Despite these advancements, exploring RIS within VR environments, particularly in enhancing VR system sensing and transmission, still needs to be explored.

3) RIS-assisted VR system: As detailed in [45], researchers have explored the integration of RIS in ISAC systems to enhance channel throughput by simultaneously fine-tuning UE beamformers and adjusting RIS phases. In [9], an innovative framework to improve transmission speed and reliability was proposed, employing risk considerations. This involved transforming the optimization challenge into a linear weighted equation using Lyapunov optimization techniques, followed by applying a recurrent neural network (RNN) with reinforcement learning to solve this equation. However, while focusing on transmission rate optimization, these studies have not fully leveraged RIS's capabilities in ISAC environments.

The reviewed literature highlights the potential and challenges of utilizing mmWave and RIS technologies in VR systems. Building on these insights, our research aims to overcome current limitations by proposing a framework that utilizes multiple RISs to improve mmWave VR environments, especially on NLoS and dynamic scenarios.

4.3 System Model

In the considered indoor scenario depicted in Fig. 4.1, we consider an AP serving $\boldsymbol{U}$ VR users, with the assistance of $\boldsymbol{K}$ RISs. The indices of RISs and VR users are given by $\boldsymbol{K} = [1,2,\ldots,K]$ and $\boldsymbol{U} = [1,2,\ldots,U]$, respectively. The AP, equipped with a uniform linear array (ULA) of N_p antennas, is strategically positioned within the indoor space $\boldsymbol{S}$, at a location specified by the position vector $\boldsymbol{q}_p \in \mathbb{R}^3$. Each RIS, configured as a uniform planar array (UPA) with $N_k = N_{k,x} \times N_{k,y}$ elements, occupies a distinct position $\boldsymbol{q}_k \in \mathbb{R}^3$. These RISs play a pivotal role in the data transmission and localization of VR users, which are modeled as a ULA with N_u antennas and located at $\boldsymbol{q}_u \in \mathbb{R}^3$. The system operates at a carrier frequency f_o, corresponding to a wavelength $\lambda = c/f_o$, where c denotes the speed of light. The spacing between the elements and arrays is set to $\lambda/2$. Due to the significant path loss of mmWave signals, this study focuses on signals reflected once by the RIS, excluding scenarios involving multiple reflections.

4.3.1 RIS Model

Without loss of generality, we assume that the RIS is located within the far-field region of the AP and UE. Therefore, we can represent the local reflection coefficient for each element in RIS as $\sqrt{F(\boldsymbol{\theta})F(\boldsymbol{\phi})}G_k\Gamma_k$. Herein, $\boldsymbol{\theta} = (\theta_{\text{az}}, \theta_{\text{el}})$ denotes the angle-of-arrive (AoA) in RIS local coordinate, where θ_{az} and θ_{el} indicates azimuth and the elevation angle, $\boldsymbol{\phi} = (\phi_{\text{az}}, \phi_{\text{el}})$ denotes the angle-of-departure (AoD) in RIS local coordinate, $F(\boldsymbol{\theta})$ denotes the standardized radiation pattern for every element, which can be expressed as:

$$F(\boldsymbol{\theta}) = \begin{cases} \cos^q \theta_{\text{el}} & \theta_{\text{el}} \in \left[0, \frac{\pi}{2}\right], \theta_{\text{az}} \in [0, 2\pi] \\ 0 & \theta_{\text{el}} \in \left[\frac{\pi}{2}, \pi\right], \theta_{\text{az}} \in [0, 2\pi] \end{cases} \tag{4.1}$$

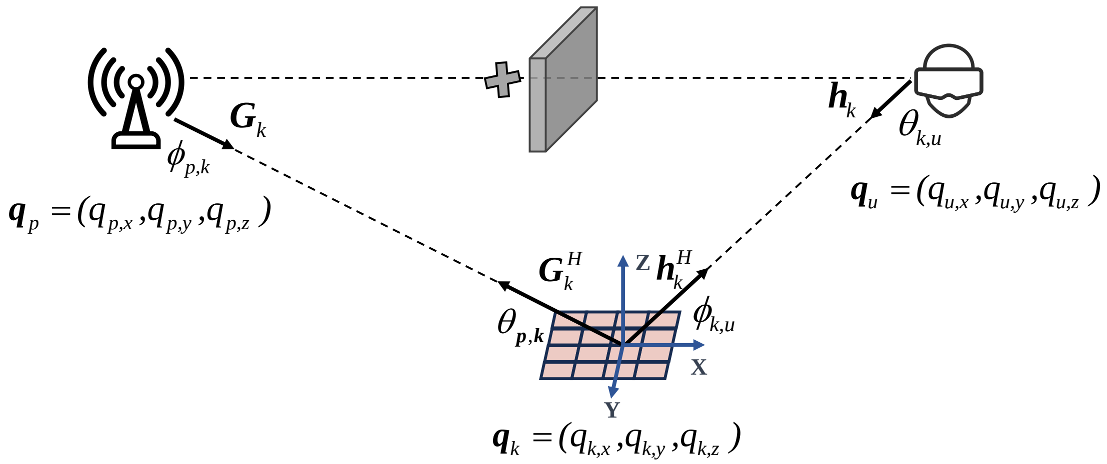

Fig. 4.2 Illustration of the channel model depicting the spatial relationship between the AP, RIS, and the VR user.

where q is a tunable parameter. Furthermore, G_k is the element's boresight gain, and $\Gamma_k = \alpha_k e^{jv_k}$ represents the load reflection coefficient for each element. Here, α_k and v_k represent the amplitude and phase of the elements within the RIS. In our analysis of RIS configuration optimization, we concentrate on the amplitude and phase adjustments for each RIS element. We simplify our discussion by fixing the amplitude α_k at 1. The focus then shifts to the phase shifts v_k, which are set to discrete values following a bit-quantization method. Specifically, the phase shifts v_k are selected from a predefined set $\boldsymbol{V}_b = \left\{0, \frac{2\pi}{2^b}, \ldots, \frac{2\pi}{2^b}\left(2^b - 1\right)\right\}$. Here, b represents the bit-quantization level, and $N = 2^b$ is the number of discrete phase states. This quantization approach is chosen for its practicality and computational efficiency, streamlining the implementation of the RIS configuration.

4.3.2 Channel Model

We establish the channel model after detailing the RIS model and its reflection characteristics. As illustrated in Fig. 4.2, the direct channel from AP to VR users is blocked, requiring RIS to create the indirect channel between AP and VR users. The array response vector from the AP towards a specific location $\boldsymbol{q}$ is defined as follows:

$$\mathbf{a}_{AP}(\boldsymbol{q}) = \sum_{n=1}^{N_p} e^{j\left\langle \boldsymbol{k}_{pq}, (\boldsymbol{q}_p^n - \boldsymbol{q}_p)\right\rangle} \tag{4.2}$$

where $\mathbf{a}_{AP}(\boldsymbol{q}) \in \mathbb{C}^{N_p \times 1}$ represents the AP's array response vector, $\boldsymbol{q}_p^n$ indicates the position of n-th antenna at the AP, and $\boldsymbol{k}_{pq}$ is the wave vector pointing towards $\boldsymbol{q}$, given by:

$$\boldsymbol{k}_{pq} = \frac{2\pi}{\lambda} \frac{\boldsymbol{q}_p - \boldsymbol{q}}{\|\boldsymbol{q}_p - \boldsymbol{q}\|} \tag{4.3}$$

Likewise, the array response vector of k-th RIS towards point $\boldsymbol{q}$ is formulated as:

$$\mathbf{a}_R^k(\boldsymbol{q}) = \sum_{m=1}^{N_k} e^{j\langle \boldsymbol{k}_{kq}, (\boldsymbol{q}_k^m - \boldsymbol{q}_k)\rangle} \tag{4.4}$$

Here, $\mathbf{a}_R^k(\boldsymbol{q}) \in \mathbb{C}^{N_k \times 1}$ represents the array response vector of the k-th RIS, $\boldsymbol{q}_k^m$ denotes the position of m-th element on the k-th RIS, and the wave vector $\boldsymbol{k}_{kq}$ is defined as:

$$\boldsymbol{k}_{kq} = \frac{2\pi}{\lambda} \frac{\boldsymbol{q}_k - \boldsymbol{q}}{\|\boldsymbol{q}_k - \boldsymbol{q}\|} \tag{4.5}$$

The overall channel gain from AP to k-th RIS is expressed as:

$$\begin{aligned} \alpha_{p,k} = &\sqrt{F(\boldsymbol{\theta}_{p,k}) G_k G_p} \\ &\frac{\lambda}{4\pi \|\boldsymbol{q}_{p,k}\|} \exp\left(\frac{-j2\pi \ \|\boldsymbol{q}_{p,k}\|}{\lambda} \right) \end{aligned} \tag{4.6}$$

Here, G_p and G_k denote the boresight gain of AP and RIS antennas, respectively. $\boldsymbol{q}_{p,k} = \boldsymbol{q}_p - \boldsymbol{q}_k$ is the vector from AP to k-th RIS, the corresponding angle $\boldsymbol{\theta}_{p,k} = [\theta_{p,k}^{el}, \theta_{p,k}^{az}]$ is the AoA from AP to k-th RIS, where $\theta_{p,k}^{az} = \arccos(\boldsymbol{q}_{p,k}[3] / \|\boldsymbol{q}_{p,k}\|)$ and $\theta_{p,k}^{el} = \arctan 2(\boldsymbol{q}_{p,k}[2], \boldsymbol{q}_{p,k}[1])$.

Thus, the channel from AP to k-th RIS can be written as:

$$\boldsymbol{G}_k = \alpha_{p,k} \mathbf{a}_R^k(\boldsymbol{q}_p) \mathbf{a}_{AP}^H(\boldsymbol{q}_k) \tag{4.7}$$

Likewise, the channel from the k-th RIS to VR user $\boldsymbol{q}_u$ can be represented as:

$$\boldsymbol{h}_{k,u} = \alpha_{k,u} \mathbf{a}_R^k(\boldsymbol{q}_u) \mathbf{a}_u^H(\boldsymbol{q}_k) \tag{4.8}$$

Where $\boldsymbol{h}_k \in \mathbb{C}^{N_k \times N_u}$, $\mathbf{a}_u^H(\boldsymbol{q}_k)$ denotes the array response vector of VR users, and the overall channel gain $\alpha_{k,u}$ can be denoted as:

$$\alpha_{k,u} = \sqrt{F(\boldsymbol{\phi}_{k,u}) G_k G_u} \\ \frac{\lambda}{4\pi \left\|\boldsymbol{q}_{k,u}\right\|} \exp\left(\frac{-j2\pi \left\|\boldsymbol{q}_{k,u}\right\|}{\lambda}\right) \tag{4.9}$$

where G_u is the boresight gain of antennas of VR users, $\boldsymbol{\phi}_{k,u}$ and $\boldsymbol{q}_{k,u} = \boldsymbol{q}_k - \boldsymbol{q}_u$ represent the AoD and vector from k-th RIS to u-th VR user.

Therefore, the received signal of u-th VR user can be expressed as:

$$y_u = \sum_{k=1}^{K} \boldsymbol{m}_u \boldsymbol{h}_{k,u}^H \boldsymbol{\Phi}_k \boldsymbol{G}_k \boldsymbol{W} \boldsymbol{s} + \eta_u \tag{4.10}$$

where $\boldsymbol{m}_u = [\frac{1}{\sqrt{N_u}}(e^{j\pi\theta_1}, \ldots, e^{j\pi\theta_{N_n}})] \in \mathbb{C}^{1 \times N_u}$ represents the beamforming matrix of u-th VR user, $\boldsymbol{\Phi}_k = \mathrm{diag}[e^{jv_1}, \ldots, e^{jv_{N_k}}] \in \mathbb{C}^{N_k \times N_k}$ denotes the phase shift of k-th RIS, $\boldsymbol{W} \in \mathbb{C}^{N_p \times N_u}$ denotes the transmit precoding matrix for AP where each column $\boldsymbol{w}_u$ corresponds to the precoding vector for u-th VR users, $\boldsymbol{s} = [s_1, s_2, \ldots, s_U] \in \mathbb{C}^{N_u \times 1}$ is the transmit data where $\mathbb{E}\left[|s_k|^2\right] = 1 \quad \forall k$, and $\eta_u \sim \boldsymbol{CN}(0, \sigma_u^2)$ is the gaussian white noise of u-th VR users.

Thus, the signal-to-interference-plus-noise (SINR) of u-th VR user can expressed as:

$$\mathrm{SINR}_u = \frac{\left|\sum_{k=1}^{K} \boldsymbol{m}_u \boldsymbol{h}_{k,u}^H \boldsymbol{\Phi}_k \boldsymbol{G}_k \boldsymbol{w}_u\right|^2}{\sigma^2 + \sum_{j \neq u} \left|\sum_{k=1}^{K} \boldsymbol{m}_u \boldsymbol{h}_{k,u}^H \boldsymbol{\Phi}_k \boldsymbol{G}_k \boldsymbol{w}_j\right|^2} \tag{4.11}$$

where σ^2 represents the noise of the system. Furthermore, the achievable rate of u-th VR user can be defined as:

$$R_u = \log_2(1 + \mathrm{SINR}_u) \tag{4.12}$$

4.3.3 Codebook

To enhance the average achievement rate of the multi-RIS-assisted multi-user mmWave VR system, accurate CSI is crucial, according to Eq. (4.12). However, the passive nature of RIS and the dynamic environment pose challenges in acquiring precise, real-time CSI. Moreover, given the extensive number of elements, real-time optimization of RIS configurations can lead to delays, adversely impacting VR users' QoE. A codebook approach is utilized for QoE optimization to address latency issues.

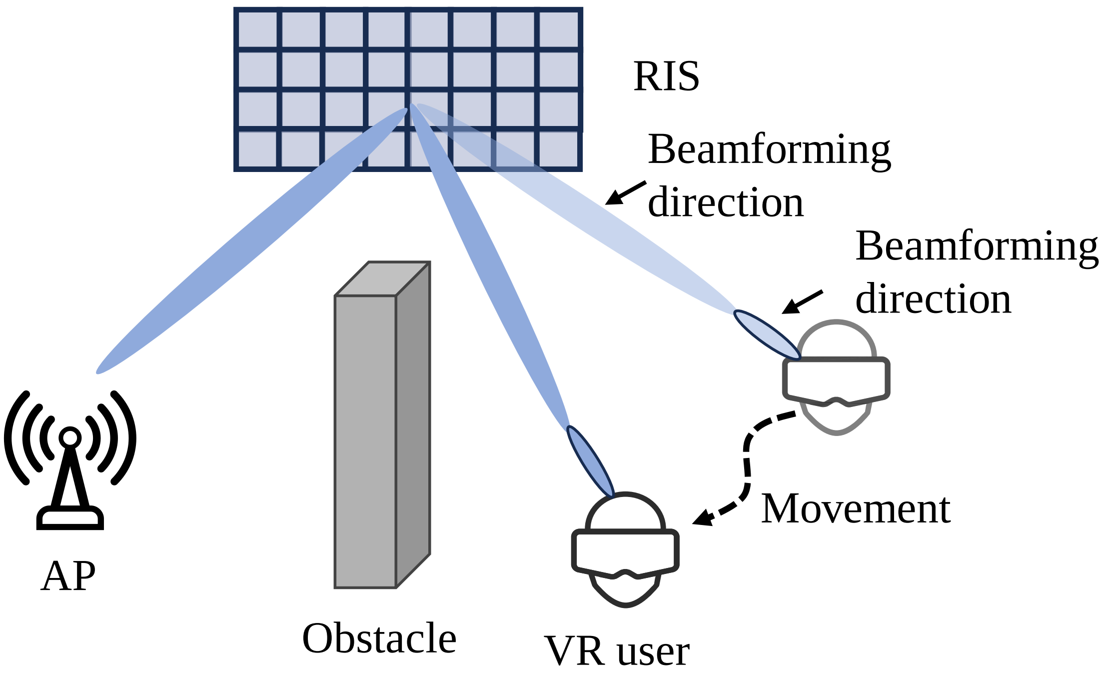

Fig. 4.3 The direction of beam alignment changes with the movement of the VR user.

A codebook comprises a set of predefined RIS element configurations in RIS-assisted systems. Each configuration (or codeword) corresponds to a specific phase shift pattern, directing or shaping the beam towards a desired direction [2, 75].

Considering a codebook $\boldsymbol{C} = \{\boldsymbol{c}_1, \boldsymbol{c}_2, \ldots, \boldsymbol{c}_L\}$, with each $\boldsymbol{c}_l \in \mathbb{C}^{N_k \times 1}$ representing a RIS configuration $\boldsymbol{\Phi}$. Specifically, the codewords are defined as $\boldsymbol{c}_l = \boldsymbol{c}_l^v \otimes \boldsymbol{c}_l^h$, where

$$\boldsymbol{c}_l^v = \frac{1}{\sqrt{N_{k,x}}} \left[1, e^{\frac{j2\pi v}{\varpi N_v}}, \ldots, e^{\frac{j2\pi(N_{k,x}-1)v}{\varpi N_v}} \right] \tag{4.13}$$

$$\boldsymbol{c}_l^h = \frac{1}{\sqrt{N_{k,y}}} \left[1, e^{\frac{j2\pi h}{\varpi N_h}}, \ldots, e^{\frac{j2\pi(N_{k,x}-1)h}{\varpi N_h}} \right] \tag{4.14}$$

$\boldsymbol{c}_l^v$ and $\boldsymbol{c}_l^h$ are the codewords for vertical and horizontal dimensions, respectively, N_v and N_h indicating the number of codewords, and ϖ adjusting based on the RIS's scan range.

Each codeword $\boldsymbol{c}_l$ represents a specific beam pattern. Selecting the optimal beam for each user ensures beam alignment, maximizing transmission rates.

4.3.4 The Mobility Model of VR Users

As illustrated in Fig. 4.3, the movement of the VR user disrupts the existing beam alignment between the RIS and VR users. We employ a virtual reality mobility model (VRMM) to simulate the movement path of VR users, which is mainly determined by the following four key variables: the initial position, movement velocity, the end position, and movement direction. At each discrete time interval, VR users can move in one of four directions: upward, downward, leftward, or rightward. Users determine their speed, endpoint, and travel direction starting from the initial location. It's essential to note that the VR user's location for the next time slot depends on their present location, not on previous positions, thus maintaining the Markovian nature of the mobility model. Upon reaching their destination, users select a new endpoint and continue at the same speed.

4.3.5 Problem Formulation

Several factors, including video frame resolution, delay in VR interactions, and connection stability, impact wireless VR users' QoE. According to [41], the QoE for the u-th VR user at the t-th time slot is given by:

$$\mathrm{QoE}_u(t) = \hat{\rho}_u(t)\left(q(R_u(t)) - |\Delta R_u(t)|\right) \tag{4.15}$$

where $q(R_u(t)) = R_u(t)/R_{\mathrm{th}}$ is the metrics for data transmission, R_{th} is the threshold of the transmission rate, $\Delta R_u(t) = q(R_u(t)) - q(R_u(t-1))$ is the changes in signal transmission quality for $t-1$ time slot to t time slot. Furthermore, $\hat{\rho}_u(t)$ represents the accuracy of beam alignment.

While maximizing transmission speed is crucial, reducing latency in user interactions to below a specific threshold is equally important for enhancing user QoE. VR latency is composed of three main components: uplink transmission latency, downlink transmission latency, and rendering latency, as shown below:

$$T_{\mathrm{VR}} = T_{\mathrm{up}} + T_{\mathrm{down}} + T_{\mathrm{render}} \tag{4.16}$$

The uplink transmission latency T_{up} is minimal due to the small size of data transmitted and thus can be considered negligible. Furthermore, as the size of the rendered data is the same at any given time, it is appropriate to consider the rendering time T_{render} as a constant. Therefore, our objective is to maximize the QoE of users within the constraints of the latency, which can be formulated as:

$$(\mathbf{P0}) \quad \max_{\boldsymbol{w},\boldsymbol{c}_l,\boldsymbol{m}} \quad \sum_{i=t}^{\infty}\sum_{u=1}^{U} \mathrm{QoE}_u(i) \tag{17}$$

$$\text{s.t.} \quad \mathrm{Tr}\left[\sum_{k=1}^{K}\left(\mathbf{g}_k^{+}\mathbf{P}\left(\mathbf{g}_k^{+}\right)^{H}\right)\right] \leq P_t \tag{4.17a}$$

$$\boldsymbol{c}_l \in \{\boldsymbol{c}_1, \boldsymbol{c}_2, \ldots, \boldsymbol{c}_L\}, \forall l \tag{4.17b}$$

$$T_{\mathrm{up}} + T_{\mathrm{down}} + T_{\mathrm{render}} \leq T_{\mathrm{th}} \tag{4.17c}$$

where $\mathbf{P}$ represents the power allocation for users, P_t is the transmission power for AP, $\mathbf{g}_k^{+} = \boldsymbol{h}_{k,u}^{H}\boldsymbol{\Phi}_k\boldsymbol{G}_k$, and T_{th} is the threshold of latency.

However, solving $(\mathbf{P0})$ directly is computationally challenging due to its complexity and the necessity for real-time processing. The solution requires high-dimensional optimization, which is computationally demanding and impractical for real-time scenarios. To address this, we propose a localization-based beam selection algorithm as a more efficient alternative. This method utilizes users' spatial information to simplify the optimization problem, significantly reducing computational requirements while ensuring precise beam alignment, thus improving system performance within latency limits.

4.4 Localization-based Beamforming

In this section, we detail our proposed localization-based beam selection algorithm. Initially, we outline the framework, followed by an in-depth explanation of our multi-user localization algorithm. Next, we present a location-based beam selection strategy to enhance user QoE.

4.4.1 Framework of the Localization-based Beamforming

To address the demands for low latency and high transmission rates in VR applications, we introduce a new transmission frame structure designed to enhance user experience. As depicted in Fig. 4.4, our proposed framework segments one location coherence interval, T_L, into three successive phases, ensuring a smooth and high-quality VR experience.

Stage I - Localization: This stage aims to determine the positions of VR users. Upon a user's location changes, the AP transmits a probing signal $\boldsymbol{s} = [s_1, s_2, \ldots, s_N] \in \mathbb{C}^{1\times N}$, where N is the length of the probing signal. Then, a distinct AoD is deduced from the received signal $\boldsymbol{y}$ for each RIS-assisted path. Estimations of user positions are then obtained by identifying the intersections of M ($M \geq 3$) lines, each representing an AoD.

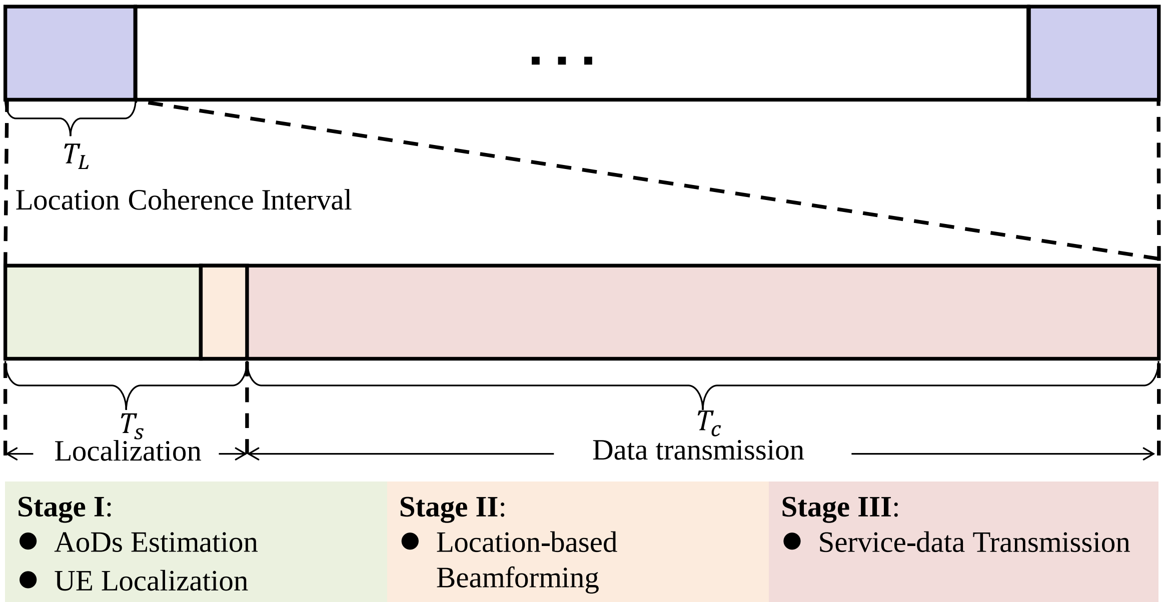

Fig. 4.4 Illustration of the framework for the proposed localization-based beamforming method.

Stage II - Location-based beam selection: After estimating user locations, the system begins the beam selection phase. Stage II involves identifying optimal reflection paths from the RIS for each user and adjusting the RIS to align its beams with their current locations, thus optimizing signal paths for enhanced reception quality.

Stage III - Service-data transmission: This final stage involves transmitting VR content to users via the downlink, using the beam configurations established in the previous stage. This stage continues until a user's position changes, prompting a return to Stages I and II.

It is important to note that during Stage I, the system design ensures simultaneous reception of probing signals from the AP by all users. Additionally, to eliminate interference among multiple RIS, only one RIS is operational at any given time, while the others are deactivated.

4.4.2 AoDs Estimation

In Stage I, the communication channel from AP to the u-th VR user through k-th RIS can be written as:

$$\boldsymbol{H}_{k,u} = \alpha_k \mathbf{a}_{AP}(\boldsymbol{q}_k)\mathbf{a}_R^k(\boldsymbol{q}_p)\boldsymbol{\Phi}_k \mathbf{a}_R^k(\boldsymbol{q}_u)\mathbf{a}_u^H(\boldsymbol{q}_k) \tag{4.18}$$

where $\alpha_k = \alpha_{p,k} \times \alpha_{k,u}$ denotes the path loss. With the positions of the AP and RISs predetermined, the received signal of u-th VR user via k-th RIS can be further written as:

$$\boldsymbol{y}_{k,u} = \alpha \mathbf{F} \mathbf{h}(\boldsymbol{\phi}_{k,u}, \boldsymbol{\theta}_{k,u}) \boldsymbol{s} + \boldsymbol{\eta}_{k,u} \tag{4.19}$$

where $\boldsymbol{y}_{k,u}$ denotes the received signal,α is the path gain, $\mathbf{F}$ denotes the precoding matrix of AP and UE, $\boldsymbol{\eta}_{k,u} \sim \boldsymbol{CN}(0, \sigma^2 \boldsymbol{I})$ is the gaussian white noise of u-th VR users, $\mathbf{h}(\boldsymbol{\phi}_{k,u}, \boldsymbol{\theta}_{k,u}) \triangleq vec(\mathbf{a}_R^k(\boldsymbol{\phi}_{k,u}) \mathbf{a}_u(\boldsymbol{\theta}_{k,u}))$, $\boldsymbol{\phi}_{k,u}$ and $\boldsymbol{\theta}_{k,u}$ denote the AoD of k-th RIS and AoA of u-th VR user, respectively, as shown in Fig. 5.4. A maximum likelihood (ML) estimation method is utilized for estimating the propagation parameters $(\alpha, \boldsymbol{\phi}_{k,u}, \boldsymbol{\theta}_{k,u})$, which is described as follows:

$$\left(\hat{\alpha}, \hat{\boldsymbol{\theta}}_{k,u}, \hat{\boldsymbol{\phi}}_{k,u}\right) = \underset{\alpha, \boldsymbol{\phi}_{k,u}, \boldsymbol{\theta}_{k,u}}{\arg\max} \boldsymbol{L}(\alpha, \boldsymbol{\phi}_{k,u}, \boldsymbol{\theta}_{k,u}) \tag{4.20}$$

where

$$\begin{aligned} \boldsymbol{L}(\alpha, \boldsymbol{\phi}_{k,u}, \boldsymbol{\theta}_{k,u}) &= \ln p\left(\boldsymbol{y}_{k,u} | (\alpha, \boldsymbol{\phi}_{k,u}, \boldsymbol{\theta}_{k,u})\right) \\ &= -N \log \pi \sigma^2 - \frac{\left\| \boldsymbol{y}_{k,u} - \alpha \mathbf{F} \boldsymbol{h}(\boldsymbol{\phi}_{k,u}, \boldsymbol{\theta}_{k,u}) \right\|^2}{\sigma^2} \end{aligned} \tag{4.21}$$

Therefore, when $\frac{\partial \boldsymbol{L}(\alpha, \boldsymbol{\phi}_{k,u}, \boldsymbol{\theta}_{k,u})}{\partial \alpha} = 0$, the optimal $\hat{\alpha}$ can be expressed as:

$$\hat{\alpha} = \frac{(\mathbf{F} \boldsymbol{h}(\boldsymbol{\phi}_{k,u}, \boldsymbol{\theta}_{k,u}))^H \boldsymbol{y}_{k,u}}{\|\mathbf{F} \boldsymbol{h}(\boldsymbol{\phi}_{k,u}, \boldsymbol{\theta}_{k,u})\|^2} \tag{4.22}$$

Then, we can obtain the new expression of $\boldsymbol{L}(\alpha, \boldsymbol{\phi}_{k,u}, \boldsymbol{\theta}_{k,u})$ by substituting Eq. (4.22) in Eq. (4.21), i.e.,

$$\begin{aligned} \boldsymbol{L}(\alpha, \boldsymbol{\phi}_{k,u}, \boldsymbol{\theta}_{k,u}) &= -N \log \pi \sigma^2 \\ &- \frac{\left\| \boldsymbol{y}_{k,u} - \frac{\mathbf{F} \boldsymbol{h}(\boldsymbol{\phi}_{k,u}, \boldsymbol{\theta}_{k,u}) \boldsymbol{h}^H(\boldsymbol{\phi}_{k,u}, \boldsymbol{\theta}_{k,u}) \mathbf{F}^H}{\|\mathbf{F} \boldsymbol{h}(\boldsymbol{\phi}_{k,u}, \boldsymbol{\theta}_{k,u})\|_2^2} \boldsymbol{y}_k \right\|_2^2}{\sigma^2} \end{aligned} \tag{4.23}$$

In Stage I, we mainly focus on AoD estimation. Therefore, we assume the user's beamforming matrix is random and provides uniform gain in all directions. To maximize the log-likelihood function, we can obtain the following optimization problem:

$$\begin{aligned} (\mathbf{P1}) \quad & \max_{\boldsymbol{\phi}_{k,u}} \left\| \frac{\boldsymbol{h}^H(\boldsymbol{\phi}_{k,u}) \mathbf{F}^H}{\|\mathbf{F} \boldsymbol{h}(\boldsymbol{\phi}_{k,u})\|_2} \boldsymbol{y}_{k,u} \right\|_2^2 \\ & \text{s.t.} \quad 0 \leq \boldsymbol{\phi}_{k,u}[1] < 2\pi \\ & \qquad\;\; 0 \leq \boldsymbol{\phi}_{k,u}[2] \leq \frac{\pi}{2} \end{aligned} \tag{4.24}$$

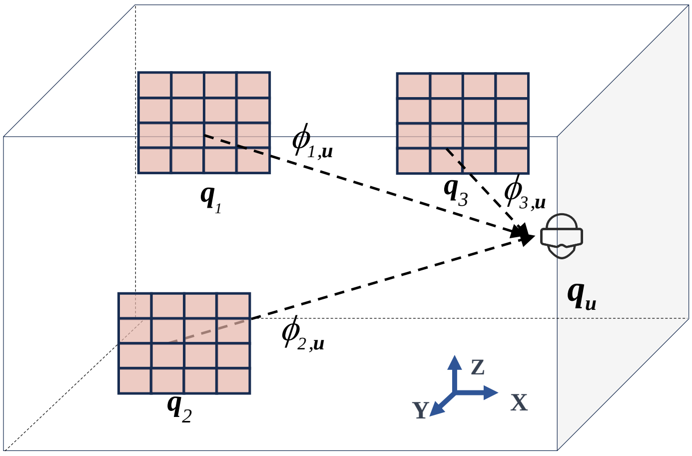

Fig. 4.5 The proposed AoDs-based localization approach, where $\boldsymbol{q}_1$, $\boldsymbol{q}_2$ and $\boldsymbol{q}_3$ represent the location of RISs which are known in advance.

Due to (**P1**) being a non-convex problem, we propose an AoD parameter estimation algorithm to solve this problem. Let $f(\boldsymbol{\phi}_{k,u}) = \left\| \frac{\boldsymbol{h}^H(\boldsymbol{\phi}_{k,u})\mathbf{F}^H}{\|\mathbf{F}\boldsymbol{h}(\boldsymbol{\phi}_{k,u})\|_2} \boldsymbol{y}_k \right\|_2^2$, the optimal AoD can be denoted as:

$$f(\boldsymbol{\phi}^*_{k,u}) = \max_{\boldsymbol{\phi}_{k,u} \in \boldsymbol{G}} f(\boldsymbol{\phi}_{k,u}) \tag{4.25}$$

Where $\boldsymbol{G}$ is the search space, which is defined as:

$$\boldsymbol{G} = \left\{ \boldsymbol{q} \in \mathbb{R}^3 : \|\boldsymbol{q} - \boldsymbol{q}_u(t-1)\|_2 \leq V_{th} \times T_L \right\} \tag{4.26}$$

where $\boldsymbol{q}_u(t-1)$ is the position of u-th VR user in the previous time instant, V_{th} is the maximum velocity of user movement, and T_L is the time interval between two successive localization instances.

To obtain $\boldsymbol{\phi}^*_{k,u}$, we propose a gradient descent-based approach to find a more precise value, which can be expressed as:

$$\boldsymbol{\phi}^{i+1}_{k,u} = \boldsymbol{\phi}^{i}_{k,u} + \lambda \nabla f(\boldsymbol{\phi}^{i}_{k,u}) \tag{4.27}$$

Where $\boldsymbol{\phi}^1_{k,u} = \boldsymbol{\phi}_{k,u}(t-1)$ represents the AoD corresponding to the user's position at the previous time slot, $\nabla f(\boldsymbol{\phi}^i_{k,u}) = \frac{\partial f}{\partial \phi}$ is defined as the gradient and λ is the predefined learning rate. When $\nabla f(\boldsymbol{\phi}^i_{k,u}) \leq \varepsilon$, the iteration stops. Note that for a VR user at time slot t, the location $\boldsymbol{q}_u(t-1)$ is taken as a priori knowledge. Consequently, a comprehensive spatial search is required only at the initial time t_0. The entire process of the proposed AoD estimation algorithm is shown in Algorithm 1.

Algorithm 5 AoDs Estimation Algorithm

1: **Input:** $\boldsymbol{y}_k, \boldsymbol{G}$
2: **Output:** Estimated AoD $\boldsymbol{\phi}^*_{k,u}$
3: **Initialization:** $\boldsymbol{G}, f(\boldsymbol{\phi}_{k,u}(t-1)), \lambda, \varepsilon$
4: Set $\boldsymbol{\phi}^1_{k,u} = \boldsymbol{\phi}_{k,u}(t-1)$
5: **for** i = 0,1,..., K **do**
6: Calculate $\boldsymbol{\phi}^i_{k,u}$ based on Eq. (4.27)
7: **while** $\nabla f(\boldsymbol{\phi}^i_{k,u}) > \varepsilon$ **do**
8: Update $\boldsymbol{\phi}^*_{k,u} = \boldsymbol{\phi}^i_{k,u}$
9: **end while**
10: **end for**

4.4.3 AoD-based Localization

Following the estimation of AoDs, we propose an iterative algorithm based on AoDs to estimate the position of each UE. Based on Section III, the geometric relationship of the UE position and AoDs can be expressed as:

$$\boldsymbol{\phi}^*_{k,u} = \arccos\left(\frac{(\boldsymbol{q}_k - \boldsymbol{q}_u)\boldsymbol{O}_k}{\|\boldsymbol{q}_k - \boldsymbol{q}_u\|_2}\right) + \boldsymbol{\eta}_{k,u} \tag{4.28}$$

where $\boldsymbol{\phi}^*_{k,u}$ is the estimated AoD from k-th RIS to u-th VR user, $\boldsymbol{O}_k \in \mathbf{SO}(3)$ is the orientation matrix for k-th RIS, and $\boldsymbol{\eta}_{k,u}$ is the estimation error. With knowledge of the RIS locations, the AP uses beamforming to communicate through a specific RIS in each time slot. As shown in Fig. 5.4, since the position of the VR user $\boldsymbol{q}_u$ is a three-dimensional coordinate, we can estimate the location of the VR user when there are AoDs from three different RIS. By iterating through $\boldsymbol{N}, (\boldsymbol{N} = 3)$ selected RISs, the AP collects a set of estimated AoDs of u-th VR user, denotes as $\left[\boldsymbol{\phi}^*_{1,u}, \boldsymbol{\phi}^*_{2,u}, \dots, \boldsymbol{\phi}^*_{\boldsymbol{N},u}\right]$.

To obtain an accurate estimation of $\boldsymbol{q}_u$, a least square criterion is applied, which can be denoted as:

$$\begin{aligned} (\mathbf{P2}) \quad & \min \sum_{n=1}^{\boldsymbol{N}} \|\boldsymbol{\phi}^*_{n,u} - \boldsymbol{\phi}_{n,u}(\boldsymbol{q}_u)\|_2^2 \\ & \text{s.t.} \quad \boldsymbol{q}_u \in \boldsymbol{S} \end{aligned} \tag{4.29}$$

where $\boldsymbol{\phi}_{n,u}(\boldsymbol{q}_u)$ is the actual AoD from n-th RIS to u-th VR user. To solve the above optimization problem ($\mathbf{P2}$), we apply Taylor-series estimation method. Without loss of generality, we assume that the actual positions for the UE are uniformly distributed around the estimated location $\hat{\boldsymbol{q}}_u$ [82]. With an initial estimation location $\hat{\boldsymbol{q}}_u$, we can iteratively obtain a more precise location for the UE based on the following formulation:

$$\boldsymbol{\phi}_{n,u}(\boldsymbol{q}_u) \approx \boldsymbol{\phi}_{n,u}(\hat{\boldsymbol{q}}_u) + (\boldsymbol{q}_u - \hat{\boldsymbol{q}}_u)^T \nabla \boldsymbol{\phi}_{n,u}(\hat{\boldsymbol{q}}_u) \tag{4.30}$$

where $\nabla \boldsymbol{\phi}_{n,u}(\hat{\boldsymbol{q}}_u)$ is the gradient at the estimation position $\boldsymbol{\phi}_{n,u}(\hat{\boldsymbol{q}}_u)$. Therefore, the corresponding mean squared error (MSE) can be expressed as:

$$\Delta(\boldsymbol{\phi}) \approx \boldsymbol{A}^T \Delta(\boldsymbol{q}_u) + \boldsymbol{\eta}_n \tag{4.31}$$

where $\boldsymbol{\eta}_n = [\eta_1, \dots, \eta_n]$, $\Delta(\boldsymbol{q}_u) = \hat{\boldsymbol{q}}_u - \boldsymbol{q}_u$, and

$$\Delta(\boldsymbol{\phi}) = [\phi_1^* - \phi_1(\hat{\boldsymbol{q}}_u), \dots, \phi_{\boldsymbol{N}}^* - \phi_{\boldsymbol{N}}(\hat{\boldsymbol{q}}_k)] \tag{4.32a}$$

$$\boldsymbol{A} = [\nabla(\phi_1(\hat{\boldsymbol{q}}_u)), \nabla(\phi_2(\hat{\boldsymbol{q}}_u)) \dots, \nabla(\phi_{\boldsymbol{N}}(\hat{\boldsymbol{q}}_u))] \tag{4.32b}$$

Therefore, the MSE of the position can be expressed as:

$$\boldsymbol{L}(\Delta(\boldsymbol{q}_u)) = (\boldsymbol{A}\boldsymbol{A}^T)^{-1} \boldsymbol{A} \nabla(\boldsymbol{\phi}) \tag{4.33}$$

Following Eq. (4.33), we update the estimated position of $\boldsymbol{q}_u$ based on:

$$\hat{\boldsymbol{q}}_u \leftarrow \hat{\boldsymbol{q}}_u + \boldsymbol{L}(\Delta(\boldsymbol{q}_u)) \tag{4.34}$$

Repeat this process until $\boldsymbol{L}(\boldsymbol{q}_u) < \zeta$, where ζ is the predefined threshold. The entire process is summarized as Algorithm 2. Note that while the algorithm is described for positioning a single user, it is designed to be run by the VR client. Algorithm 2 allows all users in the system to perform the positioning process in parallel, enabling the simultaneous localization of all users.

4.4.4 Boundary of Localization

Based on the system model introduced above, the unknown parameters of the UE location $\boldsymbol{q}_u$ can be represented as:

$$\boldsymbol{\xi}_u = [\boldsymbol{\theta}_u, \boldsymbol{\phi}_u, \boldsymbol{\alpha}_u]^T \in \mathbb{R}^{6K} \tag{4.35}$$

where $\boldsymbol{\theta}_u = \left[\theta_{1,u}, \theta_{2,u}, \dots, \theta_{k,u}\right]^T \in \mathbb{R}^{2K}$ and $\boldsymbol{\phi}_u = \left[\phi_{1,u}, \phi_{2,u}, \dots, \phi_{k,u}\right]^T \in \mathbb{R}^{2K}$ are the AoAs and AoDs from all RISs to u-th UE, and $\boldsymbol{\alpha}_u = [\Re(\bar{\alpha}_{1,i}), \Im(\bar{\alpha}_{1,u}), \dots, \Re(\bar{\alpha}_{K,u}), \Im(\bar{\alpha}_{K,u})]^{\mathrm{T}} \in \mathbb{R}^{2K}$ is the path gain.

Algorithm 6 AoD-based Localization Algorithm

1: **Input:** Positions of all RISs $\boldsymbol{q}_k (k \in K)$, position of the AP $\boldsymbol{q}_p$, estimated AoDs $\boldsymbol{\phi}_{n,u}, (n \in \boldsymbol{N})$, threshold ζ
2: **Initialization:** The initial position $\hat{\boldsymbol{q}}_u$
3: **repeat**
4: With the given $\hat{\mathbf{q}}_u$, generate $\boldsymbol{\phi}_{n,u}(\hat{\mathbf{q}}_u)$, for all $n \in \boldsymbol{N}$ according to Eq. (4.32a) and $\mathbf{A}$ according to Eq. (4.32b).
5: Find the least square estimate of $\Delta(\mathbf{q}_u)$, i.e.,
6: $\boldsymbol{L}(\Delta(\mathbf{q}_u)) = (\mathbf{A}^T\mathbf{A})^{-1}\mathbf{A}\Delta\boldsymbol{\phi}$
7: Update $\hat{\mathbf{q}}_u$, i.e., $\hat{\mathbf{q}}_u \leftarrow \hat{\mathbf{q}}_u + \boldsymbol{L}(\Delta(\boldsymbol{q}_u))$
8: **until** $\|\Delta\mathbf{p}\|_2 < \zeta$

Let $\hat{\boldsymbol{\xi}}_u$ represents the unbiased estimate of $\boldsymbol{\xi}_u$, the MSE of $\hat{\boldsymbol{\xi}}_u$ is subject to the following:

$$\mathbb{E}\left\{\left(\hat{\boldsymbol{\xi}}_u - \boldsymbol{\xi}_u\right)\left(\hat{\boldsymbol{\xi}}_u - \boldsymbol{\xi}_u\right)^H\right\} \succeq \boldsymbol{J}(\boldsymbol{\xi}_u) \tag{4.36}$$

where $\boldsymbol{J}(\boldsymbol{\xi}_u) \in \mathbb{R}^{6K\times 6K}$ is the FIM matrix of $\boldsymbol{\xi}_k$. The element (m,n) of $\boldsymbol{J}(\boldsymbol{\xi}_u)$ is defined as:

$$[\boldsymbol{J}(\boldsymbol{\xi}_u)]_{m,n} \triangleq \mathbb{E}\left\{-\frac{\partial^2 \ln p(\mathbf{y}|\boldsymbol{\xi}_u)}{\partial \xi_m \partial \xi_n}\right\} \tag{4.37}$$

where $\ln p(\boldsymbol{y}_u|\boldsymbol{\xi}_u)$ is the likelihood function.

For a random vector $\boldsymbol{y}_k \sim \boldsymbol{CN}(\boldsymbol{\mu}_k, \boldsymbol{\Sigma}_k)$, the element at position (m,n) can be expressed as:

$$\begin{aligned}[\boldsymbol{J}(\boldsymbol{\xi})]_{m,n} = 2\Re\left\{\frac{\partial \boldsymbol{\mu}_k^{\mathrm{H}}}{\partial \xi_m}\boldsymbol{\Sigma}_k^{-1}\frac{\partial \boldsymbol{\mu}_k}{\partial \xi_n}\right\} \\ + \Im\left\{\boldsymbol{\Sigma}_k^{-1}\frac{\partial \boldsymbol{\Sigma}_k}{\partial \xi_m}\boldsymbol{\Sigma}_k^{-1}\frac{\partial \boldsymbol{\Sigma}_k}{\partial \xi_n}\right\}\end{aligned} \tag{4.38}$$

Based on Lemma 1, the $\boldsymbol{J}(\boldsymbol{\xi}_u)$ is defined as:

$$\boldsymbol{J}(\boldsymbol{\xi}_u) = \frac{2}{\sigma^2}\sum_{\bar{t}=1}^{N}\Re\left\{\nabla_{\boldsymbol{\xi}_k}\boldsymbol{\mu}_{k,\bar{t}}\left(\nabla_{\boldsymbol{\xi}_k}\boldsymbol{\mu}_{k,\bar{t}}\right)^{\mathrm{H}}\right\} \tag{4.39}$$

To estimate the position of UEs, we also defined the parameters of the UE position as $\boldsymbol{\rho}_k = [\boldsymbol{q}_k, \boldsymbol{\psi}_k, \boldsymbol{\alpha}_k]^T \in \mathbb{R}^{3+4K}$. The corresponding FIM matrix can be indicated as $\boldsymbol{J}(\boldsymbol{\rho}_k) = \boldsymbol{T}_k\boldsymbol{J}(\boldsymbol{\xi}_k)\boldsymbol{T}_k^T$, where $\boldsymbol{T}_k \in \mathbb{R}^{4K+3}$ is the Jacobian matrix, defined as $[\boldsymbol{T}_k]_{m,n} = \partial[\boldsymbol{\xi}_k]_m / \partial[\boldsymbol{\rho}_k]_n$ which can be calculated using the geometric relationship described in Section III.

In summary, the CRLB to determine the positions of the k-th UE can be described as the first 3×3 diagonal block for the trace of the inverse of the matrix, which is specified as follows:

$$\mathbf{CRLB} = \mathrm{tr}[\boldsymbol{J}^{-1}(\boldsymbol{\rho}_k)]_{1:3,1:3} \tag{4.40}$$

where **CRLB** corresponds to the upper limit of the system's positioning accuracy.

4.4.5 Location-based Beamforming

Due to the interdependence of the AP beamforming matrix $\boldsymbol{w}$, the codebook of RIS $\boldsymbol{C}$, and the users' beamforming vector $\boldsymbol{m}$, directly addressing problem (**P0**) presents a significant challenge. A two-step approach is proposed to optimize QoE by determining the VR user's location. Initially, Step I involves selecting the optimal RIS for reflection based on geometric relationships and optimizing the beamforming matrix of AP. Subsequently, Step II focuses on establishing the beam alignment of RISs and VR users to enhance the VR user's QoE. The details of Step I and Step II are described as follows.

Step I - Optimal RIS selection The mobility of VR users results in changing positions over time, which complicates the selection of the appropriate RIS, as shown in Fig. 4.1. For any given time block t, the path loss from the AP to the u-th VR user via the k-th RIS is given by:

$$PL_k^u(t) = \left(\left(\frac{\lambda}{4\pi}\right)^4 \frac{G_p G_k G_u F(\boldsymbol{\theta}_{p,k}) F(\boldsymbol{\phi}_{k,u})}{\left\|\boldsymbol{q}_{p,k}\right\|_2^2 \left\|\boldsymbol{q}_{k,u}\right\|_2^2}\right)^{-1} \tag{4.41}$$

Using the estimated VR user position $\hat{\boldsymbol{q}}_u(t)$, we can calculate the path loss $PL_k^u(t)$ through the k-th RIS. Therefore, we acquire a set $\left\{PL_1^u(t), PL_2^u(t), \ldots, PL_K^u(t)\right\}$, indicating the path losses through different RIS for u-th VR user at t-th time block. Comparing these path losses allows us to select the RIS $\boldsymbol{q}_u^*(t)$ with the minimum loss as the optimal communication path for the u-th VR user during that time block. Knowing which RISs are in use, we optimize the AP's beamforming matrix $\boldsymbol{w}$. The positions of the selected RISs guide us in precisely directing the AP's beamforming, simplifying the optimization of $\boldsymbol{w}$. This process ensures the AP's beamforming vectors are aligned with the directions of the chosen RISs, enhancing the signal transmission path for improved signal strength and quality at the VR user's end.

Step II - Fast beam selection Once the AP's beamforming matrix $\boldsymbol{w}$ has been determined, we can further optimize the beamforming direction of RISs and VR users. Utilizing the VR user's positional information allows us to narrow the search for suitable codewords in the beam alignment process, effectively reducing latency. At t-th time block, the estimated position of u-th VR user can be denoted as $\hat{\boldsymbol{q}}_u(t) = \boldsymbol{q}_u(t) + \boldsymbol{\Sigma}_t$, where $\boldsymbol{\Sigma}_t$ represents the estimation error of t-th time block. According to [12], we assume that actual position of VR user $\boldsymbol{q}_u(t) \sim N(\hat{\boldsymbol{q}}_u(t), \boldsymbol{\Sigma}_t)$, where $N(\cdot)$ represents the Gaussian distribution. Therefore, the

Algorithm 7 Location-based Beamforming for VR Users

```
Input: t, q̂_u(t), Σ_t, C
Output: Optimized w, c_l, m
Step I: Optimal RIS Selection
for each VR user u at time block t do
    Calculate path loss PL_k^u(t) for each RIS k according to Eq. (4.41)
    Determine q_u^*(t) with minimum PL_k^u(t)
end for
Optimize AP's beamforming matrix w using selected RISs
Step II: Fast Beam Selection
for each selected RIS at time block t do
    Estimate scan space S'(t) using q̂_u(t) and Σ_t
    for each codeword c_l in S'(t) do
        Scan the S'(t) for each VR user and corresponding RIS
    end for
    Select optimal c_l and m for RIS and VR user
end for
```

scan space for each selected RIS of t-th time block can be denoted as:

$$\boldsymbol{S}^{'}(t) = \{\boldsymbol{c}_l \in \boldsymbol{C} \mid l \in [l_{\min}, l_{\max}]\} \tag{4.42}$$

where

$$l_{\min} = \max\left(1, \lfloor L \cdot F(\hat{\boldsymbol{q}}_u(t) - \sigma_{\text{angle}}) \rfloor\right) \tag{4.43}$$

$$l_{\max} = \min\left(L, \lceil L \cdot F(\hat{\boldsymbol{q}}_u(t) + \sigma_{\text{angle}}) \rceil\right) \tag{4.44}$$

Where $F(\cdot)$ denotes the function that maps the estimated user position's angular change to the codeword indices in the codebook, σ_{angle} represents the standard deviation of the angular variation caused by the positional estimation error $\boldsymbol{\Sigma}_t$. After defining the scan space $\boldsymbol{S}^{'}(t)$ for each time block, we achieve beam alignment for every VR user by scanning within $\boldsymbol{S}^{'}(t)$. This critical step ensures the QoE by aligning beams with the users' current positions and their chosen RIS. The system automatically repeats this process whenever there is a change in user position, maintaining the quality of communication. The entire process is summarized as Algorithm 3.

Complexity Analysis: The computational complexity of the proposed algorithm mainly depends on the localization algorithm. Within the localization algorithm, the gradient calculation determines the complexity, which can be expressed as $\boldsymbol{O}(KN_pN_kN_uN)$, where K is the iteration number. The beam selection complexity is $\boldsymbol{O}(1)$ based on the localization.

Table 4.1 Simulation Parameters

Parameters	**Values**
Communication frequency f_o	30 GHz
Antenna gain of AP G_p	20 dbi
Antenna gain of UE G_u	4 dbi
The boresight gain of RIS G_k	6 dbi
Number of antennas in AP N_p	4
Number of antennas in UE N_u	2
Number of antennas in RIS N_k	6×6
Location of AP $\boldsymbol{q}_p$	$[0,5,2]$
Position of RISs $\boldsymbol{q}_k$	[3,10,1] ,[7,10,1] [3,0,1], [7,0,1]
AP transmit power	30 dBm
Noise power σ^2	-85 dbm

4.5 Simulation Results

In the multi-RIS-assisted mmWave VR scenario, the QoE for VR users is significantly influenced by three main factors: the accuracy of position estimation, the latency of VR interaction, and the downlink transmission rate. We conduct extensive and comprehensive experiments in this section to demonstrate the efficacy of our proposed multi-RIS-assisted mmWave VR system.

4.5.1 Simulation Scenario and Settings

In our simulation of a multi-RIS-assisted wireless VR system, we depict an indoor environment measuring $10\text{m} \times 10\text{m} \times 2\text{m}$. A single AP, positioned at $[0,5,2]$, caters to two VR users with four RISs. These RISs are strategically placed at $[3,10,1]$, $[7,10,1]$, $[3,0,1]$, and $[7,0,1]$. Each RIS features a 6×6 UPA of elements. The AP has four ULA antennas ($N_p = 4$), while each UE includes two antennas ($N_u = 2$). The VR users' movements are confined to the $x-y$ plane, adhering to the VRMM. Initially, each UE is positioned at a distinct starting location and moves randomly through the space. For comprehensive details, refer to Table I for the simulation parameters.

4.5.2 Performance of AoD-based Positioning

In our experimental evaluation, we analyze the localization performance using the root mean square error (RMSE) as a metric to quantify the accuracy of position estimation, which can be defined as:

$$\text{RMSE} = \mathbb{E}\left\{\sqrt{\frac{1}{U}\sum_{u=1}^{U}\|\hat{\mathbf{q}}_u - \mathbf{q}_u\|^2}\right\} \tag{4.45}$$

Where U is the number of VR users, this formula calculates the average distance between the estimated positions $\hat{\mathbf{q}}_u$ and the actual positions $\mathbf{q}_u$ of the VR users, providing a precise measure of the estimation accuracy.

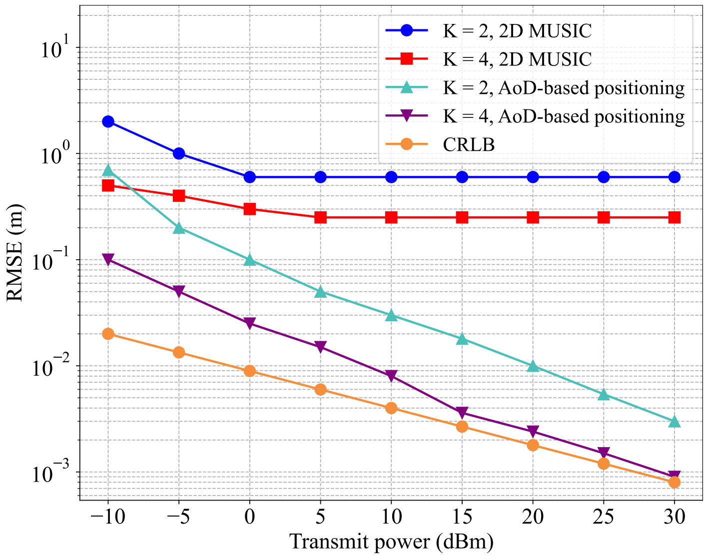

Fig. 4.6 The accuracy of the proposed AoD-based positioning algorithm versus transmit power.

We evaluate the localization performance by comparing the two-dimensional multiple signal classification (2D MUSIC) algorithms [84], which localizes users by analyzing the spatial spectrum, with our proposed AoD-based positioning method.

Fig. 5.5 demonstrates how the RMSE of localization varies with transmit power for different numbers of RISs used in positioning users. It is evident that the AoD-based positioning method consistently surpasses the 2D MUSIC algorithm at all transmit power levels and, with any number of RISs, closely approaches the CRLB at higher power values. The AoD-based positioning method demonstrates superior accuracy over the 2D MUSIC algorithm because it directly utilizes the geometric information of the AoD, which is less susceptible to the noise and interference that typically affect spectral estimation methods. The CRLB represents a theoretical minimum variance for any unbiased estimator, serving as a benchmark for evaluating the RMSE. As transmit power increases, the SNR improves, leading to more precise localization. Simultaneously, using more RISs for positioning introduces additional reflective paths, thereby increasing the accuracy of the localization process.

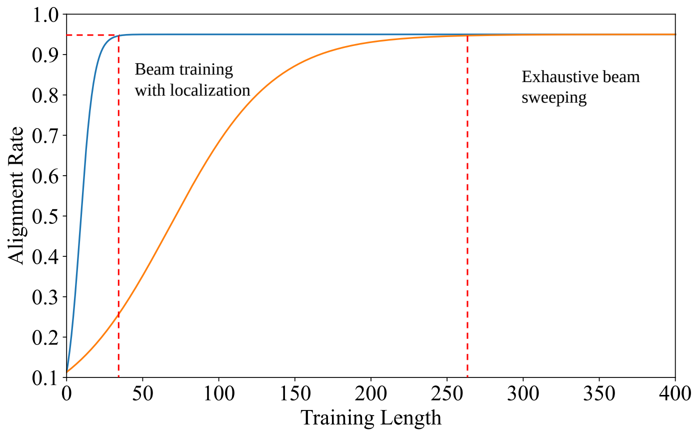

Fig. 4.7 Alignment rate comparison between the proposed localization-based beamforming and exhaustive beam sweeping.

Fig. 5.6 compares our proposed location-based beam selection method against the exhaustive beam sweeping approach. Exhaustive beam sweeping involves iterating through every codeword in the RIS codebook without user location information, with the codebook size set at 256. Utilizing positional information, our method effectively reduces the search space, markedly improving alignment rate efficiency. This improvement is highlighted by the sharp initial slope, indicating rapid achievement of near-optimal alignment with shorter training length. In contrast, exhaustive beam sweeping undertakes a complete search through the codebook's codewords, resulting in a slower incremental improvement in alignment rate. The findings underscore our method's advantage in speed and efficiency, which is crucial for mmWave VR systems that demand quick and accurate beam alignment.

4.5.3 Performance of Our Proposed Algorithm

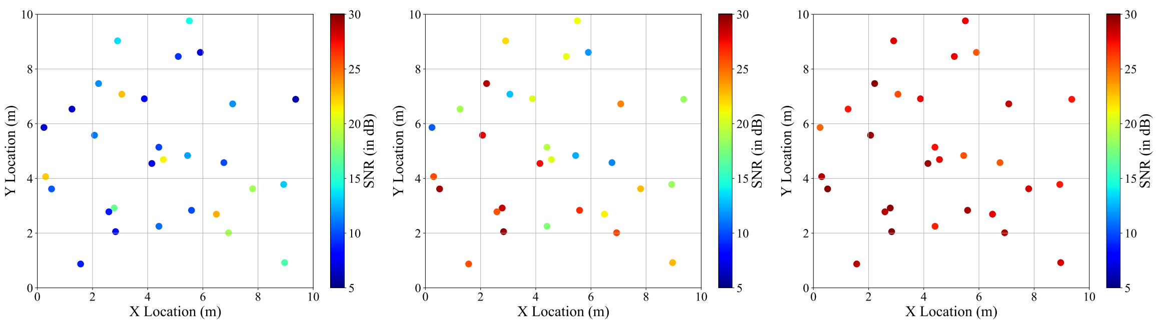

(a) Random RIS phase shift (b) Fixed beamforming direction (c) Our proposed algorithm

Fig. 4.8 Comparison of VR user SNR under different RIS optimization algorithms.

In this subsection, we detail the outcomes of numerical experiments conducted to validate the efficacy of our proposed localization-based beam selection algorithm within a multi-RIS-assisted wireless VR system. To benchmark our algorithm's performance, we compare it against a selection of algorithms, detailed as follows:

- **AO with perfect CSI:** adaptive optimization (AO) [19] with perfect CSI is considered as the upper bound for performance comparison. It operates assuming complete and accurate CSI, allowing for optimal beamforming and serving as an ideal benchmark.
- **Exhaustive beam sweeping:** The exhaustive beam sweeping method uses a discrete Fourier transform (DFT) codebook to perform spatial scanning. Due to the lack of user location information, it is constrained to a smaller codebook size, which reduces the beamforming effectiveness.
- **Single RIS:** This approach involves the deployment of a single RIS in the environment, which is designed to compare the performance of multi-RIS and single-RIS.
- **Random RIS:** The random RIS method serves as the performance lower bound in our comparison, where the RIS elements are assigned random phase shifts.

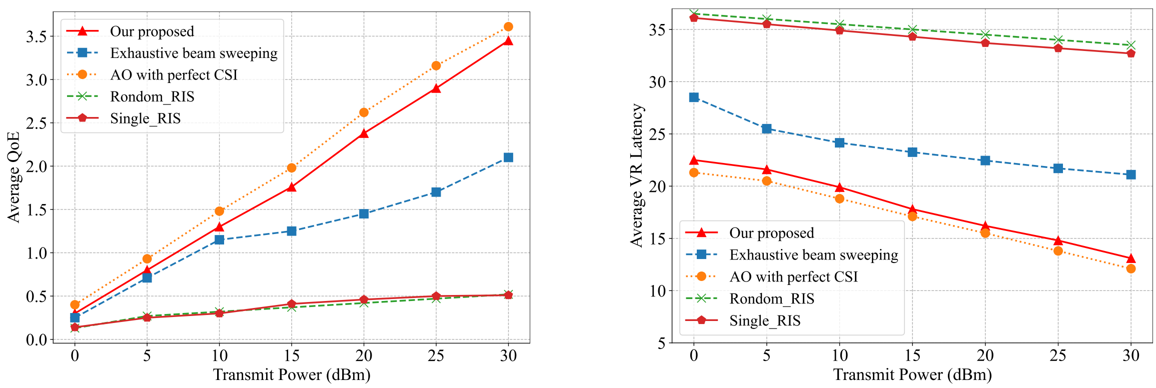

(a) Average QoE (b) Average VR latency

Fig. 4.9 The effect of the transmit power on the average QoE and average VR latency in the proposed multi-RIS-assisted mmWave wireless VR network.

Initially, we evaluate our proposed algorithm's performance in a scenario where VR users randomly move within space $\boldsymbol{S}$, utilizing a multi-RIS-assisted mmWave VR system. This evaluation seeks to determine the algorithm's adaptability to dynamic changes in user positions. We introduce three distinct scenarios for this purpose: (1) Random RIS phase shift, indicating that each RIS's configuration is random, reflecting signals in all directions with low gain; (2) Fixed beamforming direction, where the RISs' beamforming direction is constant, unaffected by changes in users' positions; and (3) Our proposed algorithm, which dynamically adjusts the RIS beamforming direction based on VR users' locations.

As shown in Fig. 4.8, we show the user's SNR at 30 locations. According to [1], the minimum SNR required to meet the needs of VR users is established at 20 dB. The results show that the fixed RIS beamforming can improve the SNR of VR users compared with the random RIS phase shift. However, due to the mobility of users, there are still some locations where the SNR is below 20 dB. Our proposed method allows accurate beam alignment to be maintained even during the user's movement by localization. Fig. 4.8 shows the importance of localization and highlights that our proposed algorithm can provide high SNR performance in all locations, thereby enhancing the QoE of VR users.

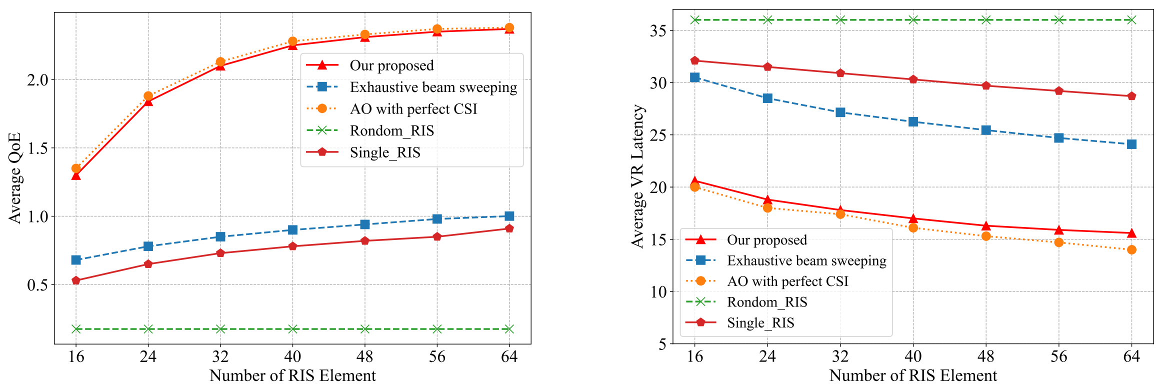

(a) Average QoE (b) Average VR latency

Fig. 4.10 The effect of the number of RIS element on the average QoE and average VR latency in the proposed multi-RIS assisted mmWave wireless VR network.

Fig. 5.7 shows the impact of transmission power P_t on the average QoE and latency in a multi-RIS-assisted mmWave VR system. Increasing transmit power enhances the average QoE for all strategies, with our approach surpassing others and closely matching the performance of AO with perfect CSI. This underscores the effectiveness of higher transmit power in improving VR users' QoE. The low QoE with the random RIS strategy underscores the need for accurate beam alignment in mmWave VR systems. Additionally, the single RIS strategy's difficulty localizing and tracking users due to limited reflection paths results in lower QoE. Fig. 9(b) examines how transmit power P_t affects average VR latency. Higher transmit power reduces latency across all methods thanks to faster downlink transmission rates that meet a VR interaction delay limit of 20ms. Our algorithm enhances beam alignment speed in dynamic environments, reducing VR latency. In contrast, the Single RIS and Random RIS strategies face challenges in beam alignment due to user movement, leading to higher latency. Also, the exhaustive beam-sweeping strategy, which scans the entire environment, leads to more significant latency than our method. These findings highlight our algorithm's capability to maintain high QoE for VR users at different transmit power levels.

Fig. 5.8 demonstrates how increasing the number of RIS elements influences the average QoE and latency in a multi-RIS-assisted mmWave VR system. As shown in Fig. 10(a), a marked enhancement in average QoE is observed with a higher count of RIS elements. Our method outperforms the benchmarks, closely emulating the outcomes achieved by AO with perfect CSI. This improvement stems from the augmented path gains and more focused beams provided by the additional RIS elements, facilitating the dynamic adaptation of beam directions to users' locations and, thus, elevating VR users' QoE. Nonetheless, a more significant number of RIS elements also escalates the complexity of the optimization challenge, underscoring the importance of judiciously determining the optimal quantity of RIS elements. Fig. 10(b) illustrates that average VR latency diminishes with increased RIS elements. This latency reduction is attributed to our approach's capacity for swift and precise beam alignment, boosting downlink transmission rates and curtailing latency to adhere to the VR interaction delay benchmark of 20ms. Conversely, strategies involving a Single RIS or Random RIS configurations falter in beam alignment amid user movements, leading to protracted latencies. Moreover, the exhaustive beam sweeping method, necessitating a scan of the entire environment, incurs additional delays compared to our streamlined approach.

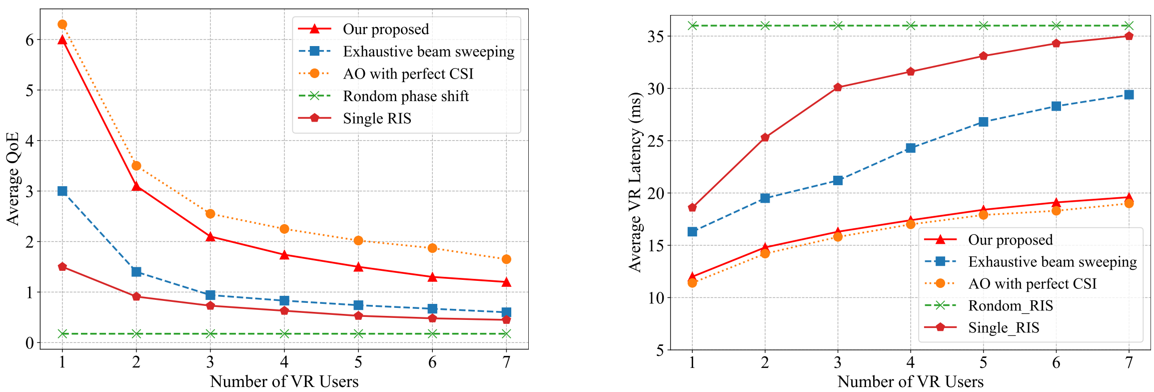

(a) Average QoE (b) Average VR latency

Fig. 4.11 The effect of the number of VR users on the average QoE and average VR latency in the proposed multi-RIS-assisted mmWave wireless VR network.

Fig. 5.9 illustrates the impact of the number of VR users on the average QoE and latency within a multi-RIS-assisted mmWave VR system. As depicted in Fig. 11(a), there is a noticeable decline in the average QoE as the user count increases due to the shared wireless resources and escalating interference among users. Despite this challenge, our proposed method consistently outperforms other strategies, offering a level of QoE that nearly parallels that of the AO with a perfect CSI approach. Fig. 11(b) reveals that average latency for VR users increases with the number of users. This rise in latency is attributed to the augmented interference stemming from a higher user density, which diminishes the efficiency of downlink communication, thereby extending latency. Compared to competing algorithms, excluding the AO with perfect CSI, our methodology exhibits the lowest latency, affirming its efficacy in environments populated by multiple users.

4.6 Conclusion

This paper introduced a localization-based beamforming algorithm to optimize the QoE for VR users in an indoor, multi-RIS-assisted mmWave VR system. The proposed algorithm ensures a stable wireless connection with high transmission rates, addressing blockages and user mobility effectively. Initially, an AoD-based localization algorithm was developed to accurately estimate the real-time locations of VR users, facilitating dynamic movement tracking. Leveraging this precise location data, our approach employs a novel, rapid beam alignment technique to enhance VR users' QoE under VR interaction latency constraints. Simulation results show that our proposed beam selection strategy achieves a 95% beam alignment success rate. Even with imperfect CSI, our localization-based beamforming algorithm performs comparably to the benchmark set by perfect CSI. Additionally, it was observed that increasing transmission power and the number of RIS elements improves QoE, whereas a higher number of VR users tends to diminish it. Importantly, the RIS-assisted network demonstrated here is particularly suited for consumer electronics applications, offering significant potential for various mobile communication scenarios.

Chapter 5

QoE Optimization for Mobile Users Based on User Movements for IoRT Scenario

With the evolution of robotics and Internet of things (IoT) technologies, the Internet of robotic things (IoRT) has emerged as novel technological paradigm, attracting widespread attention from academic and industrial communities [60]. IoRT is considered as a potential solution for improving human life quality, introducing more intelligent, autonomous systems that alleviate the human burden of engaging in dangerous and monotonous tasks [61, 94]. To realize this vision, we still face some unique challenges, including how to support intelligent AI models on robots with limited resources such as computing and barriers, high transmission rate under unstable wireless channels, high accuracy sensing even under dense obstacle environments, and how to maintain the seamless connection for multiple robots in a dynamic environment [32]. Unlike general IoT systems, IoRT requires real-time sensing and decision-making capabilities in dynamic and often unpredictable environments, which necessitates a high level of integration between sensing, computing, and communication. [33]

To tackle these challenges, integrated sensing, computing and communication (ISCC), emerging as a breakthrough technology of 6G, can be a promising enabler for IoRT, enabling low latency, high transmission rate and high reliability [23]. By integrating communications and sensing capabilities and offloading computational tasks to mobile edge computing (MEC), ISCC allows for real-time data processing and decision-making at the network's edge, reducing latency and improving spectral efficiency and power consumption for IoRT systems [20]. However, the high frequency of 6G signals leads to severe propagation attenuations and reduces their ability to bypass obstacles, which results in unstable wireless links between IoRT devices and MEC [47]. In practical scenarios, obstacles like buildings and trees can block the line-of-sight (LoS) channel between IoRT devices and MEC, leading to increased offloading delays in MEC and reduced sensing accuracy, thereby compromising ISCC's performance [59].

Fortunately, reconfigurable intelligent surface (RIS) sheds light on the above challenge by establishing LoS links, thereby enhancing the quality of wireless channel [49]. RIS consists of a digital controller and an array of massive passive elements, which is capable of dynamically adjusting phase shifts in response to incident electromagnetic waves. From one perspective, RIS has been proved to enhance the transmission rate by improving the wireless channel, significantly reducing offloading delays in MEC scenarios. Specifically, the author of [34] proposed a joint optimization algorithm to minimize the offloading latency in RIS-assisted MEC framework. The authors of [77] focused on reducing the system delay in multi-RIS-assisted MEC scenarios where RIS was adopted to enhance the transmission rate. The author of [16] presented a double-RIS-assisted offloading scheme for non-orthogonal multiple access (NOMA) MEC to reduce the offloading and transmission time. From another perspective, existing studies have also shown that RIS can play an important role in improving the accuracy of user sensing and tracking. In specific, the author of [13] introduced the utilization of RIS in an integrated sensing and communication (ISAC) system to enhance detection and localization accuracy, by improving the received signal strength in receiver.

It is important to note that with the rapid development of RIS-assisted MEC networks and RIS-assisted ISAC systems, the performance of RIS-assisted ISCC systems has also garnered significant research attention, demonstrating potential enhancements in integrated communication, sensing, and computational capabilities. The authors of [74] employed RIS to facilitate the task offloading process between users and MEC, and an algorithm was proposed to minimize the system delay. In [85], the RIS was employed as a passive information carrier in an ISCC system, and the results showed that the proposed framework could enhance the weighted throughput capacity performance.

Motivated by the aforementioned considerations, this paper introduces a RIS-enabled ISCC system tailored for IoRT scenarios, where the RIS is deployed to enhance the wireless transmission rate for offloading local tasks to MEC, thereby improving the reliability and reducing latency of robotic operations in complex environments. The main contributions of this paper are summarized as follows.

- We propose an RIS-enabled ISCC system for IoRT scenarios, where RIS is employed to enhance the transmission rate of task offloading process. In our proposed network, we aim to enhance QoS of ISCC system by jointly optimizing the communication precoding matrix of BS, the phase shift matrix of RIS, the offloading volume, the edge computing resource allocation, and sensing beamforming matrix of robot.

- A block coordinate descent (BCD) based algorithm is introduced to decouple the QoS optimization problem into two sub-problems. These are named as follows: the minimization of computing latency in stage-I and the maximization of transmission rate and sensing accuracy in Stage-II. Specifically, in stage-I, the minimization computing latency problem is solved by applying KarushKuhn-Tucker (KKT) conditions and the bisection search. In stage-II, we first utilize the alternating optimization (AO) algorithm to further decompose the problem. Through iterative optimization, we identify an approximate optimal configuration of the RIS and BS beamforming vectors to maximize the communication rate. Additionally, we introduce a codebook-based global scanning strategy to enhance the perceptual accuracy of the robots.
- Extensive simulations are conducted to verify the effectiveness of the proposed RIS-enabled ISCC system for IoRT scenarios and the advantages of employing RIS.

5.1 Related Work

RIS, known for its capabilities to control the propagation for wireless signals, is employed to enhance the performance of IoT system. In [97, 37, 5, 95], the coverage, reliability, transmission rate, and energy consumption of RIS-assisted network were analyzed. Specifically, the authors of [97] introduced a weighted gradient descent algorithm for jointly optimizing the positions and orientations of RISs to maximize the wireless network coverage. In [37], the reliability of RIS-assisted NOMA IoT system was investigated, and the result indicated that the integration of RIS can effectively improve the reliability of network. The authors of [5] investigated RIS-assisted multi-user indoor communications, and a majority voting optimization method was proposed to optimize the configuration of RIS. Experimental results indicated that the average received signal strength increased by 9.5 times compared to scenarios without RIS. In [95], the authors deployed RIS on a IoT system to minimize the energy consumption by jointly optimizing the passive beamforming of RIS, the active beamforming of BS and user association. However, the above works have primarily focused on leveraging RIS to enhance the communication performance of IoT systems, ignoring the immense potential of 6G signals in integrated sensing, computing, and communication.

Some works have demonstrated the effectiveness of RIS in enhancing the performance of ISCC systems [30, 101, 36, 81]. Specifically, the authors of [30] proposed a two-timescale transmission design for multiple RIS-assisted ISAC system, where RIS not only improved the transmission rate, but also enhanced the sensing accuracy. In [101], the potential of employing active RIS in ISAC system is explored, and focused on optimizing transmit beamformers, RIS reflections, and radar receive filters to maximize radar SNR and maintain communication SINR. In [36], the authors investigated the performance of RIS-assisted ISAC system and maximized the average achievable capacity through joint optimization of the time resource allocation between sensing and communication at the BS and the precoding matrix at the RIS. The authors of [81] deployed RIS on dual-functional unmanned aerial vehicle (UAV)-enabled ISAC system to enhance the weighted sum of average sum-rate and SNR by optimizing the phase shift of RIS, the trajectory of UAV and the dual-functional-radar-communication beamforming of the system. Nevertheless, these studies mainly focused on optimizing phase shifters and beamforming vector to enhance the communication and sensing performance of the network, overlooking how to effectively handle massive disturbed ISAC data and utilize MEC to alleviate computational burdens and reduce computing latency for users.

Moreover, the performances of RIS-assisted IoRT systems were further explored in [57, 28]. Specifically, in [57], a novel RIS-assisted ISCC framework was introduced to optimize resource allocation, improve reliability, and enhance data processing speeds. The author of [28] utilized RIS to enhance the quality of wireless channel from users to MEC, aiming to improve the energy efficiency of the RIS-assisted ISCC system. However, the above works mainly concentrated on multi-input single-output (MISO) scenarios, which may not align in the real-world application. While the state of art has investigated a wide range of details in sensing and communications, the majority of these works fall short in investigating the sensing accuracy. Therefore, in this work, we propose a RIS-enabled ISCC system specifically tailored for IoRT scenarios, which optimizes sensing accuracy, computing latency, and transmission speed simultaneously, thereby enhancing the performance of IoRT systems.

5.2 System Model and Problem Formulation

5.2.1 Communication Model

In this paper, we consider an RIS-enabled ISCC system in IoRT scenarios as shown in Fig. 1, which consists of K robots with M antennas, an RIS with N reflective elements, and a L-antennas BS linked to an MEC. In the proposed IoRT scenarios, we assume that each robot is capable of performing target sensing while concurrently offloading computational tasks to the BS via communication links. Due to the obstacles may block the LoS path from robots to BS, RIS is deployed to enhance the communication rate during task offloading. We denote the set of robots and elements of RIS as $\mathscr{K} = \{1,\ldots,k,\ldots,K\}$, $\mathscr{N} = \{1,\ldots,n,\ldots,N\}$, respectively. It is worth nothing that, in this paper, we make a reasonable assumption that

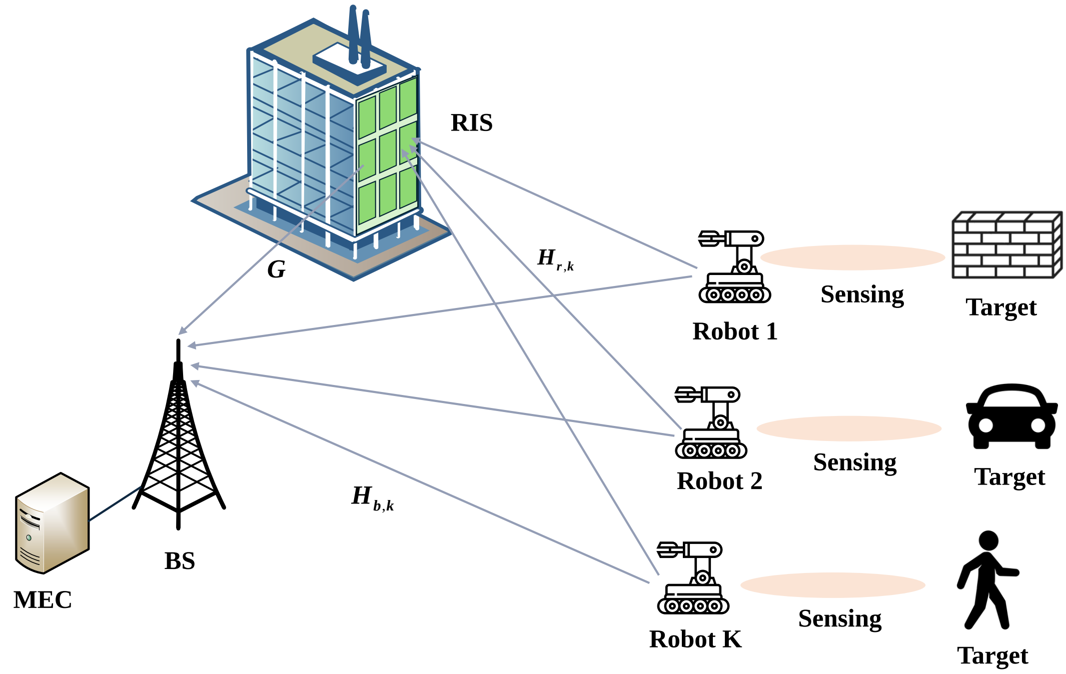

Fig. 5.1 System model of RIS-enabled ISCC system for IoRT scenarios.

RIS does not have the impact of the sensing capabilities of robot due to the spatial separation between the BS and the detection target.

By defining the communication channel from k-th robot to RIS, RIS to BS, and k-th robot to BS as $\mathbf{H}_{r,k} \in \mathbb{C}^{N\times M}$, $\mathbf{G} \in \mathbb{C}^{L\times N}$ and $\mathbf{H}_{b,k} \in \mathbb{C}^{L\times M}$, respectively, the channel matrix from k-th robot to BS $\mathbf{H}_k$ can be represented as:

$$\mathbf{H}_k = \mathbf{H}_{b,k} + \mathbf{G}\boldsymbol{\Theta}\mathbf{H}_{r,k} \in \mathbb{C}^{L\times M} \tag{5.1}$$

where $\boldsymbol{\Theta} = \mathrm{diag}\left\{e^{j\theta_1}, \cdots, e^{j\theta_N}\right\} \in \mathbb{C}^{N\times N}$ is the phase shift matrix of RIS and $\theta_n \in (0, 2\pi], \forall n \in \mathscr{N}$. Therefore, the received signal of BS can be given by:

$$\mathbf{y}_b = \sum_{k=1}^{K} \mathbf{H}_k \mathbf{x}_k + \mathbf{n}_b \in \mathbb{C}^{L\times 1} \tag{5.2}$$

where $\mathbf{x}_k \in \mathbb{C}^{M\times 1}$ is transmit signal of k-th robot, $\mathbf{n}_b \in \mathbb{C}^{L\times 1} \sim \mathscr{CN}\left(\mathbf{0}, \sigma_b^2 \mathbf{I}_L\right)$ is the Additive White Gaussian Noise (AWGN). The power constraint of k-th robot can be denoted as:

$$\mathbb{E}\left[\mathbf{x}_k \mathbf{x}_k^{\mathrm{H}}\right] \leq P_k, \forall k \in \mathscr{K} \tag{5.3}$$

where P_k is the transmit power of k-th robot. Furthermore, the SINR of k-th robot can be formulated as:

$$\mathrm{SINR}_k = \frac{\left\| \left(\mathbf{G}\boldsymbol{\Theta}\mathbf{H}_{r,k} + \mathbf{H}_{b,k} \right) \mathbf{w}_k \right\|^2}{\sigma_k^2 + \sum_{j \neq k} \left\| \left(\mathbf{G}\boldsymbol{\Theta}\mathbf{H}_{r,k} + \mathbf{H}_{b,k} \right) \mathbf{w}_j \right\|^2} \tag{5.4}$$

where $\mathbf{w}_k \in \mathbb{C}^{M \times 1}$ and σ_k are the precoding matrix and AWGN of k-th robot, respectively. Therefore, the achievable off-loading rate of k-th robot can be expressed as:

$$R_k = B \log_2 \left(1 + \mathrm{SINR}_k\right) \tag{5.5}$$

where B represents the communication bandwidth.

5.2.2 Sensing Model

Based on the transmit signal $\mathbf{x}_k$, the received sensing signal of k-th robot can be formulated as:

$$\begin{aligned} \mathbf{y}_k = {} & \alpha_k \mathbf{a}_k^R(\theta_k) \mathbf{a}_k^T(\theta_k) \mathbf{x}_k \\ & + \sum_{j=1, j \neq k}^{K} \mathbf{H}_{k,j} \mathbf{x}_j + \mathbf{n}_k \in \mathbb{C}^{M \times 1} \end{aligned} \tag{5.6}$$

where α_k denotes the path loss of the sensing object positioned at θ_k, $\mathbf{a}_k^R(\theta_k) \in \mathbb{C}^{M \times 1}$ and $\mathbf{a}_k^T(\theta_k) \in \mathbb{C}^{1 \times M}$ represent the receive and transmit array response vectors for k-th robot, respectively. These vectors describe how signals are received and transmitted at a specific angle θ_k through an array of M antennas. $\mathbf{H}_{k,j} \in \mathbb{C}^{M \times M}$ denotes the channel matrix from k-th robot to j-th robot, and $\mathbf{n}_k \in \mathbb{C}^{M \times 1}$ is the AWGN with the covariance of δ_d^2. Therefore, the received sensing signal of k-th robot can be formulated as:

$$s_k = \mathbf{w}_{s,k} \mathbf{y}_k \tag{5.7}$$

where $\mathbf{w}_{s,k} \in \mathbb{C}^{1 \times M}$ is the sensing received beamforming vector for k-th robot.

The effectiveness of the sensing can be evaluated by the radar SINR. Following the implementation of receive beamforming, the radar SINR for k-th robot can be expressed as follows:

$$\beta_k = \frac{\left\| \mathbf{w}_{s,k} \alpha_k \mathbf{a}_k^R(\theta_k) \mathbf{a}_k^T(\theta_k) \mathbf{x}_k \right\|^2}{\left\| \mathbf{w}_{s,k} \sum_{j=1, j \neq k}^{K} \mathbf{H}_{k,j} \mathbf{x}_j + \mathbf{n}_k \right\|^2} \tag{5.8}$$

where β_k is the radar SINR for k-th robot.

5.2.3 Computing Model

According to [85], in RIS-assisted ISCC system, adopting a partial offloading strategy can achieve a better performance compared to a binary offloading strategy. This strategy involves processing a portion of the data locally using the computational resources of the robot, while offloading the remaining data MEC via the RIS.

a) Local computation model: For k-th robot, let D_k, d_k, c_k and f_k denote the total number of bits in the computing task awaiting processing, the number of bits offloaded to the edge, the number of CPU cycles required per bit, and the CPU frequency, respectively. Therefore, the local computing latency for k-th robot can be expressed as $T_k^l = (D_k - d_k)c_k/f_k$.

b) Edge computation model: The computational resources assigned to k-th robot are denoted as f_k^e, where $\sum_{k=1}^{K} f_k^e \leq f_{\text{total}}^e$ representing the total processing capacity of MEC. It is assumed that edge computing for k-th robot commences upon the reception of all d_k bits offloaded to the BS. The latency of entire edge computing process for k-th robot mainly consists of $T_{k,u}$, $T_{k,c}$ and $T_{k,d}$, which can be expressed as:

$$T_k^e = T_{k,u} + T_{k,c} + T_{k,d} \tag{5.9}$$

where $T_{k,u}$ is the task offloading latency, $T_{k,c}$ is the MEC computing latency and $T_{k,d}$ is the result feedback latency. It is important to know that size of feedback data is small, and therefore, the feedback latency $T_{k,d}$ can be considered negligible [7]. As a result, the edge computing latency can be written as $T_k^e = T_{k,u} + T_{k,c} = d_k/R_k + d_k c_k/f_k^e$.

In this paper, we consider the simultaneous execution of local and edge computing. Thus, the total latency of k-th robot can be denoted as:

$$T_k = \begin{cases} T_k^l, & \mathrm{T}_k^l > T_k^e \\ T_k^e, & \text{Otherwise} \end{cases}, \forall k \in \mathscr{K} \tag{5.10}$$

5.2.4 Problem Formulation

In the RIS-assisted ISCC system for the IoRT scenario, the performance is primarily determined by the following three indicators: the latency of computing T_k, the transmission rate of communication R_k, and the accuracy of sensing β_k. According to [24], the QoS of k-th robot can be denoted as:

$$\mathrm{QoS}_k = \mathscr{F}_1(T_k)\,\mathscr{F}_2(R_k)\,\beta_k \tag{5.11}$$

where $\mathscr{F}_1(x) = \frac{x_{\max} - x}{x_{\max} - x_{\min}}$ and $\mathscr{F}_2(x) = \frac{x - x_{\min}}{x_{\max} - x_{\min}}$ are two normalization method. From Eq. (5.11), we can observe that lower computing latency can result in higher value of $\mathscr{F}_1(T_k)$, thereby improving the QoS of the IoRT system. As the same, higher transmission rate and sensing accuracy can also improve QoS of the RIS-enable ISCC system.

In practical scenarios, it is crucial to fully consider the hardware conditions and deployment environment of the system. However, this paper primarily focuses on the theoretical aspects and simulation results, and does not delve into the practical deployment considerations. In this paper, our objective is to enhance the QoS for robots in RIS-assisted ISCC network, aiming to meet the high demands of robotic application in terms of real-time communication and precise environment interaction. Specifically, we aim to jointly optimize the communication precoding matrix $\mathbf{W} = \{\mathbf{w}_k, \forall k \in \mathscr{K}\}$, the sensing beamforming matrix $\mathbf{W}_s = \left\{\mathbf{w}_{s,k}, \forall k \in \mathscr{K}\right\}$, the phase shift matrix $\boldsymbol{\Theta} = \mathrm{diag}\left\{e^{j\theta_1}, \cdots, e^{j\theta_N}\right\} \in \mathbb{C}^{N\times N}$, the offloading volume $\mathbf{d} = [d_1, \cdots, d_K]^{\mathrm{T}}$, and the edge computational resource allocation $\mathbf{f} = \left[f_1^e, \cdots, f_K^e\right]^{\mathrm{T}}$.

Thus, the optimization problem can be formulated as:

$$\begin{aligned}
\textbf{(P0)} \quad & \max_{\mathbf{W},\mathbf{W}_s,\boldsymbol{\Theta},\mathbf{d},\mathbf{f}} \quad \sum_{k=1}^{K} \lambda_k \mathrm{QoS}_k && (12)\\
\text{s.t.} \quad & \mathrm{Tr}\left[\mathbb{E}\left[\mathbf{x}_k \mathbf{x}_k^{\mathrm{H}}\right]\right] \leq P_k, \forall k \in \mathscr{K} && (5.12a)\\
& \beta_k \geq \beta_{th}, \forall k \in \mathscr{K} && (5.12b)\\
& 0 < \theta_n \leq 2\pi, \forall n \in \mathscr{N} && (5.12c)\\
& \sum_{k\in\mathscr{K}} f_k^e \leq f_{\mathrm{total}}^e && (5.12d)\\
& d_k \in \{0, 1, \ldots, D_k\}, \forall k \in \mathscr{K} && (5.12e)\\
& f_k^e \geq 0, \forall k \in \mathscr{K} && (5.12f)
\end{aligned}$$

where λ_k is the weight of k-th robot, β_{th} is the sensing threshold. However, **(P0)** is a multi-variable non-convex problem with a high degree of coupling between variables, solving it remains a significant challenge. Therefore, we adopt a block coordinate descent (BCD) method, decoupled the complex problem into several sub-problems.

5.2.5 Problem Decomposition

In the RIS-enabled ISCC system in IoRT scenarios, the QoS optimization problem can be divided into two successive stages by employing BCD. In the first stage, given the passive and active beamforming matrix $\{\mathbf{W}, \mathbf{W}_s, \boldsymbol{\Theta}\}$, the offloading volume $\mathbf{d}$ and edge computational resource allocation $\mathbf{f}$ are jointly optimized, with the constraints (12d), (12c) and (12e). In the second stages, given the $\{\mathbf{v}, \mathbf{f}\}$, the passive and active beamforming matrix are optimized with constraints (12a), (12b) and (12c). In alignment with the two stages, the non-convex problem **(P0)** is segmented into two sub-problems, namely minimizing the computing latency T_k in stage-I and maximizing the communication transmission rate R_k and sensing accuracy β_k in stage-II. The two sub-problems can be expressed as:

Problem 1:*Minimization computing latency of Stage-I*

$$\textbf{(P1)} \quad \max_{\mathbf{d},\mathbf{f}} \quad \sum_{k\in\mathcal{K}} \lambda_k \mathscr{F}_1(T_k) \tag{13}$$

$$\text{s.t.} \quad \text{(12d), (12e), (12f)} \tag{5.13a}$$

Problem 2:*Maximization transmission rate and sensing accuracy of Stage-II*

$$\textbf{(P2)} \quad \max_{\mathbf{W},\mathbf{W}_s,\mathbf{\Theta}} \quad \sum_{k\in\mathcal{K}} \mathscr{F}_2(R_k)\,\beta_k \tag{14}$$

$$\text{s.t.} \quad \text{(12a), (12b), (12c)} \tag{5.14a}$$

Thus, by this way, the complex problem **(P0)** is effectively divided into two more manageable sub-problems, **(P1)** and **(P2)**, which are successfully addressed in Section IV.

5.3 QoS Optimization in RIS-assisted ISCC system in IoRT scenarios

5.3.1 Minimization Computing Latency at Stage-I

In this section, a partial offloading approach is proposed to minimize the computing latency. From **(P1)**, it is evident that the computing latency T_k^l and T_k^e exhibit opposing responses to increase in offloading volume d_k. Specifically, T_k^l decreases while T_k^e increases as d_k grows. Therefore, to achieve the minimum value of T_k, an alternating optimization method is employed. First, given an initial value of $\mathbf{f}$, we optimize $\mathbf{d}$ to balance T_k^l and T_k^e according to Eq. (5.10). Then, with the optimized $\mathbf{d}$, we update and optimize $\mathbf{f}$. This process is repeated iteratively until convergence is achieved, ensuring that both $\mathbf{f}$ and $\mathbf{d}$ are optimally adjusted to minimize the computing latency. The optimal value of d_k can be calculated as:

$$d_k^* = \frac{D_k R_k c_k f_k^e}{f_k^e f_k^l + R_k c_k (f_k^e + f_k^l)} \tag{5.15}$$

where d_k^* denotes the optimal value of offloading volume for k-th robot. Note that d_k^* must satisfy the constraint (12e). If d_k^* meet the constraint, then the boundary of d_k should chosen as the optimal offloading strategy, which equals to a binary offloading strategy.

Following obtaining d_k^* for each robot, the **(P0)** can be transform into:

$$\textbf{(P3)} \quad \min_{\mathbf{f}} \quad \sum_{k\in\mathscr{K}} \lambda_k \frac{D_k c_k (f_k^e + R_k c_k)}{f_k^e f_k^l + R_k c_k (f_k^e + f_k^l)} \tag{16}$$

$$\text{s.t.} \quad \text{(12d), (12f)} \tag{5.16a}$$

The problem **(P3)** is convex and satisfies the Karush-Kuhn-Tucker (KKT) condition. Therefore, the Lagrangian function can be written as:

$$\begin{aligned} \mathscr{L}(\mathbf{f},\mu) = \sum_{k\in\mathscr{K}} \lambda_k \frac{D_k c_k (f_k^e + R_k c_k)}{f_k^e f_k^l + R_k c_k (f_k^e + f_k^l)} \\ + \mu\Big(\sum_{k\in\mathscr{K}} f_k^e - f_{\text{total}}^e\Big) \end{aligned} \tag{5.17}$$

where μ is the Lagrange multiplier. The optimal f_k^{e*} can be obtained when:

$$\nabla_{f_k^e} \mathscr{L} = -\frac{D_k R_k^2 c_k^3 \lambda_k}{\left(R_k c_k f_k^l + R_k c_k f_k^{e*} + f_k^l f_k^{e*}\right)^2} + \mu^* = 0 \tag{5.18a}$$

$$\mu\Big(\sum_{k\in\mathscr{K}} f_k^e - f_{\text{total}}^e\Big) = 0 \tag{5.18b}$$

$$\sum_{k\in\mathscr{K}} f_k^e - f_{\text{total}}^e \leq 0 \tag{5.18c}$$

$$\mu \geq 0, f_k^e \geq 0 \tag{5.18d}$$

When μ is given, we can obtain the optimal f_e^k by solving:

$$\max_{f_e^k \in \left(0, f_{total}^e\right]} \quad \mu^* \Big(\sum_{k\in\mathscr{K}} f_k^e - f_{\text{total}}^e\Big) \tag{5.19}$$

which can be solved by binary search method. The overall process is summarized at Algorithm I. The complexity is mainly influenced by the binary method, which can be denoted as $\mathscr{O}(\log n)$.

Algorithm 8 Joint optimization of offloading volume and edge computing resource allocation

1: **Input:** Beamforming matrices $\mathbf{\Theta}$, $\mathbf{W}$, $\mathbf{W}_s$
2: **Output:** Optimal edge computing resource allocation $\mathbf{f} = \left\{f_1^{e*}, \cdots, f_K^{e*}\right\}^{\mathrm{T}}$, offloading volume $\mathbf{d} = \{d_1^*, \cdots, d_K^*\}^{\mathrm{T}}$
3: **Initialization:** $t = 0$, $\mathbf{f}^0$, $\mathbf{d}^0$, maximum iterations $t_{\max}$
4: Calculate d_k^* using Eq. (5.15) for all $k \in \mathscr{K}$
5: **repeat**
6: Determine μ and update $f_e^{(t+1)}$ via binary method
7: $t \leftarrow t+1$
8: **until** $t = t_{\max}$ or $\left|T_k^t - T_k^{t-1}\right| < \varepsilon$
9: **Return:** Optimal edge computing resource allocation $\mathbf{f} = \left\{f_1^{e*}, \cdots, f_K^{e*}\right\}^{\mathrm{T}}$ and offloading volume $\mathbf{d} = \{d_1^*, \cdots, d_K^*\}^{\mathrm{T}}$

5.3.2 Maximization Transmission Rate and Sensing Accuracy at Stage-II

This section introduces an optimization framework to solve problem **(P2)**, where objective function conversion and Alternative Optimization (AO) methods are applied. Given $\{\mathbf{f}, \mathbf{d}\}$, we first focus on enhance the communication performance with fixed $\mathbf{W}_s$, which can be formulated as:

$$\textbf{(P4)} \quad \max_{\mathbf{W},\mathbf{\Theta}} \quad \sum_{k \in \mathscr{K}} \mathscr{F}_2(R_k) \tag{20}$$

$$\text{s.t.} \quad \text{(12a), (12c)} \tag{5.20a}$$

However, due to the coupling between $\mathbf{W}$ and $\mathbf{\Theta}$, problem **(P4)** remains non-convex. Consequently, an AO method is employed to address this problem. In AO approach, we consider $\mathbf{W}$ as a fixed parameter and find $\mathbf{\Theta}$ to optimize the objective function. Subsequently, with $\mathbf{\Theta}$ fixed, we determine the optimal $\mathbf{W}$ to enhance the transmission rate. This iterative process continues until convergence of the objective function is achieved. For simplicity, the phase shifts ϕ_n of RIS are selected from a predefined set $\mathbf{\Theta}_b = \left\{0, \frac{2\pi}{2^b}, \ldots, \frac{2\pi}{2^b}\left(2^b - 1\right)\right\}$. Specifically, in this paper, $b = 1$.

1) RIS phase shift optimization: Given the communication precoding matrix $\mathbf{W}$, the problem **(P4)** can be rewritten as:

$$\textbf{(P5)} \quad \max_{\boldsymbol{\Theta}} \quad \sum_{k\in\mathscr{K}} \frac{\left\|\left(\mathbf{G}\boldsymbol{\Theta}\mathbf{H}_{r,k}+\mathbf{H}_{b,k}\right)\mathbf{w}_k\right\|^2}{\sigma_k^2+\sum_{j\neq k}\left\|\left(\mathbf{G}\boldsymbol{\Theta}\mathbf{H}_{r,k}+\mathbf{H}_{b,k}\right)\mathbf{w}_j\right\|^2} \tag{21}$$

$$\text{s.t.} \quad \text{(12a), (12c)} \tag{5.21a}$$

To tackle this problem, we apply Fractional Program Quadratic Transform method [67] to the objective function of **(P5)** and get equivalent optimization problem **P(5.1)** as follows:

$$\textbf{(P5.1)} \quad \max_{\boldsymbol{\Theta},y_k} \quad \log_2\left(2y_k\sqrt{A_k(\boldsymbol{\Theta})}-y_k^2B_k(\boldsymbol{\Theta})\right) \tag{22}$$

$$\text{s.t.} \quad \theta_n\in(0,2\pi],n\in\mathscr{N} \tag{5.22a}$$

$$y_k\in\mathbb{R},k\in\mathscr{K} \tag{5.22b}$$

where

$$A_k(\boldsymbol{\Theta})=\sum_{k\in\mathscr{K}}\left|\left(\mathbf{G}\boldsymbol{\Theta}\mathbf{H}_{r,k}+\mathbf{H}_{b,k}\right)\mathbf{w}_k\right|^2+\sigma_k^2 \tag{5.23}$$

$$B_k(\boldsymbol{\Theta})=\sum_{j\neq k}\left|\left(\mathbf{G}\boldsymbol{\Theta}\mathbf{H}_{r,k}+\mathbf{H}_{b,k}\right)\mathbf{w}_j\right|^2+\sigma_k^2 \tag{5.24}$$

When the phase shift matrix $\boldsymbol{\Theta}$ is fixed, the optimal y_k can be obtained as:

$$y_k^*=\frac{\sqrt{A_k(\boldsymbol{\Theta})}}{B_k(\boldsymbol{\Theta})} \tag{5.25}$$

Then, it is found that optimizing $\boldsymbol{\Theta}$ for given y_k is a convex problem. Therefore, the problem **(P5.1)** can be effectively solved by alternating optimization over $\boldsymbol{\Theta}$ and over the auxiliary variables $\{y_k\}_{k=1}^K$.

2) Communication precoding matrix optimization: Given the phase shift matrix $\boldsymbol{\Theta}$ of RIS and employing the Quadratic Transform method, the problem **(P4)** can be transformed into:

$$\textbf{(P6)} \quad \max_{\mathbf{W},\mathbf{y}_1} \quad \sum_{k\in\mathscr{K}} f\left(\mathbf{W},\mathbf{y}_1\right) \tag{26}$$

$$\text{s.t.} \quad \text{Tr}\left[\mathbb{E}\left[\mathbf{x}_k\mathbf{x}_k^{\mathrm{H}}\right]\right]\leq P_k,\forall k\in\mathscr{K} \tag{5.26a}$$

$$y_{1,k}\in\mathbb{R},\forall k\in\mathscr{K} \tag{5.26b}$$

Algorithm 9 AO optimization for communication optimization

1: **Input:** $\mathbf{H}_k$, δ, ε
2: **Output:** $\mathbf{W}$, $\boldsymbol{\Theta}$
3: **Initialization:** $t = 0$, $\boldsymbol{\Theta}_0$, $\mathbf{W}_0$, maximum iterations $t_{\max}$
4: **repeat**
5: Calculate $\boldsymbol{\Theta}_t$ by solving **(P5)** with fixed $\mathbf{W}_{t-1}$
6: Calculate $\mathbf{W}_t$ by solving **(P6)** with fixed $\boldsymbol{\Theta}_{t-1}$
7: $t \leftarrow t+1$
8: **until** $t = t_{\max}$ or $|\boldsymbol{\Theta}_{t+1} - \boldsymbol{\Theta}_t| < \varepsilon$ and $|\mathbf{W}_{t+1} - \mathbf{W}_t| < \varepsilon$
9: **Return:** $\mathbf{W}$, $\boldsymbol{\Theta}$

where $\mathbf{y}_1 = \left\{y_{1,1}, \ldots, y_{1,k}\right\}$ is a auxiliary vector. The formulation of $f(\mathbf{W}, \mathbf{y}_1)$ can be expressed as:

$$\begin{aligned} f(\mathbf{W}, \mathbf{y}_1) = \sum_{k \in \mathscr{K}} \log_2 \Bigg(& 2y_{1,k}\sqrt{|\mathbf{H}_k \mathbf{w}_k|^2} \\ & -y_{1,k}^2 \left(\sum_{j \neq k} \left|\mathbf{H}_k \mathbf{w}_j\right|^2 + \delta_k^2 \right) + 1 \Bigg) \end{aligned} \tag{5.27}$$

Given the fixed $\mathbf{W}$, the optimal value of $\mathbf{y}_1$ can be calculated as:

$$y_{1,k}^* = \sum_{k \in \mathscr{K}} \frac{\sqrt{\left|\left(\mathbf{H}_{r,k} \boldsymbol{\Theta} \mathbf{G} + \mathbf{H}_{b,k}\right) \mathbf{w}_k\right|^2}}{\sigma_k^2 + \sum_{j \neq k} \left|\left(\mathbf{H}_k \boldsymbol{\Theta} \mathbf{G} + \mathbf{H}_{b,k}\right) \mathbf{w}_j\right|^2} \tag{5.28}$$

It is important to note that after obtaining optimal $\mathbf{y}_1$, the optimization problem of $\mathbf{W}$ is convex, which can be solved by convex optimization method.

By implementing the AO method and iteratively updating $\mathbf{W}$ and $\boldsymbol{\Theta}$, we can obtain approximate optimal solutions for $\mathbf{W}$ and $\boldsymbol{\Theta}$. The procedure is encapsulated in Algorithm 2.

Given $\{\mathbf{W}, \boldsymbol{\Theta}\}$, we then focus on optimizing $\mathbf{W}_s$ of robots to enhance the sensing accuracy. The problem **(P2)** can be rewritten as:

$$\textbf{(P7)} \quad \max_{\mathbf{W}_s} \quad \sum_{k \in \mathscr{K}} \frac{\left|\mathbf{w}_{s,k} \alpha_k \mathbf{a}_k^R(\theta_k) \mathbf{a}_k^T(\theta_k) \mathbf{x}_k\right|^2}{\left|\mathbf{w}_{s,k} \sum_{j=1, j \neq k}^{K} \mathbf{H}_{k,j} \mathbf{x}_j + \eta_k\right|^2} \tag{29}$$

$$\text{s.t.} \quad \beta_k \geq \beta_{th}, \forall k \in \mathscr{K} \tag{5.29a}$$

Due to signal interference among multiple robots, we employ a codebook-based approach to enhance the perceptual accuracy of the robots. Let us consider a codebook $\mathscr{C}_k = \left\{\mathbf{c}_{1,k}, \ldots, \mathbf{c}_{k,l}, \ldots, \mathbf{c}_{k,L}\right\}$, with each codeword $\mathbf{c}_{k,l} \in \mathbb{C}^{M \times 1}$ denotes a specific sensing beamforming matrix of k-th robot [53]. Without loss of generality, we assume that each

Algorithm 10 Optimization of Communication Strategy

Input: $\mathscr{C}_k$, $\mathbf{W}$, $\mathbf{\Theta}$
Output: $\mathbf{W}_s$
Initialization: $l=0$, $\mathbf{W}_s^0$, maximum iterations L, $\beta_k^*=0$
repeat
    Calculate β_k^l by scanning $\mathscr{C}_k$ according to **(P8)**
    if $\beta_k^l \geq \beta_k^*$ **then**
        $\beta_k^* \leftarrow \beta_k^l$
    end if
    $l \leftarrow l+1$
until $l=L$
Return: $\mathbf{c}^*$

codeword in the codebook exhibits a degree of spatial directivity, meaning that the resulting sensing beamforming matrix is only capable of maximizing when aligned with a specific (narrow) angle. Therefore, by iteratively scanning all the codewords $\mathbf{c}_{k,l} \in \mathbf{C}_k$, the k-th robot is able to scan the space with a given spatial resolution and detect target objects using wireless signals. By employing a predefined set of codewords, each representing a specific spatial directivity, we can quickly determine the optimal configuration through iterative scanning. This approach ensures that the robots can efficiently and accurately detect target objects, even in dynamic and complex environments. The problem **(P7)** can be transformed into:

$$\textbf{(P8)} \quad \max_{\mathbf{W}_s} \quad \sum_{k\in\mathscr{K}} \beta_k(\mathbf{w}_{s,k}) \tag{30}$$

$$\text{s.t.} \quad \beta_k \geq \beta_{th}, \forall k \in \mathscr{K} \tag{5.30a}$$

$$\mathbf{w}_{s,k} \in \mathscr{C}_k, \forall k \in \mathscr{K} \tag{5.30b}$$

By iterating through all the codewords, the angle corresponding to the codeword with the highest received signal strength is considered to be the direction where the target object is located. The overall process is summarized as algorithm 3.

5.4 Simulation Results

In this section, we conduct extensive simulation experiments to validate the performance of our proposed RIS-enabled ISCC system in IoRT scenarios. In the RIS-enabled ISCC system for IoRT scenarios, the QoS performance metrics are mainly influenced by transmission rate, the computing latency, and sensing accuracy. Therefore, we investigate the affect of system settings to QoS performance metrics, including the quantity of robots K, the quantity of

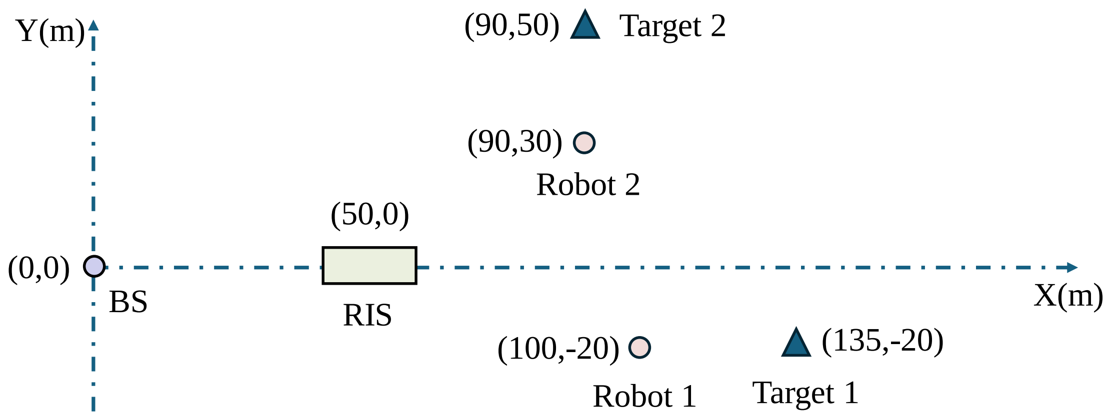

Fig. 5.2 Simulation scenario for RIS-assisted ISCC in IoRT.

RIS element N, the edge computing capability f^{e}_{total}. To deliver a thorough assessment, we choose several benchmark schemes compared with our proposed method.

- `Proposed Method`: This legend denotes the proposed joint optimization approach for the RIS-assisted ISCC in IoRT scenarios, in which the transmission matrix, the offloading volume, the edge computing resource allocation, the sensing beamforming matrix of robot and the phase shift of RIS are jointly optimized.

- `No-Passive`: This legend means that the simplified optimization approach for the RIS-assisted ISCC in IoRT scenarios, in which the passive beamforming matrix of RIS is random generated, while other optimization methods remain unchanged.

- `No-Offloading`: In this benchmark, robots can not offloading tasks to MEC and only can finish computational task in local, while other optimization parts is same.

- `No-RIS`: To validate the impact of RIS on enhancing the wireless transmission rate in ISCC systems, in this comparative optimization scheme, we have removed the RIS, and communication between the robots and the BS is conducted solely via LoS links.

- `No-Active`: In this optimization benchmark, we randomly generate the communication beamforming matrix, aiming to investigate the impact of active beamforming.

Unless specified differently, the simulation parameters are as follows. As illustrated in Fig. 5.2, the BS with the number antennas $L = 4$ and RIS with the number of element $N = 32$ are located at [0, 0] and [50, 0],respectively. We assume that two robots with the number of antenna $M = 2$ are located at [90, 30] and [100, -20], with corresponding target at [90, 50] and [135,-20], respectively. The transmit power of each robot is 0 dbW, the

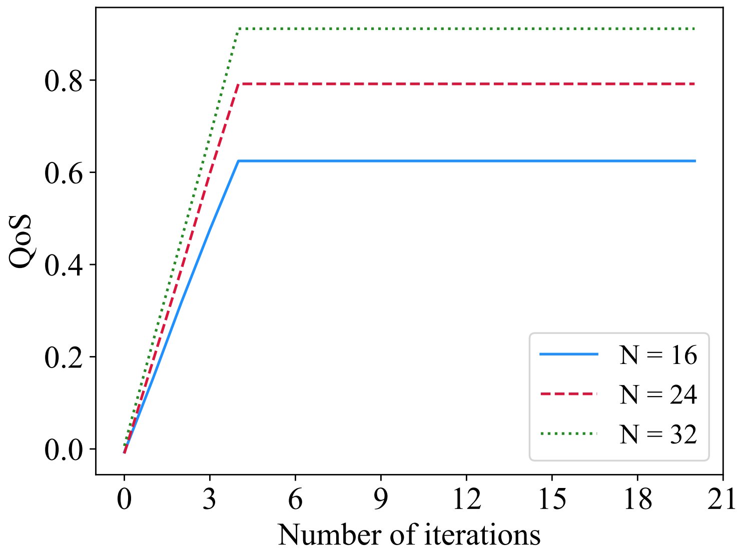

Fig. 5.3 The convergence of the proposed algorithm via different RIS elements N.

available bandwidth $B = 1$GHz. The CPU cycles required for processing each bit set as $c_k = 500$ cycle/bit, and the total computing resource of MEC is $f^e_{total} = 5 \times 10^9$cycle/s.

Fig. 5.3 depicts the convergence of the `Proposed Method` with respect to the number of iterations for three different RIS element numbers, specifically $N = 16$, $N = 24$, and $N = 32$. It is evident from the Fig. 5.3 that the QoS metric approaches its peak rapidly, indicating that the system achieves optimal performance within a few iterations. Additionally, the convergence profiles for the various system sizes show a high degree of overlap, suggesting that the QoS metric is robust to changes in the system size within the range considered.

Fig. 5.4 shows the variability in the performance of `Proposed Method` by displaying the average QoS for ten different channel realizations, each associated with distinct computational tasks, indexed from 1 to 10. For every channel realization, optimization variables were initialized 100 times at random, with the solutions calculated using the prescribed algorithm. The figure delineates the span between the Max and Min average QoS achieved across these iterations. Max corresponds to the least favorable outcome, whereas Min is indicative of an approximation to the optimal QoS. The pattern observed in the Fig. 5.4 suggests that the spread between Max and Min is consistent across different realizations, pointing to a stable performance of the algorithm under varied initial conditions.

Fig. 5.5 illustrates the impact of the number of robots K on both the average QoS and computing latency in the considered RIS-assisted ISCC system. In Fig. 5(a), as K increases, there is a notable decrease in average QoS for all strategies, which signifies a decline in service quality with more robots in the network. Similarly, Fig. 5(b) reveals that the latency

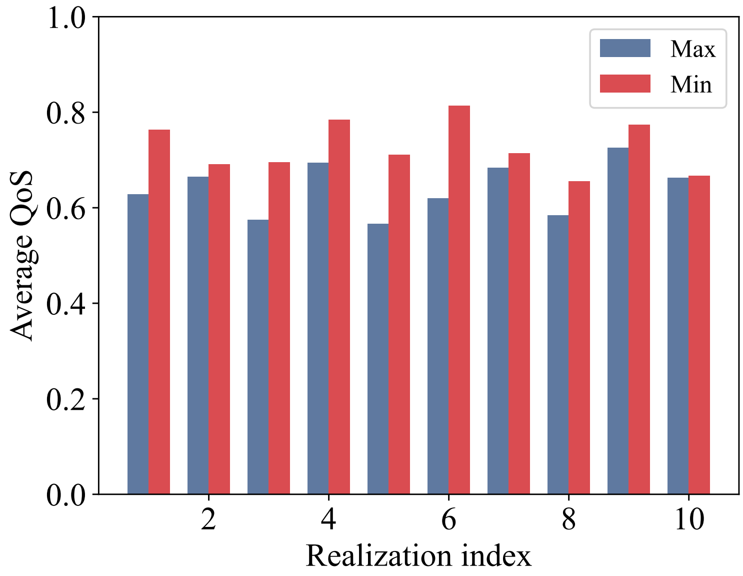

Fig. 5.4 Simulation results showing the maximum and minimum latency values across the realization index.

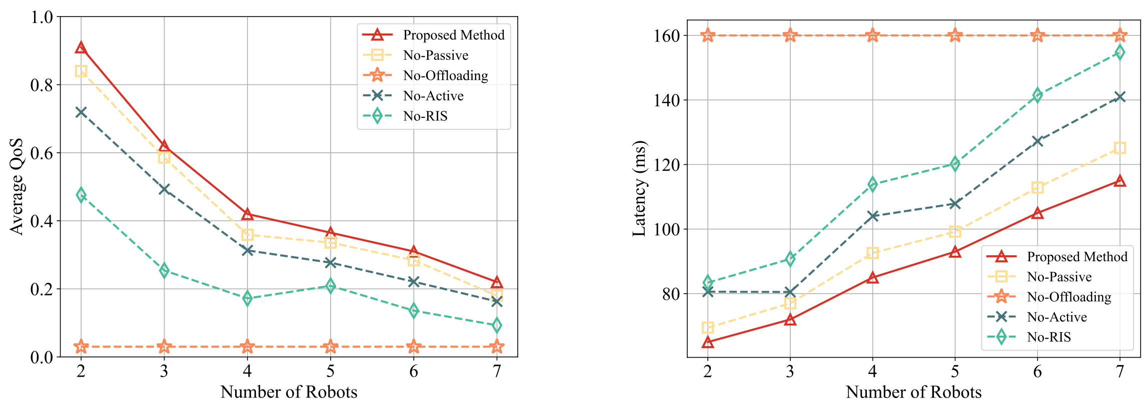

(a) Average QoS

(b) Average latency

Fig. 5.5 The effect of the number of robots K on the average QoS and average latency in the proposed RIS-assisted ISCC for IoRT scenarios.

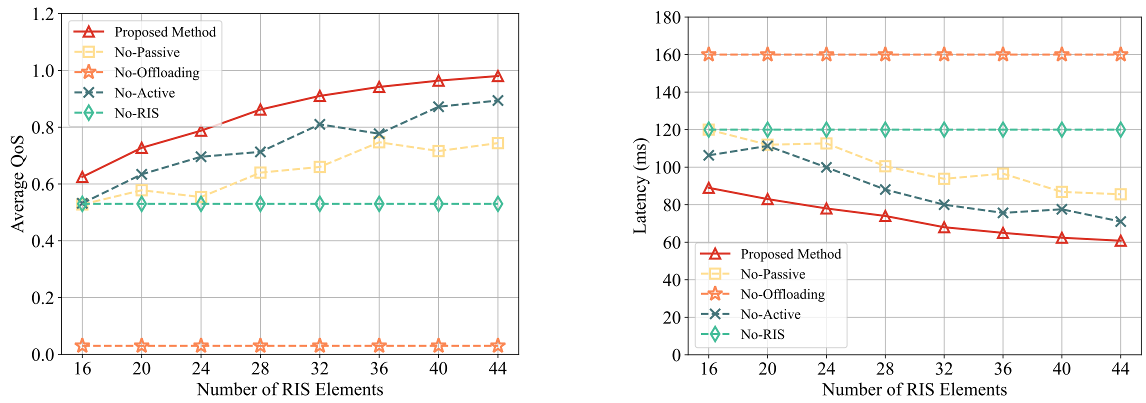

(a) Average QoS (b) Average latency

Fig. 5.6 The effect of the number of RIS elements N on the average QoS and average latency in the proposed RIS-assisted ISCC for IoRT scenarios.

tends to increase with the number of robots for all methods. This could be attributed to the additional computational and communication load that more robots introduce to the system. The `Proposed Method` outperforms the other strategies, as it maintains the highest average QoS and the lowest latency across the range of K, emphasizing the efficiency of the proposed system. However, for both metrics, the `No-RIS` scheme consistently demonstrates the least favorable performance, underscoring the significance of RIS in enhancing system performance in IoRT applications. Fig. 6 analyzes the relationship between the number of RIS elements N and the system performance in terms of average QoS and latency within an IoRT context employing an RIS-assisted ISCC framework. From Fig. 6(a), we can deduce that the average QoS improves as N increases for the `Proposed Method`, which contrasts with other methods where QoS either increases at a slower rate or plateaus. In Fig. 6(b), the latency trends downward for the proposed method with an increase in N, indicating enhanced performance, whereas the other schemes exhibit either a slower reduction in latency or an initial decrease followed by stabilization. The `No-RIS` strategy shows a flat trend, reflecting no improvement with additional RIS elements, since it does not benefit from the RIS's reflective capabilities. These observations collectively emphasize the effectiveness of RIS elements in improving QoS and reducing latency in IoRT applications, with the `Proposed Method` demonstrating superior performance compared to other strategies under investigation.

Fig. 5.7 illustrates the correlation between the edge computing resources f_{total} and both the average QoS and latency within the framework of a proposed RIS-assisted ISCC for IoRT scenarios. In Fig. 7(a), the graph indicates an enhancement in average QoS proportional to the increase in computing resources for the proposed method, whereas the other schemes exhibit a more modest growth or saturation in QoS. Concurrently, Fig. 7(b) demonstrates a decrease in latency as computing resources are augmented, with the proposed method again showing superior performance with the lowest latency across the resource spectrum. The `No-RIS` approach consistently manifests higher latency and lower QoS, unaffected by the variation in edge computing resources, thereby highlighting the integral role of RIS elements in augmenting the IoRT network's efficiency. These observations reinforce the premise that greater computing resources bolster the IoRT system's capability, as reflected in the QoS and latency metrics, particularly when leveraging RIS technology.

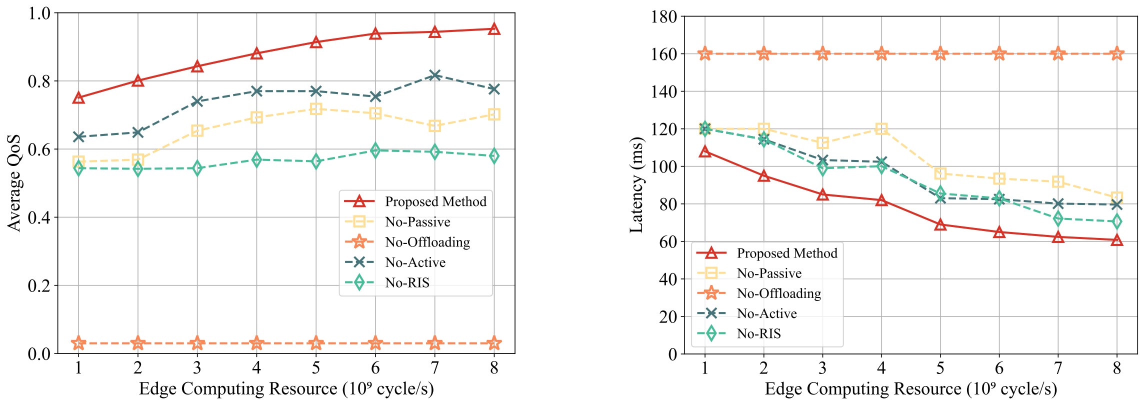

(a) Average QoS (b) Average latency

Fig. 5.7 The effect of the number of edge computing resource f^e_{total} on the average QoS and average latency in the proposed RIS-assisted ISCC for IoRT scenarios.

Fig. 5.8 shows the performance of the RIS-enabled ISCC system in reducing the bit error rate (BER) of uplink transmission from the robot to the MEC. For binary phase shift keying (BPSK) signaling, the general BER expression is considered. The average BER for the uplink can be obtained as follows [49]:

$$\mathrm{BER}_k = \frac{1}{\pi}\int_0^{\frac{\pi}{2}} R_k\left(-\frac{\sin\left(\frac{\pi}{2}\right)}{\sin^2\theta}\right)\mathrm{d}\theta \tag{5.31}$$

The upper bound for the average BER with BPSK can be expressed as:

$$\mathrm{BER}_k \leq \frac{\exp\left(\frac{-\frac{N^2 P_{loss}\pi^2\left(-k^2/(K+1)\right)p_k}{16(K+1)^2 N_0}}{1+\frac{NP_{loss}\left(16(K+1)^2-\pi^2\left(-k^2/(K+1)\right)\right)p_k}{8(K+1)^2 N_0}}\right)}{2\sqrt{1+\frac{NP_{loss}\left(16(K+1)^2-\pi^2\left(-k^2/(K+1)\right)\right)p_k}{8(K+1)^2 N_0}}} \tag{5.32}$$

where K is the Rician factor, P_{loss} is the path loss from k-th robot to BS.

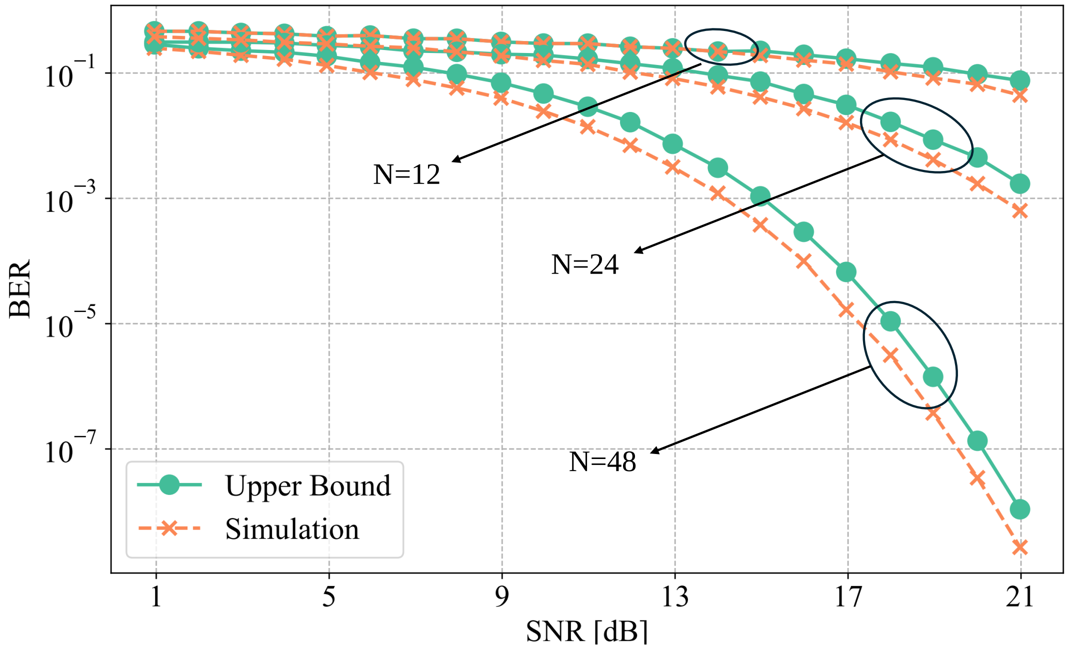

Fig. 5.8 BER performance of RIS-enabled ISCC system for IoRT scenarios.

Fig. 5.8 shows that as the SNR increases, the BER significantly decreases, indicating that better signal quality reduces the error rate. Additionally, increasing the number of reflecting elements substantially improves the system's BER performance. This significant reduction in BER with more RIS elements highlights the enhanced reliability and communication quality of the proposed system, addressing concerns about reliability as a key performance metric.

Fig. 5.9 demonstrates the effect of sensing SNR on the average QoS of the system. As sensing SNR increases, the average QoS improves significantly for all schemes, which indicates that higher sensing SNR enhances system performance and reduces the impact of blockages on the optimization process. Compared to other schemes, the `Proposed Method` outperforms other schemes regarding the average QoS, confirming our proposed method's effectiveness. Moreover, the QoS initially overgrows with increasing sensing SNR but slows down after reaching a certain threshold, likely due to diminishing returns as the system approaches its optimal performance limits.

5.5 Conclusion

This paper introduced a novel RIS-enabled ISCC system specifically designed for IoRT scenarios to tackle the pressing challenges of computational latency, communication rate, and sensing accuracy. We formulated an optimization problem aimed at enhancing the

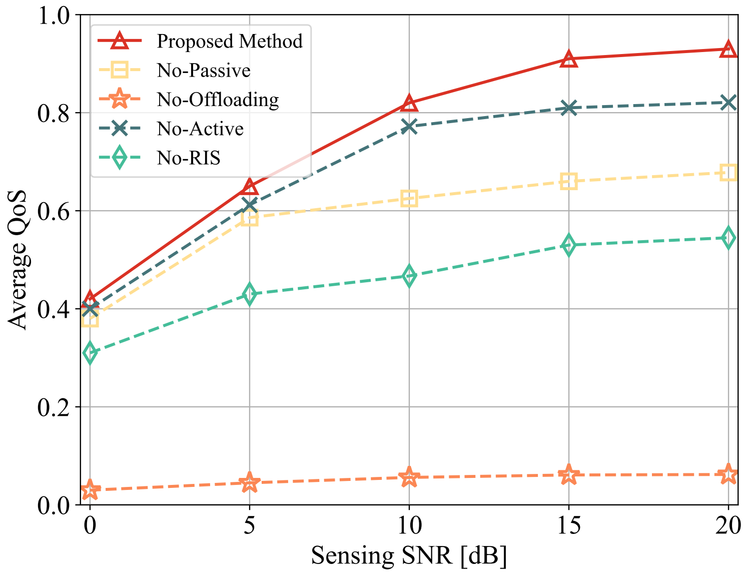

Fig. 5.9 The effect of the sensing SNR on the average QoS.

overall performance of IoRT systems and proposed a BCD-based algorithm to effectively decompose this non-convex problem into manageable sub-problems. The first sub-problem focused on minimizing computing latency by optimizing edge computing resource allocation, while the second aimed to maximize communication speed and improve sensing precision through innovative beamforming techniques. Our proposed solution leveraged AO and objective function conversion techniques to address the complexities of the optimization tasks. Extensive simulations validated the effectiveness of our approach, demonstrating significant enhancements in QoS and reductions in system latency. These improvements not only underscore the potential of RIS in overcoming traditional barriers in wireless communication and computation but also highlight the pivotal role of integrated ISCC systems in advancing IoRT technologies. The significant reduction in latency and the improvement in the reliability and efficiency of robotic operations in complex environments, as evidenced by our simulations, illustrate the transformative potential of integrating RIS into IoRT. Additionally, the proposed RIS-enabled ISCC system is designed to be scalable and can be expanded to large-scale applications. However, the challenges associated with such expansion, such as interference management and computational overhead, will be addressed in future work.

Chapter 6

Conclusions and Future Directions

In the first task, we focus on optimizing the deployment of multi-RIS in a multi-user communication scenario to maximize the achievable rate through a heuristic approach based on adaptive optimization. Our proposed method enables dynamic adjustment of the RIS's phase configuration, resulting in significant improvements in achievable rate compared to conventional static schemes. Simulation results illustrate that the intelligent deployment of multiple RISs allows precise focusing of signal transmissions towards users, thus enhancing overall system efficiency. Future work will explore the combination of multi-hop signal reflections to improve coverage in broader areas and create a highly adaptive wireless communication environment.

In the second task, we target large-scale deployment of RISs to extend the coverage of outdoor wireless networks. The key idea is to employ cost-aware optimization, taking into account both coverage probability and deployment costs. Our approach involves using a cell decomposition-based coverage model and an optimization algorithm that incorporates both greedy and adaptive methodologies to ensure that RISs are optimally placed to achieve desired coverage levels within network constraints. The results indicate that our method provides a better balance between maximizing coverage and minimizing deployment costs compared to conventional methods. In future research, we will investigate coverage enhancements considering three-dimensional positioning of RISs, as well as user mobility, to further refine coverage estimates and solutions.

The third task addresses the optimization of resource allocation in RIS-assisted IoT networks, with a focus on reducing power consumption while maintaining a target coverage rate. We propose a dual-objective optimization that simultaneously solves for RIS-device association and phase shift configuration. A heuristic approach is employed to ensure optimal resource usage, while a relaxation-based phase optimization is used to minimize the power requirements. Our simulation findings show that the proposed approach effectively reduces system power consumption while meeting coverage targets, outperforming existing benchmark methods. Future work will focus on improving the real-time responsiveness of the RIS network through the design of a strategic codebook and more advanced phase adjustment algorithms, thereby better serving the needs of mobile IoT devices.

In the last task, we investigate a multi-RIS-assisted THz communication network for virtual reality (VR) applications in an indoor environment. The main objective is to enhance user Quality of Experience (QoE) while maintaining low latency during interactive VR activities. We tackle this problem by jointly optimizing the RIS beamforming, VR transmission power, and rendering resource allocation. Simulation results indicate that an increase in reflective elements, transmit power, and rendering resources directly contributes to higher achievable rates in the downlink, thus improving QoE. However, adding too many RISs may not yield additional benefits in confined indoor settings and can negatively affect system efficiency. Overall, our proposed multi-RIS-assisted optimization approach is validated as a viable method for enhancing VR experiences, offering superior performance in terms of QoE compared to other reference algorithms.

References

[1] Abari, O., Bharadia, D., Duffield, A., and Katabi, D. (2017). Enabling high-quality untethered virtual reality. In *14th USENIX Symposium on Networked Systems Design and Implementation (NSDI 17)*, pages 531–544.

[2] Abdallah, A., Celik, A., Mansour, M. M., and Eltawil, A. M. (2024). Multi-agent deep reinforcement learning for beam codebook design in ris-aided systems. *IEEE Transactions on Wireless Communications*.

[3] Albanese, A., Devoti, F., Sciancalepore, V., Di Renzo, M., and Costa-Pérez, X. (2022). MARISA: A self-configuring metasurfaces absorption and reflection solution towards 6g. In *IEEE INFOCOM 2022-IEEE Conference on Computer Communications*, pages 250–259. IEEE.

[4] Alexandropoulos, G. C., Shlezinger, N., Alamzadeh, I., Imani, M. F., Zhang, H., and Eldar, Y. C. (2021). Hybrid reconfigurable intelligent metasurfaces: Enabling simultaneous tunable reflections and sensing for 6g wireless communications. *arXiv preprint arXiv:2104.04690*.

[5] Arun, V. and Balakrishnan, H. (2020a). Rfocus: Beamforming using thousands of passive antennas. In *17th USENIX symposium on networked systems design and implementation (NSDI 20)*, pages 1047–1061.

[6] Arun, V. and Balakrishnan, H. (2020b). Rfocus: Beamforming using thousands of passive antennas. In *17th USENIX symposium on networked systems design and implementation (NSDI 20)*, pages 1047–1061.

[7] Bennis, M., Debbah, M., and Poor, H. V. (2018). Ultrareliable and low-latency wireless communication: Tail, risk, and scale. *Proceedings of the IEEE*, 106(10):1834–1853.

[8] Björnson, E., Özdogan, Ö., and Larsson, E. G. (2020). Reconfigurable intelligent surfaces: Three myths and two critical questions. *IEEE Communications Magazine*, 58(12):90–96.

[9] Chaccour, C., Soorki, M. N., Saad, W., Bennis, M., and Popovski, P. (2020). Risk-based optimization of virtual reality over terahertz reconfigurable intelligent surfaces. In *ICC 2020 - 2020 IEEE International Conference on Communications (ICC)*, pages 1–6.

[10] Chakareski, J., Khan, M., Ropitault, T., and Blandino, S. (2023). Millimeter wave and free-space-optics for future dual-connectivity 6dof mobile multi-user vr streaming. *ACM Transactions on Multimedia Computing, Communications and Applications*, 19(2):1–25.

[11] Chen, M., Liu, A., Liu, W., Ota, K., Dong, M., and N. Xiong, N. (2022). Rdrl: A recurrent deep reinforcement learning scheme for dynamic spectrum access in reconfigurable wireless networks. *IEEE Transactions on Network Science and Engineering*, 9(2):364–376.

[12] Chen, Y., Lu, H., Qin, L., Wu, C., and Chen, C. W. (2023). Streaming 360-degree vr video with statistical qos provisioning in mmwave networks from delay and rate perspectives. *arXiv preprint arXiv:2305.07935*.

[13] Cheng, Y., Du, J., Liu, J., Jin, L., Li, X., and da Costa, D. B. (2024). Nested tensor-based framework for isac assisted by reconfigurable intelligent surface. *IEEE Transactions on Vehicular Technology*, 73(3):4412–4417.

[14] Di Renzo, M., Zappone, A., Debbah, M., Alouini, M.-S., Yuen, C., De Rosny, J., and Tretyakov, S. (2020). Smart radio environments empowered by reconfigurable intelligent surfaces: How it works, state of research, and the road ahead. *IEEE Journal on Selected Areas in Communications*, 38(11):2450–2525.

[15] Dong, J., Ota, K., and Dong, M. (2022). Why vr games sickness? an empirical study of capturing and analyzing vr games head movement dataset. *IEEE MultiMedia*, 29(2):74–82.

[16] Fang, J., Lu, B., Hong, X., and Shi, J. (2024). Double RISs assisted task offloading for noma-mec with action-constrained deep reinforcement learning. *Knowledge-Based Systems*, 284:111307.

[17] Fu, M., Zhou, Y., Shi, Y., and Letaief, K. B. (2021). Reconfigurable intelligent surface empowered downlink non-orthogonal multiple access. *IEEE Transactions on Communications*, 69:3802–3817.

[18] Gao, X., Dai, L., Chen, Z., Wang, Z., and Zhang, Z. (2016). Near-optimal beam selection for beamspace mmwave massive mimo systems. *IEEE Communications Letters*, 20(5):1054–1057.

[19] Guo, H., Liang, Y.-C., Chen, J., and Larsson, E. G. (2020). Weighted sum-rate maximization for reconfigurable intelligent surface aided wireless networks. *IEEE transactions on wireless communications*, 19(5):3064–3076.

[20] He, W., He, D., Ma, X., Chen, X., Fang, Y., and Zhang, W. (2024). Joint user association, resource allocation, and beamforming in RIS-assisted multi-server mec systems. *IEEE Transactions on Wireless Communications*, 23(4):2917–2932.

[21] He, Z.-Q. and Yuan, X. (2019). Cascaded channel estimation for large intelligent metasurface assisted massive MIMO. *IEEE Wireless Communications Letters*, 9(2):210–214.

[22] Hu, G., Wu, Q., Si, J., Xu, K., Li, Z., Cai, Y., and Al-Dhahir, N. (2023). Star-ris-assisted information surveillance over suspicious multihop communications. *IEEE Transactions on Mobile Computing*.

[23] Hu, L., Yang, R., Wu, L., Huang, C., Jiang, Y., Chen, L., and Zhou, X. (2024). RIS-assisted integrated sensing and covert communication design. *IEEE Internet of Things Journal*, 11(9):16505–16516.

[24] Hu, X., Liu, T., and Shu, T. (2022). (k,α)-coverage for ris-aided mmwave directional communication. *IEEE Transactions on Mobile Computing*.

[25] Huang, C., Mo, R., and Yuen, C. (2020). Reconfigurable intelligent surface assisted multiuser miso systems exploiting deep reinforcement learning. *IEEE Journal on Selected Areas in Communications*, 38(8):1839–1850.

[26] Huang, C., Yang, Z., Alexandropoulos, G. C., Xiong, K., Wei, L., Yuen, C., Zhang, Z., and Debbah, M. (2021). Multi-hop RIS-empowered terahertz communications: A DRL-based hybrid beamforming design. *IEEE Journal on Selected Areas in Communications*, 39(6):1663–1677.

[27] Huang, C., Zappone, A., Alexandropoulos, G. C., Debbah, M., and Yuen, C. (2019). Reconfigurable intelligent surfaces for energy efficiency in wireless communication. *IEEE Transactions on Wireless Communications*, 18(8):4157–4170.

[28] Huang, N., Wang, T., Wu, Y., Wu, Q., and Quek, T. Q. S. (2022). Integrated sensing and communication assisted mobile edge computing: An energy-efficient design via intelligent reflecting surface. *IEEE Wireless Communications Letters*, 11(10):2085–2089.

[29] Iepure, B. and Morales, A. W. (2021). A novel tracking algorithm using thermal and optical cameras fused with mmwave radar sensor data. *IEEE Transactions on Consumer Electronics*, 67(4):372–382.

[30] Jiang, F., Abrardo, A., Keykhosravi, K., Wymeersch, H., Dardari, D., and Di Renzo, M. (2023). Two-timescale transmission design and RIS optimization for integrated localization and communications. *IEEE Transactions on Wireless Communications*, 22(12):8587–8602.

[31] Jiang, Z.-M., Rihan, M., Zhang, P., Huang, L., Deng, Q., Zhang, J., and Mohamed, E. M. (2021). Intelligent reflecting surface aided dual-function radar and communication system. *IEEE Systems Journal*, 16(1):475–486.

[32] Kabir, H., Tham, M.-L., and Chang, Y. C. (2023). Internet of robotic things for mobile robots: concepts, technologies, challenges, applications, and future directions. *Digital Communications and Networks*.

[33] Khan, S., Ullah, S., Khan, H. U., and Rehman, I. U. (2023). Digital-twins-based internet of robotic things for remote health monitoring of covid-19 patients. *IEEE Internet of Things Journal*, 10(18):16087–16098.

[34] Li, N., Chen, B., and Tao, X. (2024a). Star-RIS assisted offloading based on hybrid noma: A time minimization perspective. *IEEE Transactions on Vehicular Technology*.

[35] Li, X., Gao, X., Yang, L., Liu, H., Wang, J., and Rabie, K. M. (2024b). Performance analysis of star-ris-cr-noma-based consumer iot networks for resilient industry 5.0. *IEEE Transactions on Consumer Electronics*, 70(1):1380–1391.

[36] Li, X., Wang, H., Chen, Y., and Sheng, S. (2024c). Joint resource allocation and reflecting precoding design for RIS-assisted isac systems. *IEEE Wireless Communications Letters*, 13(4):1193–1197.

[37] Li, X., Zhang, J., Han, C., Hao, W., Zeng, M., Zhu, Z., and Wang, H. (2023). Reliability and security of CR-STAR-RIS-NOMA assisted iot networks. *IEEE Internet of Things Journal*.

[38] Li, Y.-K. and Petropulu, A. (2023). Minorization-based low-complexity design for irs-aided isac systems. In *2023 IEEE Radar Conference (RadarConf23)*, pages 1–6. IEEE.

[39] Liu, F., Cui, Y., Masouros, C., Xu, J., Han, T. X., Eldar, Y. C., and Buzzi, S. (2022a). Integrated sensing and communications: Toward dual-functional wireless networks for 6g and beyond. *IEEE Journal on Selected Areas in Communications*, 40(6):1728–1767.

[40] Liu, X., Deng, Y., Han, C., and Di Renzo, M. (2021a). Learning-based prediction, rendering and transmission for interactive virtual reality in ris-assisted terahertz networks. *IEEE Journal on Selected Areas in Communications*.

[41] Liu, X., Deng, Y., Han, C., and Di Renzo, M. (2021b). Learning-based prediction, rendering and transmission for interactive virtual reality in ris-assisted terahertz networks. *IEEE Journal on Selected Areas in Communications*, 40(2):710–724.

[42] Liu, X., Liu, Y., Chen, Y., and Poor, H. V. (2020). RIS enhanced massive non-orthogonal multiple access networks: Deployment and passive beamforming design. *IEEE Journal on Selected Areas in Communications*, 39(4):1057–1071.

[43] Liu, Z., Song, J., Qiu, C., Wang, X., Chen, X., He, Q., and Sheng, H. (2022b). Hastening stream offloading of inference via multi-exit dnns in mobile edge computing. *IEEE Transactions on Mobile Computing*.

[44] Lyu, S., Peng, L., and Chang, S. Y. (2024). Investigating large-scale ris-assisted wireless communications using gnn. *IEEE Transactions on Consumer Electronics*, 70(1):811–818.

[45] Ma, T., Xiao, Y., Lei, X., and Xiao, M. (2023). Integrated sensing and communication for wireless extended reality (xr) with reconfigurable intelligent surface. *IEEE Journal of Selected Topics in Signal Processing*, pages 1–16.

[46] Ma, X., Fang, Y., Zhang, H., Guo, S., and Yuan, D. (2022a). Cooperative beamforming design for multiple RIS-assisted communication systems. *IEEE Transactions on Wireless Communications*, 21(12):10949–10963.

[47] Ma, Y., Ota, K., and Dong, M. (2022b). Multi-verse optimizer for multiple reconfigurable intelligent surfaces aided indoor wireless network. In *GLOBECOM 2022 - 2022 IEEE Global Communications Conference*, pages 6152–6157.

[48] Ma, Y., Ota, K., and Dong, M. (2024a). Multi-RIS deployment location optimization for coverage enhancement in outdoor wireless communication networks. *IEEE Transactions on Vehicular Technology*, pages 1–14.

[49] Ma, Y., Ota, K., and Dong, M. (2024b). Qoe optimization for virtual reality services in multi-RIS-assisted terahertz wireless networks. *IEEE Journal on Selected Areas in Communications*, 42(3):538–551.

[50] Ma, Y., Ota, K., and Dong, M. (2024c). Qoe optimization for virtual reality services in multi-ris-assisted terahertz wireless networks. *IEEE Journal on Selected Areas in Communications*.

[51] Mazaheri, M. H., Ameli, S., Abedi, A., and Abari, O. (2019). A millimeter wave network for billions of things. In *Proceedings of the ACM Special Interest Group on Data Communication*, pages 174–186.

[52] Mei, W. and Zhang, R. (2022). Intelligent reflecting surface for multi-path beam routing with active/passive beam splitting and combining. *IEEE Communications Letters*, 26(5):1165–1169.

[53] Nguyen, T. T. and Nguyen, K.-K. (2023). A deep learning framework for beam selection and power control in massive mimo - millimeter-wave communications. *IEEE Transactions on Mobile Computing*, 22(8):4374–4387.

[54] Pan, C., Ren, H., Wang, K., Kolb, J. F., Elkashlan, M., Chen, M., Di Renzo, M., Hao, Y., Wang, J., Swindlehurst, A. L., et al. (2021). Reconfigurable intelligent surfaces for 6g systems: Principles, applications, and research directions. *IEEE Communications Magazine*, 59(6):14–20.

[55] Pan, C., Zhou, G., Zhi, K., Hong, S., Wu, T., Pan, Y., Ren, H., Renzo, M. D., Lee Swindlehurst, A., Zhang, R., and Zhang, A. Y. (2022). An overview of signal processing techniques for RIS/IRS-aided wireless systems. *IEEE Journal of Selected Topics in Signal Processing*, 16(5):883–917.

[56] Perović, N. S., Tran, L.-N., Di Renzo, M., and Flanagan, M. F. (2021). Achievable rate optimization for MIMO systems with reconfigurable intelligent surfaces. *IEEE Transactions on Wireless Communications*, 20(6):3865–3882.

[57] Qi, Q., Chen, X., Khalili, A., Zhong, C., Zhang, Z., and Ng, D. W. K. (2022). Integrating sensing, computing, and communication in 6g wireless networks: Design and optimization. *IEEE Transactions on Communications*, 70(9):6212–6227.

[58] Qian, K., Yao, L., Zhang, X., and Ng, T. N. (2022a). Millimirror: 3d printed reflecting surface for millimeter-wave coverage expansion. In *Proceedings of the 28th Annual International Conference on Mobile Computing And Networking*, pages 15–28.

[59] Qian, K., Yao, L., Zhang, X., and Ng, T. N. (2022b). Millimirror: 3d printed reflecting surface for millimeter-wave coverage expansion. In *Proceedings of the 28th Annual International Conference on Mobile Computing And Networking*, MobiCom '22, page 15–28, New York, NY, USA. Association for Computing Machinery.

[60] Ray, P. P. (2016). Internet of robotic things: Concept, technologies, and challenges. *IEEE Access*, 4:9489–9500.

[61] Romeo, L., Petitti, A., Marani, R., and Milella, A. (2020). Internet of robotic things in smart domains: Applications and challenges. *Sensors*, 20(12):3355.

[62] Rossanese, M., Mursia, P., Garcia-Saavedra, A., Sciancalepore, V., Asadi, A., and Costa-Perez, X. (2022). Designing, building, and characterizing RF switch-based reconfigurable intelligent surfaces. In *Proceedings of the 16th ACM Workshop on Wireless Network Testbeds, Experimental Evaluation & CHaracterization*, page 69–76. Association for Computing Machinery.

[63] Saad, W., Bennis, M., and Chen, M. (2019). A vision of 6g wireless systems: Applications, trends, technologies, and open research problems. *IEEE Network*, 34(3):134–142.

[64] Saeed, T., Abadal, S., Liaskos, C., Pitsillides, A., Taghvaee, H., Cabellos-Aparicio, A., Soteriou, V., Alarcon, E., Akyildiz, I., and Lestas, M. (2021). Workload characterization and traffic analysis for reconfigurable intelligent surfaces within 6g wireless systems. *IEEE Transactions on Mobile Computing*.

[65] Sai, S., Prasad, M., Garg, A., and Chamola, V. (2024). Synergizing digital twins and metaverse for consumer health: A case study approach. *IEEE Transactions on Consumer Electronics*, 70(1):2137–2144.

[66] Shafi, M., Molisch, A. F., Smith, P. J., Haustein, T., Zhu, P., De Silva, P., Tufvesson, F., Benjebbour, A., and Wunder, G. (2017). 5g: A tutorial overview of standards, trials, challenges, deployment, and practice. *IEEE Journal on Selected Areas in Communications*, 35(6):1201–1221.

[67] Shen, K. and Yu, W. (2018). Fractional programming for communication systems—part i: Power control and beamforming. *IEEE Transactions on Signal Processing*, 66(10):2616–2630.

[68] Singh, K., Wang, P.-C., Biswas, S., Singh, S. K., Mumtaz, S., and Li, C.-P. (2023). Joint active and passive beamforming design for ris-aided ibfd iot communications: Qos and power efficiency considerations. *IEEE Transactions on Consumer Electronics*, 69(2):170–182.

[69] Strinati, E. C., Alexandropoulos, G. C., Wymeersch, H., Denis, B., Sciancalepore, V., D'Errico, R., Clemente, A., Phan-Huy, D.-T., De Carvalho, E., and Popovski, P. (2021). Reconfigurable, intelligent, and sustainable wireless environments for 6g smart connectivity. *IEEE Communications Magazine*, 59(10):99–105.

[70] Struye, J., Lemic, F., and Famaey, J. (2022). Covrage: Millimeter-wave beamforming for mobile interactive virtual reality. *IEEE Transactions on Wireless Communications*.

[71] Stutzman, W. L. and Thiele, G. A. (2012). *Antenna Theory and Design*. John Wiley & Sons, Hoboken, NJ, 3rd edition.

[72] Taneja, A. and Rani, S. (2024). Robust resource control mechanism for connected support to iot-based sustainable consumer electronics for industry 5.0. *IEEE Transactions on Consumer Electronics*, 70(1):1463–1470.

[73] Tang, W., Chen, M. Z., Chen, X., Dai, J. Y., Han, Y., Di Renzo, M., Zeng, Y., Jin, S., Cheng, Q., and Cui, T. J. (2020). Wireless communications with reconfigurable intelligent surface: Path loss modeling and experimental measurement. *IEEE Transactions on Wireless Communications*, 20(1):421–439.

[74] Wan, J., Ren, H., Pan, C., Yu, Z., Zhang, Z., and Zhang, Y. (2024). Reconfigurable intelligent surface assisted integrated sensing, communication and computation systems. *arXiv preprint arXiv:2402.13692*.

[75] Wang, J., Tang, W., Jin, S., Wen, C.-K., Li, X., and Hou, X. (2023a). Hierarchical codebook-based beam training for ris-assisted mmwave communication systems. *IEEE Transactions on Communications*.

[76] Wang, L., Abanto-Leon, L. F., and Asadi, A. (2022). Joint communication and sensing in ris-enabled mmwave networks. *arXiv preprint arXiv:2210.03685*.

[77] Wang, S., Song, X., Song, T., and Yang, Y. (2024). Fairness-aware computation offloading with trajectory optimization and phase-shift design in RIS-assisted multi-uav mec network. *IEEE Internet of Things Journal*, pages 1–1.

[78] Wang, X., Fei, Z., Huang, J., and Yu, H. (2021). Joint waveform and discrete phase shift design for ris-assisted integrated sensing and communication system under cramer-rao bound constraint. *IEEE Transactions on Vehicular Technology*, 71(1):1004–1009.

[79] Wang, Z., Mu, X., and Liu, Y. (2023b). Stars enabled integrated sensing and communications. *IEEE Transactions on Wireless Communications*.

[80] Wu, Q. and Zhang, R. (2019). Intelligent reflecting surface enhanced wireless network via joint active and passive beamforming. *IEEE Transactions on Wireless Communications*, 18(11):5394–5409.

[81] Wu, Z., Li, X., Cai, Y., and Yuan, W. (2024). Joint trajectory and resource allocation design for RIS-assisted uav-enabled isac systems. *IEEE Wireless Communications Letters*, pages 1–1.

[82] Wymeersch, H., Shrestha, D., De Lima, C. M., Yajnanarayana, V., Richerzhagen, B., Keskin, M. F., Schindhelm, K., Ramirez, A., Wolfgang, A., De Guzman, M. F., et al. (2021). Integration of communication and sensing in 6g: A joint industrial and academic perspective. In *2021 IEEE 32nd Annual International Symposium on Personal, Indoor and Mobile Radio Communications (PIMRC)*, pages 1–7. IEEE.

[83] Xia, L., Sun, Y., Liang, C., Feng, D., Cheng, R., Yang, Y., and Imran, M. A. (2023). Wiservr: Semantic communication enabled wireless virtual reality delivery. *IEEE Wireless Communications*, 30(2):32–39.

[84] Xie, R., Hu, D., Luo, K., and Jiang, T. (2021). Performance analysis of joint range-velocity estimator with 2d-music in ofdm radar. *IEEE Transactions on Signal Processing*, 69:4787–4800.

[85] Xu, S., Du, Y., Zhang, J., Liu, J., Wang, J., and Zhang, J. (2024). Intelligent reflecting surface enabled integrated sensing, communication and computation. *IEEE Transactions on Wireless Communications*, 23(3):2212–2225.

[86] Xu, W., An, J., Xu, Y., Huang, C., Gan, L., and Yuen, C. (2022). Time-varying channel prediction for ris-assisted mu-miso networks via deep learning. *IEEE Transactions on Cognitive Communications and Networking*.

[87] Yang, G., Xu, X., and Liang, Y.-C. (2020). Intelligent reflecting surface assisted non-orthogonal multiple access. *2020 IEEE Wireless Communications and Networking Conference (WCNC)*, pages 1–6.

[88] Yang, P., Quek, T. Q., Chen, J., You, C., and Cao, X. (2022). Feeling of presence maximization: mmwave-enabled virtual reality meets deep reinforcement learning. *IEEE Transactions on Wireless Communications*, 21(11):10005–10019.

[89] Yao, Y., Gu, B., Su, Z., and Guizani, M. (2021). Mvstgn: A multi-view spatial-temporal graph network for cellular traffic prediction. *IEEE Transactions on Mobile Computing*.

[90] Yildirim, I., Uyrus, A., and Basar, E. (2020). Modeling and analysis of reconfigurable intelligent surfaces for indoor and outdoor applications in future wireless networks. *IEEE Transactions on Communications*, 69(2):1290–1301.

[91] Yu, X., Wang, G., Huang, X., Wang, K., Xu, W., and Rui, Y. (2022). Energy efficient resource allocation for uplink ris-aided millimeter-wave networks with noma. *IEEE Transactions on Mobile Computing*.

[92] Yu, X., Xu, D., and Schober, R. (2019). Miso wireless communication systems via intelligent reflecting surfaces : (invited paper). *2019 IEEE/CIC International Conference on Communications in China (ICCC)*, pages 735–740.

[93] Yu, Z., Ren, H., Pan, C., Zhou, G., Wang, B., Dong, M., and Wang, J. (2023). Active ris aided isac systems: Beamforming design and performance analysis. *IEEE Transactions on Communications*.

[94] Yu, Z., Ren, H., Pan, C., Zhou, G., Wang, B., Dong, M., and Wang, J. (2024). Active ris-aided isac systems: Beamforming design and performance analysis. *IEEE Transactions on Communications*, 72(3):1578–1595.

[95] Yuan, Y., Xu, X., Han, S., Sun, M., Zhang, P., and Yuen, C. (2024). Energy-aware multiuser symbiotic communications enhanced by ris for passive iot. *IEEE Internet of Things Journal*, 11(1):1398–1412.

[96] Zeng, S., Zhang, H., Di, B., Han, Z., and Song, L. (2021). Reconfigurable intelligent surface (RIS) assisted wireless coverage extension: RIS orientation and location optimization. *IEEE Communications Letters*, 25(1):269–273.

[97] Zhang, J. and Blough, D. M. (2022). Optimizing coverage with intelligent surfaces for indoor mmwave networks. In *IEEE INFOCOM 2022-IEEE Conference on Computer Communications*, pages 830–839. IEEE.

[98] Zhao, J., Zhu, Y., Mu, X., Cai, K., Liu, Y., and Hanzo, L. (2022a). Simultaneously transmitting and reflecting reconfigurable intelligent surface (STAR-RIS) assisted UAV communications. *IEEE Journal on Selected Areas in Communications*, 40(10):3041–3056.

[99] Zhao, Y., Xu, W., You, X., Wang, N., and Sun, H. (2022b). Cooperative reflection and synchronization design for distributed multiple-RIS communications. *IEEE Journal of Selected Topics in Signal Processing*, 16(5):980–994.

[100] Zheng, B., You, C., and Zhang, R. (2021). Double-IRS assisted multi-user MIMO: Cooperative passive beamforming design. *IEEE Transactions on Wireless Communications*, 20(7):4513–4526.

[101] Zhu, Q., Li, M., Liu, R., and Liu, Q. (2023). Joint transceiver beamforming and reflecting design for active RIS-aided isac systems. *IEEE Transactions on Vehicular Technology*, 72(7):9636–9640.

Publications

Journals

1. Jiale Shu, Kaoru Ota, Mianxiong Dong, "RIS-enabled Integrated Sensing, Computing and Communication for Internet of Robotic Things," IEEE Internet of Things Journal, vol. 11, no. 20, pp. 32503-32513, 2024.

Proceeding of International Conference

1. Jiale Shu, Kaoru Ota, Mianxiong Dong, "Optimizing RIS Configurations for Diverse User Requirements via Network Traffic Prediction," The 8th IEEE International Conference on Smart Cloud, Tokyo, Japan, September 16-18, 2023

Under Review

1. Jiale Shu, Kaoru Ota, Mianxiong Dong, "Localization-based Beamforming for Mobile Virtual Reality in RIS-assisted mmWave Network," IEEE Transactions on Consumer Electronics, 2024.
2. Jiale Shu, Kaoru Ota, Mianxiong Dong, Ekram Hossain, "Large-Scale RIS-Assisted 6G Networks: Deployment and Cooperative Beamforming Design," IEEE Transactions on Wireless Communications (TWC), 2024.